LASER WAVELENGTH UPCONVERSION WITH OPTICAL PARAMETRIC OSCILLATORS USING SIMULTANEOUSLY PHASE-MATCHED CRYSTALS

A DISSERTATION
SUBMITTED TO THE DEPARTMENT OF ELECTRICAL AND ELECTRONICS ENGINEERING
AND THE INSTITUTE OF ENGINEERING AND SCIENCE
OF BILKENT UNIVERSITY
IN PARTIAL FULFILLMENT OF THE REQUIREMENTS
FOR THE DEGREE OF
DOCTOR OF PHILOSOPHY

By
Tolga Kartaloğlu
September 2002

LASER WAVELENGTH UPCONVERSION WITH OPTICAL PARAMETRIC OSCILLATORS USING SIMULTANEOUSLY PHASE-MATCHED CRYSTALS

A DISSERTATION

SUBMITTED TO THE DEPARTMENT OF ELECTRICAL AND ELECTRONICS ENGINEERING

AND THE INSTITUTE OF ENGINEERING AND SCIENCES

OF BILKENT UNIVERSITY

IN PARTIAL FULFILLMENT OF THE REQUIREMENTS

FOR THE DEGREE OF

DOCTOR OF PHILOSOPHY

By

Tolga Kartaloğlu

September 2002

I certify that I have read this thesis and that in my opinion it is fully adequate, in scope and in quality, as a thesis for the degree of Doctor of Philosophy.

Assoc. Prof. Dr. Orhan Aytür (Supervisor)

I certify that I have read this thesis and that in my opinion it is fully adequate, in scope and in quality, as a thesis for the degree of Doctor of Philosophy.

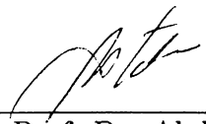

Prof. Dr. Abdullah Atalar

I certify that I have read this thesis and that in my opinion it is fully adequate, in scope and in quality, as a thesis for the degree of Doctor of Philosophy.

Prof. Dr. Hayrettin Köymen

I certify that I have read this thesis and that in my opinion it is fully adequate, in scope and in quality, as a thesis for the degree of Doctor of Philosophy.

Prof. Dr. Ekmel Özbay

I certify that I have read this thesis and that in my opinion it is fully adequate, in scope and in quality, as a thesis for the degree of Doctor of Philosophy.

Assoc. Prof. Dr. Feza Arıkan

Approved for the Institute of Engineering and Sciences:

Prof. Dr. Mehmet Baray
Director of Institute of Engineering and Sciences

ABSTRACT

LASER WAVELENGTH UPCONVERSION WITH OPTICAL PARAMETRIC OSCILLATORS USING SIMULTANEOUSLY PHASE-MATCHED CRYSTALS

Tolga Kartaloğlu
Ph.D. in Department of Electrical and Electronics Engineering
Supervisor: Assoc. Prof. Dr. Orhan Aytür
September 2002

In this thesis, we present our work on optical parametric oscillators that employ a single nonlinear crystal that is simultaneously-phase-matched for second-harmonic or sum-frequency generation in order to obtain frequency upconversion of laser radiation. We achieved simultaneous phase matching of optical parametric amplification together with second harmonic generation or sum frequency generation in bulk $KTiOPO_4$ and $KTiOAsO_4$ crystals, and in an aperiodically-poled $LiNbO_3$ crystal. We demonstrated very efficient frequency conversion of pulsed and continuous-wave lasers to higher frequencies with power conversion efficiencies reaching 40%. In addition, we present our work on an intracavity-doubled optical parametric oscillator that employs a periodically-poled $KTiOPO_4$ crystal for optical parametric amplification and an intracavity β–Ba_2BO_4 crystal for second harmonic generation. In this thesis, we also introduce a method for designing aperiodic grating structures for simultaneous phase matching in poled nonlinear crystals. In contrast to periodic grating structures, a grating structure designed using our method allows one to achieve simultaneous quasi-phase matching of two arbitrarily chosen nonlinear interactions with freely adjustable coupling coefficients.

Keywords: nonlinear frequency conversion, optical parametric oscillators, parametric devices, second harmonic generation, sum frequency generation, quasi-phase matching, aperiodically-poled.

ÖZET

AYNI ANDA FAZ UYUMU SAĞLANMIŞ KRİSTALLER KULLANARAK OPTİK PARAMETRİK OSİLATÖRLER İLE LAZER DALGABOYU YUKARI-ÇEVRİMİ

Tolga Kartaloğlu
Elektrik ve Elektronik Mühendisliği Doktora
Tez Yöneticisi: Doç. Dr. Orhan Aytür
Eylül 2002

Bu tezde, lazer ışımasının frekans yukarı çevrimi elde etmek amacı ile ikinci harmonik veya toplam frekans üretimi için aynı anda faz uyumu sağlanmış tek bir doğrusal olmayan kristal kullanan optik parametrik osilatörler üzerine çalışmalarımızı sunmaktayız. Kütle halinde $KTiOPO_4$ ve $KTiOAsO_4$ kristallerinde ve periyodik olmayacak şekilde kutuplanmış $LiNbO_3$ kristalinde, ikinci harmonik üretimi veya toplam frekans üretimi ile birlikte optik parametrik yükseltmenin aynı anda faz uyumunu sağlamayı başardık. Deneysel olarak %40'a varan güç dönüşüm verimi ile, yüksek frekanslara darbeli ve sürekli-dalga lazerlerin çok verimli frekans dönüşümünü gösterdik. Bunlara ek olarak, ikinci harmonik üretimi için kovuk içi β-Ba_2BO_4 kristali ve optik parametrik osilasyon için periyodik şekilde kutuplanmış $KTiOPO_4$ kristali kullanan kovuk-içi-katlanmış optik parametrik osilatörümüzü de sunmaktayız. Bu tezde, ayrıca, kutuplanmiş doğrusal olmayan kristalerde aynı anda faz uyumu sağlanmak için periyodik olmayan parmaklık yapısı tasarlamak için bir yöntemi tanıtmaktayız. Periyodik parmaklık yapıların aksine, bizim yöntemimiz ile tasarlanmış parmaklık yapıları serbestçe ayarlanabilen birleştirme katsayıları ile keyfi seçilmiş iki doğrusal olmayan etkileşimin aynı anda görünüşte faz uyumunu başarmaya izin vermektedir.

Anahtar Kelimeler: doğrusal olmayan frekans dönüştürme, optik parametrik osilatörler, parametrik cihazlar, ikinci harmonik üretimi, toplam frekans üretimi, görünüşte faz uyumu sağlama, periodik olmayan kutuplama.

ACKNOWLEDGMENTS

I would like to thank Assoc. Prof. Dr. Orhan Aytür for his supervision, special guidance, suggestions, and encouragement through the development of this thesis.

Special thanks to Prof. Dr. Abdullah Atalar, Prof. Dr. Hayrettin Köymen, Prof. Dr. Ekmel Özbay, and Assoc. Prof. Dr. Feza Arıkan for reading and commenting on the thesis.

During this long journey, Kahraman Güçlü Köprülü has been a close friend. We shared most problems since our undergraduate days. I am grateful to Hakkı Tunç Bostancı, Uğur Oğuz, Ayşegül Şahin, Murat Akgül, Lütfiye Durak, Ayhan Bozkurt, Ercan Solak ("tertip"), Ziya Gürkan Figen, and Vakur Ertürk for making my life at Bilkent University more pleasant with their friendship.

I would like to express my thanks to our department secretary Mürüvet Parlakay and laboratory technicians Ergün Hırlakoğlu and Ersin Başar for their help during my presence at the department of Electrical Engineering.

It is a pleasure to express my special thanks to my mother, father, and brother for their sincere love, support, and encouragement.

I would also like to express my thanks to the Turkish Scientific and Technical Research Council for their partial support of this work under Grand No. EEEAG-118 and Grand No. 197E050.

Contents

List of Figures

List of Abbreviations

APLN	aperiodically-poled lithium niobate ($LiNbO_3$)
BBO	beta-barium borate (β–Ba_2BO_4)
BPM	birefringent phase matching
cw	continuous-wave
DBS	dichroic beamsplitter
DFG	difference-frequency generation
GVD	group velocity dispersion
GVM	group velocity mismatch
HWP	half-wave plate
KTA	potassium titanyl arsenate ($KTiOAsO_4$)
KTP	potassium titanyl phosphate ($KTiOPO_4$)
OC	output-coupler
OPO	optical parametric oscillator
PP-KTP	periodically-poled potassium titanyl phosphate
QPM	quasi-phase matching
QWP	quarter-wave plate
SD-OPO	self-doubling optical parametric oscillator
SF-OPO	sum-frequency generating optical parametric oscillator
SFG	sum-frequency generation
SHG	second harmonic generation
THG	third harmonic generation
Ti:sapphire	titanium:sapphire

Chapter 1

Introduction

Ever since the invention of the laser by Maiman [1] in 1960, there has been a great deal of interest in the development of coherent light sources at new frequencies, since laser sources have broad applications in both research and industry. In addition, continuous frequency tunability is a benefit because there are various applications that need a range of frequencies to be spanned. Unfortunately, lasers cannot generate every desired frequency. Therefore, to obtain a new coherent source, frequency conversion of an available laser source to another frequency is important and if possible, tunability of this new source is an advantage.

In general, the response of optical materials to light is not linear. High intensity optical beams provided by lasers enable us to observe this nonlinearity. The field of nonlinear optics investigates this kind of interaction of light with materials. Optical materials that show high nonlinear response are called nonlinear materials.

By means of nonlinear optical processes, frequency conversion of lasers is possible. Second harmonic generation (SHG), sum frequency generation (SFG), optical parametric generation, and optical parametric amplification are widely used processes of nonlinear optics caused by second-order nonlinearity in a material. Using SHG or SFG, the frequency of laser light can be converted to a higher frequency (upconversion). On the contrary, an optical parametric oscillator (OPO) based on an optical parametric amplifier provides tunable conversion to lower frequencies (downconversion). Tunable

upconversion is possible by using two nonlinear processes one after another, i.e., upconversion followed by tunable downconversion or vice versa. We discovered that it is possible to achieve these two processes simultaneously within the same nonlinear material for efficient conversion [2]. As a result, we investigated simultaneous processes for upconversion and performed various experiments on OPOs employing these processes [3]–[10]. In this thesis, we present our work on these OPOs.

The field of nonlinear optics began in 1961 with the first example of frequency conversion. This was frequency doubling of a ruby laser using a quartz crystal by Franken [11]. Due to the nonlinear response of the crystal, a light beam at twice the frequency (second harmonic) of the laser beam was generated. The system was not tunable and the efficiency was less than one part per billion because a condition known as the phase matching condition was not satisfied in this experiment.

In addition to a nonlinear response, an efficient nonlinear interaction requires a means of achieving the phase matching condition. This condition states that phases of the interacting waves must be matched over an interaction distance of many optical wavelengths. Therefore, this condition is a requirement of momentum conservation. The early research on nonlinear optics led to an understanding of methods to achieve this condition. Two methods that are widely employed today are the use of birefringence to offset dispersion [12], [13] and the use of a periodic modulation of the sign of the nonlinear coefficient to periodically reset the optical phase [14]. The former method is referred to as birefringent phase matching (BPM) and the later method is now referred to as quasi-phase matching (QPM).

In 1962, Armstrong *et al.* [14], Kingston [15], and Kroll [16] proposed and analyzed the idea of tunable light generation by parametric amplification and parametric generation. Three years later in 1965, Wang and Rachetti [17] achieved the first experimental demonstration of parametric gain using a material that shows second-order nonlinearity. In the same year, Giordmaine and Miller [18] achieved the first parametric oscillation. They used a Q-switched Nd:$CaWO_4$ laser frequency-doubled to the green in $LiNbO_3$, to pump a monolithic $LiNbO_3$ tunable parametric oscillator.

When we consider the experiments by Franken, Wang, Rachetti, Giordmaine and

Miller, a material showing second-order nonlinearity was used to interact three optical waves whose frequencies are related by $\omega_3 = \omega_1 + \omega_2$ [14]–[16]. SFG, SHG, difference frequency generation (DFG), and optical parametric amplification and generation are different types of second-order nonlinear interactions of three optical waves, and are collectively referred to as three-wave mixing processes. They are also called three photon optical parametric processes. For example, in the SFG process, the nonlinearity in the material causes two photons at different frequencies to be combined to produce a single photon whose frequency is the sum of the frequencies of the initial two photons. As a result, three photons at different frequencies are involved in a SFG process. A SHG process is a special case of SFG in which the frequencies of the initial two photons are same.

Optical parametric amplification and DFG are the same processes. In the optical parametric amplification process, initially there are two photons. One of them is at a higher frequency than the other and is called a pump photon. The other one is at a lower frequency and is called a signal photon. In the process, the pump photon splits into two photons at lower frequencies with the influence of the signal photon. As a result, a new photon whose frequency is the difference of the frequencies of the pump and the signal photons, called an idler photon, and a photon identical to the signal photon are created. As a result, in addition to the generation of an idler photon at the difference frequency, the number of signal photons is increased.

Generation of new photons with optical parametric amplification does not necessarily require an initial signal photon. Spontaneous parametric generation of two photons from a pump photon is also possible. In the spontaneous parametric generation process, the pump photon at frequency ω_p breaks down into a signal and an idler photon at lower frequencies ω_s and ω_i, respectively. Energy and momentum are conserved in the process. These correspond to the relation of the frequencies, $\omega_p = \omega_s + \omega_i$, and the matching of the wavevectors, $\mathbf{k}_p = \mathbf{k}_s + \mathbf{k}_i$, of the waves corresponding to the pump, the signal and the idler photons. The wavevector matching, i.e. conservation of momentum, formulates the phase matching condition.

SHG, SFG and DFG processes can convert a particular frequency to another fixed

frequency. On the other hand, optical parametric generation can achieve tunable conversion to a band of frequencies. For this purpose, an OPO can be constructed by simply adding optical feedback around a parametric generator-amplifier, just like in a laser. However, in contrast to most lasers, OPOs are truly tunable sources of coherent radiation because they employ optical parametric generation where tunable virtual energy levels are involved in the process.

An OPO is analogous to an optically pumped three-level laser. The frequency of the pump beam determines the top energy level. The mid-energy level is determined by the frequency of the signal and the idler beams that satisfy the phase matching condition. These energy levels are virtual and non-resonant in contrast to lasers. Continuous tuning of the OPO is achieved by externally changing the phase matching condition. Since the phase matching condition depends on the refractive indices and the frequencies of the light beams, the frequencies can be changed by adjusting the refractive indices. To do this, one can change the temperature of the material (temperature tuning) or change the propagation direction of the light beams (angle tuning).

Most of the characteristics of OPOs are determined by their pump sources. An OPO pumped by a continuous-wave (cw) laser generates a continuous-wave output. Its resonator size can be as small as the length of the nonlinear gain medium. However, Q-switched lasers provide pulsed outputs. Pulse widths are on the order of 10 ns with low repetition rates. Although the duration of the pulses are short, their peak powers are so high that there are many efficient OPOs designed to operate with Q-switched lasers [19]. In these OPOs, each laser pulse starts a new oscillation, generating a new output pulse because the OPO cavity length is much smaller than the pump pulse length, and a signal pulse resonating inside the cavity can build up by multiple passes within a single pump pulse.

Mode-locked lasers also provide pulsed outputs. These sources produce short pulses with high repetition rates. Pulse widths are on the order of 100 fs–100 ps. Although they have high peak powers like Q-switched lasers, a single pulse from a mode-locked laser is not enough to produce an oscillation in an OPO, because the duration of these pulses are not long enough for oscillations to build up. Therefore, a method called "synchronous

pumping" is employed in OPOs pumped by mode-locked lasers. In this method, the cavity length of the OPO is adjusted for a synchronous operation with a mode-locked pump laser, pump pulses always meet and propagate with the intracavity signal pulse in the nonlinear material, while the intracavity signal pulse travels back and forth in the OPO cavity. As a result, each pump pulse gives some energy to the signal pulse. As the signal pulse grows, it saturates the gain of the parametric amplifier and reaches a steady level where energy taken from the pump pulse just compensates for the losses of the signal pulse in the cavity. From this point of view, its operation characteristic is similar to a cw OPO operating in a steady-state condition.

Since 1965, there have been many demonstrations of OPOs with different kinds of lasers as pump sources. A special issue of the *Journal of the Optical Society of America Part B* in published 1993 [19] covered the achievements made in the field of parametric devices during the previous two decades. Articles on cw parametric devices, pulsed high peak power infrared tunable sources, visible parametric sources, synchronously-pumped picosecond and femtosecond parametric devices, and spectroscopic applications can be found in this issue. A second special issue on parametric devices was also published in 1995 [20]. In this issue, highly efficient devices, frequency control and spectroscopic applications, picosecond and femtosecond synchronously-pumped parametric devices, and parametric amplifiers were covered. An important article in this issue was about the first demonstrations of the quasi-phase-matched OPOs in bulk periodically-poled $LiNbO_3$ by Myers *et al.* [21].

Although QPM was proposed in 1962 together with the idea of BPM, and the first OPO using BPM was demonstrated in 1965, the demonstration of an OPO using QPM has taken much longer. This is due to the fact that until 1994 crystal quality and technology did not allow the control of ferroelectric domains with the required precision in bulk crystals [22]–[24]. The electric field induced domain inversion process, discovered by Yamada *et al.* [25], results in a crystal structure in which the sign of the nonlinear coefficient is modulated. This process led to a success for bulk crystals in 1994 and quasi-phase-matched second harmonic generation was demonstrated by Burns *et al.* [26] and Webjorn *et al.* [27] in the same year.

The field of nonlinear optics also depends on the progress in the laser sources, as well as the improvement of nonlinear optical materials. For example, Rhodamine 6G dye laser is the first laser that pumped a femtosecond OPO [28]. After this, there have been many demonstrations of femtosecond OPOs [29]–[33], especially using titanium:sapphire (Ti:sapphire) lasers.

Until we have demonstrated efficient frequency upconversion using an optical parametric oscillator pumped by a femtosecond Ti:sapphire laser that employ a single nonlinear crystal which is also phase-matched for second-harmonic generation (SHG) in 1997 [4], tunable frequency conversion of a mode-locked laser to higher frequencies was achieved using two nonlinear crystals; one for parametric oscillation with tunable conversion and one for SHG or SFG for upconversion. In one approach, the OPO is pumped by the frequency-doubled pump laser output [34]. A more widely used approach is to frequency-double the signal (or the idler) beam outside [35] or inside [36], [37] the OPO cavity. For this approach, intracavity operation is usually preferred in order to take advantage of the high intensity of the resonant field. Another approach is SFG with the residual (unconverted in the OPO) pump and the signal or idler. This can also be implemented extracavity or intracavity [38], [39]. These upconversion OPOs have successfully generated tunable ultrafast pulses at visible wavelengths, however mostly with limited conversion efficiencies ($\sim$ 10%), with the exception of [38] (25% with SFG, 31% with SHG).

The simultaneous phase matching of two different second-order nonlinear processes within the same crystal opens up many frequency conversion possibilities [40]. Since 1997, we have employed simultaneous phase matching in our OPOs to obtain upconversion [5]–[10]. In addition, there has been a growing interest in the simultaneous phase matching of two different nonlinear interactions within the same second-order nonlinear crystal in recent years [3]–[10], [41]–[68], because simultaneous phase matching allows efficient frequency conversion of two-step interactions. For example, the combination of optical parametric oscillation with SHG in the same second-order nonlinear crystal in one of our experiments results in very efficient frequency conversion reaching 34% [4].

There have been various experimental demonstrations of simultaneously-phase-matched interactions using either BPM [3]–[10], [40], [41] or periodic QPM [44], [46]–[51]. However, simultaneous phase matching occurs by chance for both BPM and periodic QPM i.e., given a pair of source and target frequencies, there is no guarantee that either method will come up with a suitable crystal design.

In simultaneous phase matching, the relative strength of the two processes is also important because this affect the over all conversion efficiency [42], [43]. Unfortunately, neither BPM nor periodic QPM methods allow any room for adjusting this important parameter.

In order to overcome the restrictions of BPM and periodic QPM, a number of groups have recently proposed the use of quasi-periodic or aperiodic poling schemes to achieve simultaneous phase matching with QPM [8], [9], [52]–[68]. In one of these schemes, quasi-periodic grating structure based on Fibonacci sequences is used [52]–[61]. Third harmonic generation (THG) [53], [56], [58], [61] and multiple-peak frequency doubling [54], [55] (phase-matched SHG for a number of distinct discrete frequencies) were experimentally demonstrated using such schemes. However, Fibonacci-based schemes also suffer from the limitation of BPM and QPM and cannot be used to achieve simultaneous phase matching. This limitation was alleviated by an extension of Fibonacci-based schemes that allow independent phase matching of the two interactions [62]–[64]. Two-peak frequency doubling [63] and THG [63], [64] were experimentally demonstrated using these structures. However, neither approach of Fibonacci sequences provides a general mechanism to adjust the relative strength of the two simultaneously phase-matched processes. Aperiodic schemes are solutions to both limitations of BPM and periodic QPM. In one method, aperiodic schemes that are optimized using simulated annealing for maximizing the conversion efficiency were proposed for multiple-peak frequency doubling, tripling, and parametric amplification [65]–[67]. However, this approach does not take pump depletion into account, and cannot be expected to yield accurate results. Another scheme for designing aperiodic grating structures which enables free adjustment of the relative strength of the two processes was proposed [68], but awaits experimental verification. Recently, we have also proposed a method employing aperiodic schemes for QPM and demonstrated the idea with experiments [8], [9].

In this thesis, we present our work on OPOs that employ a single simultaneously phase-matched nonlinear crystal for tunable frequency upconversion of laser radiation. We achieved simultaneous phase matching of optical parametric oscillation together with SHG or SFG in bulk $KTiOPO_4$ (KTP) and $KTiOAsO_4$ (KTA) crystals and an aperiodically-poled $LiNbO_3$ crystal (APLN). We demonstrated efficient frequency conversion of pulsed and cw lasers to higher frequencies. In addition, we present our work on an intracavity-doubled OPO that employs a periodically-poled KTP (PP-KTP) crystal for optical parametric amplification and an intracavity β–Ba_2BO_4 (BBO) crystal for SHG. In this thesis, we also introduce a method for designing an aperiodic grating structure for poling of nonlinear crystals.

We designed and implemented two phase-matched self-doubling optical parametric oscillators (SD-OPOs) where a single nonlinear crystal is employed for both parametric generation and frequency doubling using BPM. One of our SD-OPO is based on a KTP crystal that is synchronously-pumped by a femtosecond Ti:sapphire laser operating at a wavelength of 745 nm [3],[4]. When pumped at this wavelength, the KTP crystal is phase-matched for parametric generation at a signal wavelength of 1080 nm, corresponding to an idler wavelength of 2400 nm. The singly-resonant OPO cavity consists of highly reflecting mirrors at the signal wavelength. The signal beam is also phase-matched for SHG at the same crystal orientation. With proper intracavity polarization rotation, a frequency-doubled output beam at a wavelength of 540 nm is generated. A power conversion efficiency of 34% is achieved in the KTP crystal. To our knowledge, this is the first demonstration of phase-matched optical parametric oscillation and frequency doubling within a single crystal.

Other SD-OPO is based on KTA crystal [10]. The SD-OPO is also synchronously-pumped by the Ti:sapphire laser operating at a wavelength of 796 nm. BPM in the KTA crystal leads to a signal beam at 1150 nm. Simultaneously phase-matched frequency doubling of the intracavity signal beam within the same KTA crystal is also facilitated by intracavity rotation of the signal polarization. The resulting yellow beam at 575 nm exits the cavity via a dichroic beam-splitter. A fixed time delay introduced between the two orthogonally polarized intracavity signal pulses is shown to alleviate temporal pulse overlap problems associated with group velocity mismatch (GVM). The overall

(796 nm to 575 nm) power conversion efficiency of the two step process is 39.4% in KTA crystal. To our knowledge, this is the highest value reported to date for an intracavity frequency-doubled OPO.

We also designed and implemented a synchronously-pumped single-crystal sum-frequency generating OPO (SF-OPO) where the SFG process takes place within the OPO crystal itself [5]–[7]. Our SF-OPO is based on a KTP crystal where BPM is used for both processes. The polarization geometry of the two phase matching conditions necessitates a pump polarization that is at an angle to the fast and slow axes of the birefringent KTP crystal. Adjusting the group delay between the fast and slow components of the pump to compensate for the GVM in the KTP crystal increases the photon conversion efficiency by more than three fold. We have demonstrated 43% power conversion efficiency from the pump to the sum-frequency beam.

In addition to these simultaneously-phase-matched OPOs, we implemented an intracavity-doubled OPO that employs a periodically-poled KTP (PP-KTP) crystal for optical parametric amplification and a BBO crystal for SHG. Our OPO is synchronously-pumped by a Ti:sapphire laser operating at a wavelength of 760 nm. Quasi-phase matching is achieved with a 24 μm poling period in the PP-KTP crystal, resulting in a signal wavelength of 1260 nm and an idler wavelength of 1915 nm. Type-I SHG of the signal beam is achieved in the BBO crystal. The SHG output is tunable over a 90 nm range around 630 nm by changing the cavity length [69]. We achieved maximum conversion efficiency of 15.9%.

In this thesis, we describe a method for designing an aperiodic grating structure to simultaneously phase match two arbitrary second-order nonlinear processes within the same crystal. This method also allows the relative strength of the two processes to be adjusted freely. We performed an experiment based on an aperiodically-poled $LiNbO_3$ (APLN) crystal designed using our method [8], [9]. In this crystal, parametric oscillation and SHG are simultaneously phase-matched for upconversion of a femtosecond Ti:sapphire laser to 570 nm. This self-doubling OPO (SD-OPO) provides an experimental verification of our design method.

We implement two cw SD-OPOs. They are based on the KTA and APLN crystals

used in the femtosecond experiments. In these OPOs, we achieve necessary high intensity by designing a pump laser and an intracavity OPO because this design technique is used for various singly-resonant cw OPOs with success [70]–[73]. For this purpose, we implemented a cw Ti:sapphire laser and demonstrated two intracavity singly-resonant cw SD-OPOs.

In Chapter 2, a theoretical background for the interaction of optical waves in a nonlinear material is presented. We also introduce simultaneously-phase-matched interactions in this chapter. In Chapter 3, BPM and QPM methods are described and the calculation of phase matching curves is presented. In addition, we present our aperiodic-grating-structure design method for simultaneous phase matching. Chapter 4 covers information on some common experimental devices, operational principles, and measurement methods. Nonlinear crystals that are used in our experiments are also provided with simultaneous phase matching examples in this chapter. We describe our femtosecond experiments and their results in Chapter 5 and cw experiments and their results in Chapter 6. Finally, remarks and conclusions are provided in Chapter 7.

Chapter 2

Optical Parametric Interactions

In this chapter, we briefly present the theory of optical parametric interactions as background information. First, we go over the interaction of optical waves with a material that shows a nonlinear response, and then present the derivation of differential equations (coupled-mode equations) that describe the interaction of three light waves through a second-order nonlinearity. We discuss two important parameters of the coupled-mode equations, the "phase mismatch term" and the "effective nonlinear coefficient." These parameters are related to the physical properties of a nonlinear material, and play an important role in the design of experiments. Finally, we present the coupled-mode equations of the simultaneously phase-matched interactions that take place in our experiments.

2.1 Nonlinear Materials

Nonlinear behavior of optical materials was observed shortly after the invention of the laser. High intensity optical fields from lasers are necessary to observe such nonlinear behavior in optical materials. The three-wave mixing process is an interaction of three light waves at different frequencies in a material showing second-order nonlinearity. SHG, SFG, and DFG are examples of the three-wave mixing process.

In optical materials, the general relation between the polarization field $\mathbf{P}(\mathbf{r}, t)$ and

the electric field $\mathbf{E}(\mathbf{r},t)$ is nonlinear and dispersive [74]. This relation can be expressed as a power series of the electric field. The dispersion, being a property that states frequency dependence, has a simple expression as a multiplicative function in frequency domain. When we write the polarization field in time domain, this multiplicative function becomes a convolution. Also, all of the coefficients of the power series are expressed in terms of tensor multiplications, because the materials involved are generally anisotropic. As a result, the general relation between $\mathbf{P}(\mathbf{r},t)$ and $\mathbf{E}(\mathbf{r},t)$ can be written as

$$\begin{aligned}\mathbf{P}(\mathbf{r},t) &= \epsilon_0 \int_{-\infty}^{t} \overline{\overline{\chi}}^{(1)}(t-t')\cdot\mathbf{E}(\mathbf{r},t')dt' \\ &+\epsilon_0 \int_{-\infty}^{t}\int_{-\infty}^{t} \overline{\overline{\overline{\chi}}}^{(2)}(t-t',t-t'') : \mathbf{E}(\mathbf{r},t')\mathbf{E}(\mathbf{r},t'')dt'dt'' + \text{h.o.t.},\end{aligned} \tag{2.1}$$

where ϵ_0 is the permittivity of free space, $\overline{\overline{\chi}}^{(1)}$ is the linear susceptibility tensor of second rank, $\overline{\overline{\overline{\chi}}}^{(2)}$ is the second-order nonlinear susceptibility tensor of third rank and ":" is the double product defined as

$$\overline{\overline{\overline{\chi}}}^{(2)}(t-t',t-t'') : \mathbf{E}(\mathbf{r},t')\mathbf{E}(\mathbf{r},t'') = \mathbf{E}(\mathbf{r},t'')\cdot\overline{\overline{\overline{\chi}}}^{(2)}(t-t',t-t'')\cdot\mathbf{E}(\mathbf{r},t'). \tag{2.2}$$

In this representation, the first term

$$\mathbf{P}^{(1)}(\mathbf{r},t) = \epsilon_0 \int_{-\infty}^{t} \overline{\overline{\chi}}^{(1)}(t-t')\cdot\mathbf{E}(\mathbf{r},t')dt' \tag{2.3}$$

is the linear polarization that is responsible for the refractive index and its dispersion. The next term,

$$\mathbf{P}^{(2)}(\mathbf{r},t) = \epsilon_0 \int_{-\infty}^{t}\int_{-\infty}^{t} \overline{\overline{\overline{\chi}}}^{(2)}(t-t',t-t'') : \mathbf{E}(\mathbf{r},t')\mathbf{E}(\mathbf{r},t'')dt'dt'' \tag{2.4}$$

is the second-order nonlinear polarization term. In this term, the second-order susceptibility tensor relates the electric field to the polarization field in a manner that the square of or product of the components of the electric field vector is involved.

There are also higher order terms (h.o.t.) in the relation between $\mathbf{P}(\mathbf{r},t)$ and $\mathbf{E}(\mathbf{r},t)$. Values of elements of their nonlinear susceptibility tensors are much smaller compared to values of the elements of the second-order nonlinear susceptibility tensor. However, the higher order terms may be comparable to the second-order term as well as the linear

term if intensity of the electric field is very high. For example, third order nonlinearity in an optical material causes the "optical Kerr effect" and makes the "four wave mixing process" possible. There are also materials in which the second-order nonlinear susceptibility tensor totally vanishes due to a center of inversion symmetry. These are called centrosymmetric materials and their nonlinear response is due to higher order terms. In our case, we are interested in three-wave mixing processes in an optical material showing second-order nonlinearity, and briefly present the theory of these parametric interactions.

2.2 Second-order Nonlinear Polarization

In this section, we investigate how the second-order susceptibility tensor relates three waves of different frequencies. We represent these waves as monochromatic waves, because a simple representation of laser radiation can be made by monochromatic waves. The total electric field $\mathbf{E}(\mathbf{r},t)$ of these waves is

$$\mathbf{E}(\mathbf{r},t) = \sum_i \mathrm{Re}\left[\mathbf{E}_i(\mathbf{r})e^{j\omega_i t}\right] = \frac{1}{2}\sum_i \left[\mathbf{E}_i(\mathbf{r})e^{j\omega_i t} + \mathbf{E}_i^*(\mathbf{r})e^{-j\omega_i t}\right], \tag{2.5}$$

where $\mathbf{E}_i(\mathbf{r})$ is the slowly varying electric field phasor at an angular frequency ω_i and $i = 1, 2, 3$.

When we consider two electric field phasors at frequencies ω_1 and ω_2, as a result of second-order nonlinearity, they give rise to a nonlinear polarization phasor

$$\mathbf{P}^{(2)}(\mathbf{r}) = \frac{1}{2}\epsilon_0 \overleftrightarrow{\chi}^{(2)}(\omega_1,\omega_2) : \mathbf{E}_1(\mathbf{r})\mathbf{E}_2(\mathbf{r}) + \frac{1}{2}\epsilon_0 \overleftrightarrow{\chi}^{(2)}(\omega_2,\omega_1) : \mathbf{E}_2(\mathbf{r})\mathbf{E}_1(\mathbf{r}). \tag{2.6}$$

Since, $\mathbf{E}_1(\mathbf{r})$ and $\mathbf{E}_2(\mathbf{r})$ are associated with time dependences $e^{j\omega_1 t}$ and $e^{j\omega_2 t}$, respectively, the second-order nonlinear polarization phasor resulting from their product is associated with a time dependence $e^{j(\omega_1+\omega_2)t}$ at the sum frequency $\omega_1+\omega_2$. There are other nonlinear polarization phasors caused by these two electric field phasors but those are at frequencies $2\omega_1$, $2\omega_2$, $\omega_1-\omega_2$, $\omega_2-\omega_1$ and 0. Therefore, $\overleftrightarrow{\chi}^{(2)}$ can be expressed as a function of three frequencies for which one of them is always related to the other two by a sum or a difference.

Full permutation symmetry property and Kleinman's symmetry condition [74] state that we can write

$$\overleftrightarrow{\chi}^{(2)}(\omega_1+\omega_2,\omega_1,\omega_2) = \overleftrightarrow{\chi}^{(2)}(\omega_1+\omega_2,\omega_2,\omega_1). \tag{2.7}$$

Hence, the second-order nonlinear polarization phasor takes the form of

$$\mathbf{P}^{(2)}(\mathbf{r}) = \epsilon_0\overleftrightarrow{\chi}^{(2)}(\omega_1+\omega_2,\omega_1,\omega_2):\mathbf{E}_1(\mathbf{r})\mathbf{E}_2(\mathbf{r}). \tag{2.8}$$

An important fact is that although there is no initial electric field at the sum frequency $\omega_1+\omega_2$, there is a polarization field at this frequency and this induced time varying polarization acts as a source of electromagnetic radiation.

Similarly, when we consider the third electric field phasor with the other two electric field phasors, nonlinear polarizations

$$\epsilon_0\overleftrightarrow{\chi}^{(2)}(\omega_3-\omega_1,\omega_3,\omega_1):\mathbf{E}_3(\mathbf{r})\mathbf{E}_1^*(\mathbf{r}) \tag{2.9}$$

and

$$\epsilon_0\overleftrightarrow{\chi}^{(2)}(\omega_3-\omega_2,\omega_3,\omega_2):\mathbf{E}_3(\mathbf{r})\mathbf{E}_2^*(\mathbf{r}) \tag{2.10}$$

are also generated. When the frequencies of these three fields are related by

$$\omega_3=\omega_1+\omega_2, \tag{2.11}$$

the nonlinear polarization phasors in Equations (2.8), (2.9), and (2.10) show that there is a coupling between the three fields through the second-order nonlinearity.

2.3 Coupled-Mode Equations

With the addition of the nonlinear polarization terms, one can derive a set of equations (the coupled-mode equations) from Maxwell's equations to describe second-order nonlinear interactions. Maxwell's equations for a source free and lossless medium are given by

$$\nabla\times\mathbf{E} = -\frac{\partial\mathbf{B}}{\partial t}, \tag{2.12}$$

$$\nabla \times \mathbf{H} = \frac{\partial \mathbf{D}}{\partial t}, \tag{2.13}$$

$$\nabla \cdot \mathbf{D} = 0, \tag{2.14}$$

$$\nabla \cdot \mathbf{B} = 0, \tag{2.15}$$

and the constitutive relations for a nonmagnetic medium are

$$\mathbf{D} = \epsilon_0 \mathbf{E} + \mathbf{P}, \tag{2.16}$$

$$\mathbf{B} = \mu_0 \mathbf{H}, \tag{2.17}$$

where μ_0 is the permeability of free space, $\mathbf{H}$ is the magnetic field, $\mathbf{D}$ and $\mathbf{B}$ are the electric and the magnetic flux densities, respectively. When the linear and the nonlinear parts of the polarization field are separated, the constitutive relation between the electric field and the electric flux density takes the form of

$$\mathbf{D} = \mathbf{D}_L + \mathbf{P}^{(2)}, \tag{2.18}$$

where

$$\mathbf{D}_L = \epsilon_0 \mathbf{E} + \mathbf{P}^{(1)} = \epsilon_0 \overline{\overline{\epsilon}}_r \cdot \mathbf{E}, \tag{2.19}$$

denotes the linear part of electric flux density and $\overline{\overline{\epsilon}}_r$ is the relative permeability tensor defined as

$$\overline{\overline{\epsilon}}_r = \overline{\overline{\mathbf{I}}} + \overline{\overline{\chi}}^{(1)}. \tag{2.20}$$

where $\overline{\overline{\mathbf{I}}}$ is a three by three identity tensor.

Similar to the derivation of the homogeneous wave equation [75], a nonlinear driven wave equation

$$\nabla \times [\nabla \times \mathbf{E}(\mathbf{r}, t)] + \mu_0 \frac{\partial^2}{\partial t^2} \mathbf{D}_L(\mathbf{r}, t) = -\mu_0 \frac{\partial^2}{\partial t^2} \mathbf{P}^{(2)}(\mathbf{r}, t) \tag{2.21}$$

is derived by taking the curl of Equation (2.12) and using Equation (2.13). Equation (2.21) differs from the homogeneous wave equation by the right hand side term.

In nonlinear interactions, intensity variation of three waves occur over distances and times that are much larger than the sinusoidal oscillations of their fields. Therefore, a plane wave representation with a slowly varying envelope function can be used for each

of the waves propagating nearly in the same direction. For these waves at frequencies ω_1, ω_2, and $\omega_3 = \omega_2 + \omega_1$, the electric and the polarization phasors are written as

$$\mathbf{E}_i(\mathbf{r}) = \hat{\mathbf{a}}_i A_i(\mathbf{r}) e^{-j\mathbf{k}_i \cdot \mathbf{r}}, \tag{2.22}$$

$$\mathbf{P}_i^{(2)}(\mathbf{r}) = \hat{\mathbf{a}}_i' B_i(\mathbf{r}) e^{-j\mathbf{k}_i' \cdot \mathbf{r}}, \tag{2.23}$$

where $i = 1, 2, 3$. The unit vectors $\hat{\mathbf{a}}_i$ and $\hat{\mathbf{a}}_i'$ represent the direction of polarization, $A_i(\mathbf{r})$ and $B_i(\mathbf{r})$ represent the slowly varying envelope functions of the electric field and the second-order nonlinear polarization field, and $\mathbf{k}_i$ and $\mathbf{k}_i'$ are the wavevectors of the electric field and the nonlinear polarization field.

Relations between the slowly varying envelope functions $A_i(\mathbf{r})$ and $B_i(\mathbf{r})$ and between the propagation constants $\mathbf{k}_i$ and $\mathbf{k}_i'$ are found using Equations (2.8), (2.9), and (2.10) as

$$\hat{\mathbf{a}}_1' B_1(\mathbf{r}) = \epsilon_0 \overline{\overline{\overline{\chi}}}^{(2)}(\omega_1 = \omega_3 - \omega_2, \omega_3, \omega_2) : \hat{\mathbf{a}}_3 \hat{\mathbf{a}}_2 A_3(\mathbf{r}) A_2^*(\mathbf{r}), \tag{2.24}$$

$$\hat{\mathbf{a}}_2' B_2(\mathbf{r}) = \epsilon_0 \overline{\overline{\overline{\chi}}}^{(2)}(\omega_2 = \omega_3 - \omega_1, \omega_3, \omega_1) : \hat{\mathbf{a}}_3 \hat{\mathbf{a}}_1 A_3(\mathbf{r}) A_1^*(\mathbf{r}), \tag{2.25}$$

$$\hat{\mathbf{a}}_3' B_3(\mathbf{r}) = \epsilon_0 \overline{\overline{\overline{\chi}}}^{(2)}(\omega_3 = \omega_1 + \omega_2, \omega_1, \omega_2) : \hat{\mathbf{a}}_1 \hat{\mathbf{a}}_2 A_1(\mathbf{r}) A_2(\mathbf{r}), \tag{2.26}$$

and

$$\mathbf{k}_1' = \mathbf{k}_3 - \mathbf{k}_2, \tag{2.27}$$

$$\mathbf{k}_2' = \mathbf{k}_3 - \mathbf{k}_1, \tag{2.28}$$

$$\mathbf{k}_3' = \mathbf{k}_1 + \mathbf{k}_2, \tag{2.29}$$

with the frequency condition given in Equation (2.11). Using the definitions in Equations (2.22) and (2.23), the nonlinear driven wave equation can be expressed in frequency domain as

$$\nabla \times \left\{ \nabla \times \left[A_i(\mathbf{r}) e^{-j\mathbf{k}_i \cdot \mathbf{r}} \hat{\mathbf{a}}_i \right] \right\} - \mu_0 \epsilon_0 \omega_i^2 \overline{\overline{\epsilon}}_r \cdot \hat{\mathbf{a}}_i A_i(\mathbf{r}) e^{-j\mathbf{k}_i \cdot \mathbf{r}} = \mu_0 \omega_i^2 \hat{\mathbf{a}}_i' B_i(\mathbf{r}) e^{-j\mathbf{k}_i' \cdot \mathbf{r}}. \tag{2.30}$$

By dot multiplying Equation (2.30) with $\hat{\mathbf{a}}_i$ and neglecting the second-order derivatives under the slowly varying envelope approximation,

$$\left| \nabla^2 A_i(\mathbf{r}) \right| \ll \left| \mathbf{k}_i \cdot \nabla A_i(\mathbf{r}) \right|, \tag{2.31}$$

the wave equations can be approximated by

$$\widehat{\mathbf{k}}_1 \cdot \nabla A_1(\mathbf{r}) = -j\frac{\omega_1 d_1}{cn_1} A_3(\mathbf{r}) A_2^*(\mathbf{r}) e^{-j\Delta\mathbf{k}\cdot\mathbf{r}}, \tag{2.32}$$

$$\widehat{\mathbf{k}}_2 \cdot \nabla A_2(\mathbf{r}) = -j\frac{\omega_2 d_2}{cn_2} A_3(\mathbf{r}) A_1^*(\mathbf{r}) e^{-j\Delta\mathbf{k}\cdot\mathbf{r}}, \tag{2.33}$$

$$\widehat{\mathbf{k}}_3 \cdot \nabla A_3(\mathbf{r}) = -j\frac{\omega_3 d_3}{cn_3} A_1(\mathbf{r}) A_2(\mathbf{r}) e^{j\Delta\mathbf{k}\cdot\mathbf{r}}, \tag{2.34}$$

where

$$\Delta\mathbf{k} = \mathbf{k}_3 - \mathbf{k}_2 - \mathbf{k}_1 \tag{2.35}$$

is the phase mismatch term and $\widehat{\mathbf{k}}_i$ are the unit vectors in the direction of the wavevectors $\mathbf{k}_i$. The constant $c = 1/\sqrt{\epsilon_0\mu_0}$ is the speed of light in free space and n_i represent refractive indices for $i = 1, 2, 3$. The constants d_i given by

$$d_1 = \frac{1}{2}\hat{\mathbf{a}}_1 \cdot \overline{\overline{\overline{\chi}}}^{(2)}(\omega_1 = \omega_3 - \omega_2) : \hat{\mathbf{a}}_3\hat{\mathbf{a}}_2, \tag{2.36}$$

$$d_2 = \frac{1}{2}\hat{\mathbf{a}}_2 \cdot \overline{\overline{\overline{\chi}}}^{(2)}(\omega_2 = \omega_3 - \omega_1) : \hat{\mathbf{a}}_3\hat{\mathbf{a}}_1, \tag{2.37}$$

$$d_3 = \frac{1}{2}\hat{\mathbf{a}}_3 \cdot \overline{\overline{\overline{\chi}}}^{(2)}(\omega_3 = \omega_1 + \omega_2) : \hat{\mathbf{a}}_1\hat{\mathbf{a}}_2, \tag{2.38}$$

are the effective second-order nonlinear coefficients. In a lossless medium, due to full permutation symmetry [74], all three effective nonlinear coefficients are equal and can be given by a single real coefficient

$$d_{\text{eff}} = d_1 = d_2 = d_3. \tag{2.39}$$

These three coupled equations [see Equations (2.32), (2.33) and (2.34)] with Equation (2.39) constitute the coupled-mode equations governing the interaction of three waves through a material with second-order nonlinearity for monochromatic waves under the slowly varying envelope approximation.

2.4 Parametric Interactions

For plane waves propagating in the z-direction

$$\mathbf{E}_i(z,t) = \hat{\mathbf{a}}_i \,\text{Re}\left[A_i(z)e^{j\omega_i t - jk_i z}\right], \tag{2.40}$$

where $A_i(z)$ is the slowly varying electric field phasor at an angular frequency ω_i and $i = 1, 2, 3$, the coupled-mode equations take the form of

$$\frac{dA_1(z)}{dz} = -j\frac{\omega_1 d_{\text{eff}}}{cn_1}A_3(z)A_2^*(z)e^{-j\Delta kz}, \tag{2.41}$$

$$\frac{dA_2(z)}{dz} = -j\frac{\omega_2 d_{\text{eff}}}{cn_2}A_3(z)A_1^*(z)e^{-j\Delta kz}, \tag{2.42}$$

$$\frac{dA_3(z)}{dz} = -j\frac{\omega_3 d_{\text{eff}}}{cn_3}A_1(z)A_2(z)e^{j\Delta kz}, \tag{2.43}$$

where

$$\Delta k = k_3 - k_2 - k_1. \tag{2.44}$$

Further simplification can be made using

$$A_1(z) = \sqrt{\frac{2\hbar\omega_1}{n_1 c\epsilon_0}}a_1(z), \tag{2.45}$$

$$A_2(z) = \sqrt{\frac{2\hbar\omega_2}{n_2 c\epsilon_0}}a_2(z), \tag{2.46}$$

$$A_3(z) = -j\sqrt{\frac{2\hbar\omega_3}{n_3 c\epsilon_0}}a_3(z), \tag{2.47}$$

where a_i are the normalized field amplitudes such that $|a_i|^2 = \phi_i$ represent the photon flux densities at each frequency ω_i. A $-90°$ phase shift is imposed on the field at ω_3 to remove "j" from the coupled-mode equations. As a result, the couple mode equations for the normalized fields become

$$\frac{da_1(z)}{dz} = -\kappa a_3(z)a_2^*(z)e^{-j\Delta kz}, \tag{2.48}$$

$$\frac{da_2(z)}{dz} = -\kappa a_3(z)a_1^*(z)e^{-j\Delta kz}, \tag{2.49}$$

$$\frac{da_3(z)}{dz} = \kappa a_1(z)a_2(z)e^{j\Delta kz}, \tag{2.50}$$

where the coupling coefficient is defined as

$$\kappa = d_{\text{eff}}\sqrt{\frac{2\hbar}{c^3\epsilon_0}}\sqrt{\frac{\omega_1\omega_2\omega_3}{n_1 n_2 n_3}}. \tag{2.51}$$

The solution of the coupled-mode equations are well known in terms of Jacobi elliptic functions [14]–[16], [76].

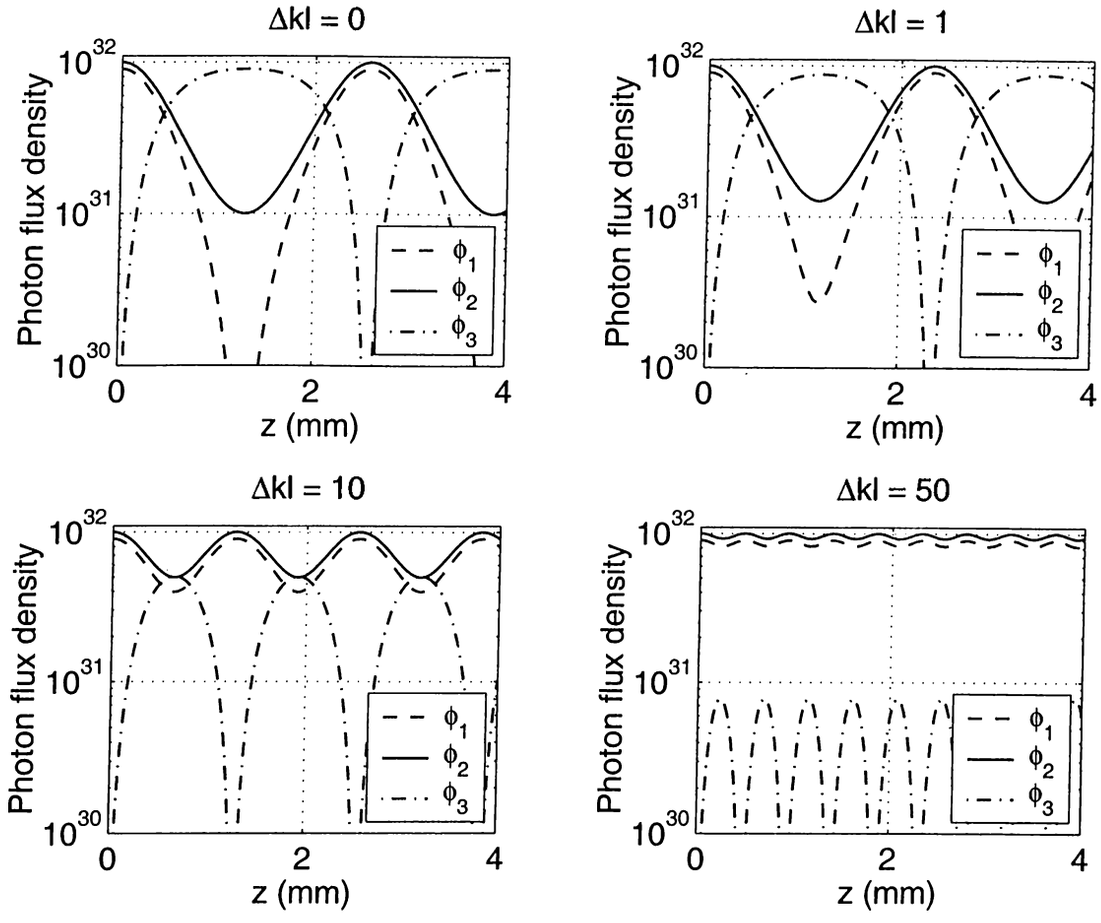

Figure 2.1: Change in photon flux densities for $\Delta kl = 0, 1, 10$ and 50.

2.4.1 Sum-frequency Generation and Phase Matching

Figure 2.1 shows examples of the evolution of photon fluxes of the three fields inside a nonlinear material for SFG. To generate this plot, we used a typical value of $\kappa = 2\times10^{-13}$, the material length of $l = 4$ mm, and $\Delta kl = 0, 1, 10,$ and 50. In this example, the initial conditions of the coupled-mode equations are $\phi_3 = 0$, $\phi_2 = 1 \times 10^{32}$ photons/m^2, and $\phi_1 = 0.9\phi_2$. As the fields propagate, ϕ_3 starts to grow and reaches a maximum, and ϕ_1 and ϕ_2 start to decrease and they reach a minimum. In the subplot with $\Delta kl = 0$, ϕ_3 has the largest value, ϕ_2 has the minimum value and ϕ_1 is totally depleted. This part of the plot is an example of a SFG interaction. After that point, the interaction reverses its direction, back conversion starts, ϕ_1 and ϕ_2 start to grow and reach their initial values, ϕ_3 starts to decrease and reaches its initial value of zero. In this example, for larger Δkl values, the SFG interaction stops earlier in the crystal and the number of photons that are converted from one field to another drops considerably. This example

demonstrates that for efficient transfer of energy between interacting fields, the phase matching condition

$$\Delta k = 0 \tag{2.52}$$

must be satisfied. Such an interaction is said to be phase-matched.

In the transparency range of frequencies, a dispersion curve of the refractive index of a material shows normal dispersion, an increasing behavior with an increase in frequency. This relation together with the frequency condition in Equation (2.11) imply that the phase matching condition is impossible to satisfy [74]. There are two methods used for phase matching despite this. The BPM method uses anisotropic materials. These materials show two different values of refractive index for a single direction of propagation for two orthogonal eigenvectors of polarization direction of an electric field, an effect known as birefringence. In BPM, selection of refractive index values from two different dispersion curves makes it possible to phase match a given interaction [12], [13], [74]. However, QPM method employs periodic phase corrections. In this method, every time the $e^{-j\Delta kz}$ terms in the coupled-mode equations introduces a $-\pi$ phase shift, a correction of π phase is applied by reversing the sign of the nonlinear coefficient along the z axis [14], [77], [78].

In the BPM method, phase matching is possible for three different polarization geometries. In all of there geometries, the third field with the highest frequency must be polarized along the eigenvector that results in smaller refractive index values. Otherwise, phase matching is impossible because of the same reason for isotropic materials. In one of these geometries, the polarization directions of the first and the second fields are the same, and are perpendicular to the polarization direction of the third field. This geometry is called type-I phase matching. In the remaining two geometries, the polarization directions of the first and the second fields are orthogonal to each other and one of them is in the same direction with the polarization direction of the third field. These two geometries are called type-II phase matching. Similar classification can be extended to the QPM case. However, in contrast to BPM, we need not restrict the polarization direction of the third field to the eigenvector with smaller refractive index values.

2.4.2 Difference-frequency Generation

The subplot with $\Delta k = 0$ in Figure 2.1 is also an example of DFG. The point at which back conversion starts corresponds to the starting point of the DFG interaction because the condition of the photon fluxes at that point is equivalent to an initial condition of the coupled-mode equations for DFG at the beginning of the nonlinear material. In this example of DFG, initially $\phi_1 = 0$, $\phi_2 = 1 \times 10^{31}$, and $\phi_3 = 9\phi_2$. As the fields propagate, ϕ_3 starts to decrease and ϕ_2 start to increase, and they generate ϕ_1. Both ϕ_1 and ϕ_2 get energy from ϕ_3. As a result, DFG causes parametric amplification of the second field from its initial condition.

The solution of the coupled-mode equations in terms of Jacobi elliptic functions are phase dependent when all of the initial conditions are nonzero. As a result, when there are three fields at the entrance of the nonlinear material, not only their intensities but

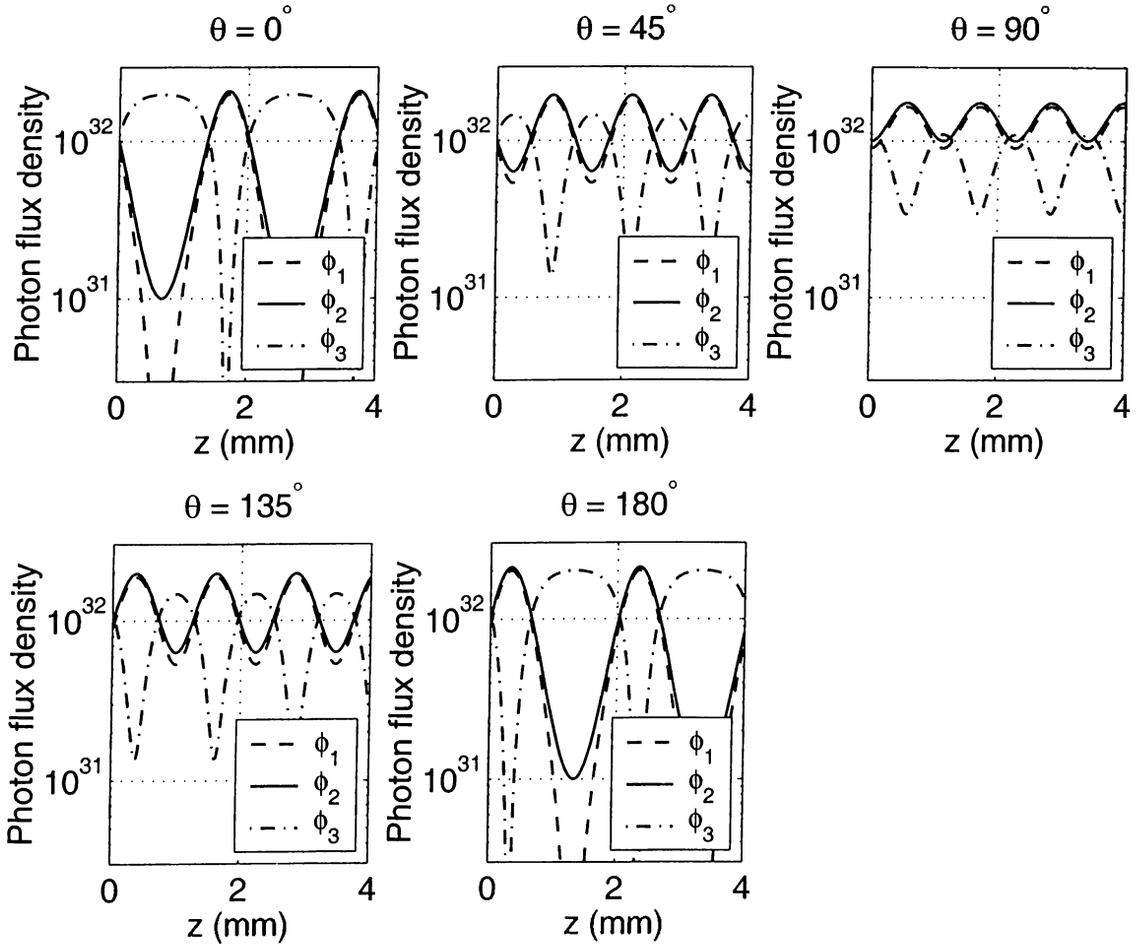

Figure 2.2: Change in photon flux densities for various phase angles.

also their relative phase, given by

$$\theta = \arg a_3(z=0) - \arg a_1(z=0) - \arg a_2(z=0), \tag{2.53}$$

effects the evolution of the field intensities. Figure 2.2 shows an example for relative phases of $\theta = 0°$, $45°$, $90°$, $135°$ and $180°$. In each subplot, we use the initial conditions $\phi_1 = 0.9\phi_2$ and $\phi_3 = 1.1\phi_2$ for a phase-matched ($\Delta k = 0$) interaction. Depending on the relative phase, the first and the second fields start to increase (amplification) or start to decrease (deamplification). Maximum conversion is achieved for $\theta = 0°$ and $\theta = 180°$. In frequency conversion systems, usually one of the fields is missing at the input. This condition results in a phase insensitive interaction in which the missing field adjusts its own phase such that conversion is maximum [76].

2.4.3 Second Harmonic Generation

SHG is a special case of SFG where a fundamental field at a frequency ω generates a field at 2ω. Depending on the phase matching type, the coupled-mode equations of SHG have two different forms. When type-II phase matching is employed, the fundamental field is polarized at a $45°$ angle to the eigenvectors of the polarization direction. Therefore, there are two orthogonal polarization components along the both eigenvectors. The same coupled-mode equations used in SFG are valid for type-II SHG, because the two fundamental components corresponding to the first and the second fields of SFG with $\omega_1 = \omega_2 = \omega$ are distinguished by their polarization directions.

For the type-I case, there is a degeneracy in which one cannot distinguish the first and second fields from each other, because both their polarizations and frequencies are same. Hence, the normalized coupled-mode equations reduce to

$$\frac{da_1(z)}{dz} = -\kappa a_3(z) a_1^*(z) e^{-j\Delta k z}, \tag{2.54}$$

$$\frac{da_3(z)}{dz} = \frac{1}{2}\kappa a_1^2(z) e^{j\Delta k z}, \tag{2.55}$$

where

$$\Delta k = k_3 - 2k_1. \tag{2.56}$$

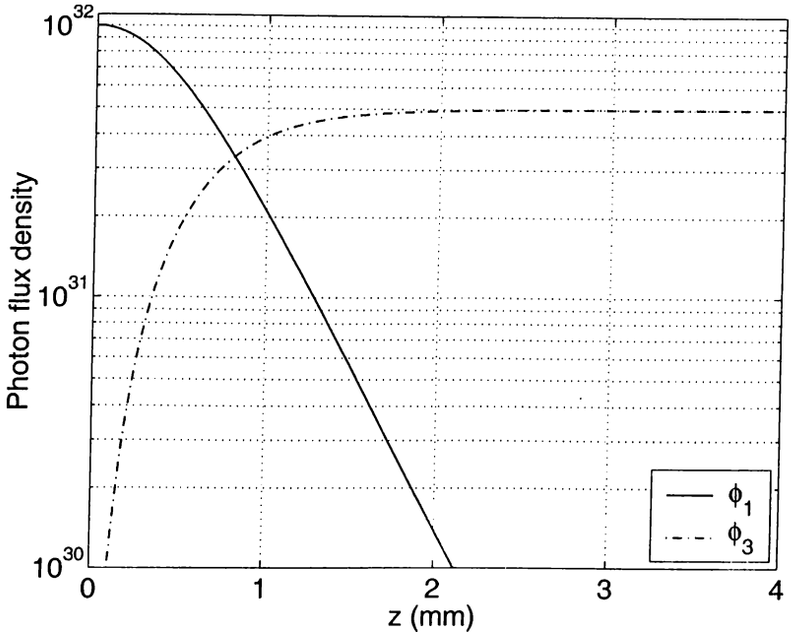

Figure 2.3: Change in photon flux densities for SHG.

Figure 2.3 shows an example of the evolution of photon flux densities of the fundamental and second harmonic fields for initial conditions of $\phi_1 = 1 \times 10^{32}$ photons/m^2 and $\phi_3 = 0$ with $\Delta k = 0$. Although most of the energy from the fundamental field is converted to the second harmonic field in a short distance, the photon flux of the second harmonic field ϕ_3 asymptotically reaches total conversion. Therefore, there is no back conversion in type-I SHG.

2.4.4 Optical Parametric Oscillation

In parametric amplification as described in Section 2.4.2, the third field provides energy to the interaction and is called the pump field, the second field (the signal field) is amplified in the process and the first field is generated as an extra output, and is called the idler field. Parametric gain for the signal field is defined as

$$G = \frac{\phi_2(z = l)}{\phi_2(z = 0)}, \tag{2.57}$$

where l is the length of the nonlinear material in which the interaction takes place. Lack of the idler wave at the input and $\Delta k = 0$ result in

$$G = 1 + m\frac{\mathrm{sn}^2(\sqrt{D}, m)}{\mathrm{dn}^2(\sqrt{D}, m)}, \tag{2.58}$$

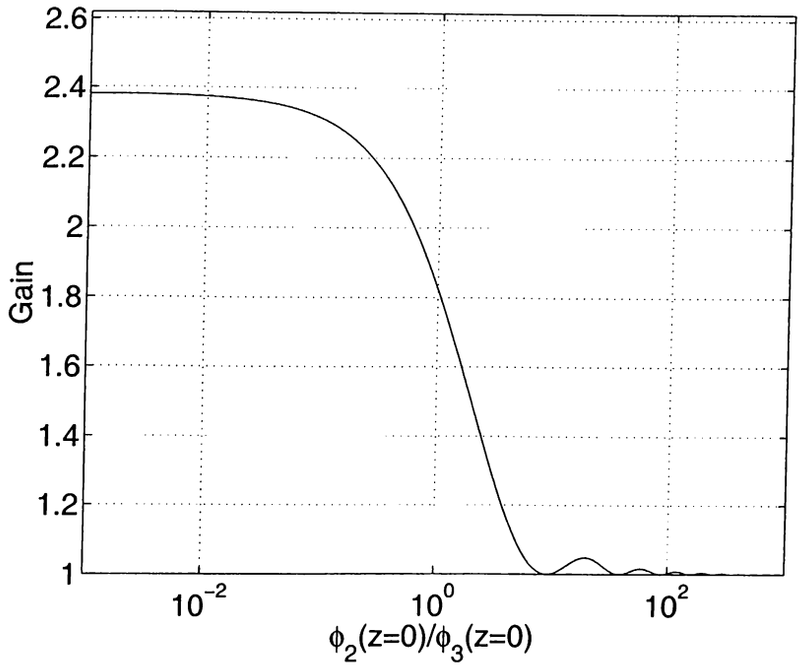

Figure 2.4: Gain saturation with the increase in the signal input.

where

$$D = (\kappa l)^2 \phi_3(z=0) \tag{2.59}$$

is called the nonlinear drive,

$$m = \frac{\phi_3(z=0)}{\phi_3(z=0)+\phi_2(z=0)}, \tag{2.60}$$

and $\mathrm{sn}(x,m)$ and $\mathrm{dn}(x,m)$ are Jacobi elliptic functions [76], [79]. As an example, Figure 2.4 shows the parametric gain G as a function of the ratio of the initial values of the photon flux of the signal and the pump fields. The initial value of the pump field is constant at $\phi_3 = 1 \times 10^{32}$ photons/m^2. The gain starts to saturate and decreases to the limiting value of unity as ϕ_2 increases. Gain provided by a parametric amplifier can be used to make an OPO with help of an optical resonator.

When the OPO resonator is singly-resonant, it provides positive feedback only for the signal wave. As a result, only the signal and the the pump waves are nonzero at the input of the parametric amplifier. This situation allows a phase insensitive operation of the OPO.

The steady-state operation point of an OPO is determined by the amplifier gain and the resonator losses. At the limiting value of small signal field ($\lim \phi_2(z=0) \to 0$)), the

unsaturated gain is given by

$$G_0 = \cosh^2(\sqrt{D}), \tag{2.61}$$

in plane wave theory. Oscillation will not start unless the unsaturated gain can compensate for the resonator losses. The unsaturated gain which can compensate for the resonator losses determines the threshold intensity of the pump field. Above this intensity, the signal field starts to grow and reaches a level where the saturated gain just compensates the resonator losses. As a result, given the nonlinear drive D and the resonator losses, the intensity of the signal field oscillating inside the OPO resonator can be found using Equation (2.58).

In order to reach high gain that compensate more loss, high nonlinear drive D is necessary. In addition to high intensity of pump field and long nonlinear materials, we need high coupling coefficient κ to get this high nonlinear drive D [see Equation (2.59)]. The coupling coefficient [see Equation (2.51)] consists of material dependent parameters of the refractive indices and the effective nonlinear coefficient d_{eff}. Although the values of the refractive indices do not change much with the propagation directions and the polarization directions of the three fields, the effective nonlinear coefficient has a strong dependence on these parameters through the second-order nonlinear susceptibility tensor [see Equations (2.36)–(2.39)]. Thus, the effective nonlinear coefficient is another important parameter, like the phase mismatch, in the design of a device employing a three-wave mixing process.

The solutions of the coupled-mode equations for three-wave mixing show that the phase matching condition represented by Equation (2.52) must be satisfied for efficient transfer of energy between the interacting fields. The effective nonlinear coefficient is also an important parameter. The coupling coefficients, hence the nonlinear drive, depend on the effective nonlinear coefficient. With high values of the effective nonlinear coefficient, one can reach high values of nonlinear drive with less intensity and shorter nonlinear materials.

2.5 Simultaneously Phase-matched Interactions

In general, various nonlinear interactions take place simultaneously inside a nonlinear material. However only phase-matched interactions can result in considerable exchange of energy between the fields. In the previous section, we considered a single interaction at a time, but it is possible to simultaneously satisfy the phase matching condition for two or more interactions for the same direction of propagation. By this way, One may provide decrease in system complexity and more efficient energy conversion etc. In this thesis, we investigate experimental situations where simultaneous phase matching of optical parametric oscillation together with SHG or SFG is achieved using BPM or QPM [3]–[10].

In order to achieve tunable frequency upconversion of laser radiation, one needs optical parametric oscillation together with SHG or SFG. There are various examples that use two nonlinear crystals for parametric oscillation and SHG or SFG [34]–[39]. The second crystal that is used for SHG or SFG increases the system complexity and in some experiments makes the design of the OPO cavity difficult. In contrast, we use a single nonlinear crystal employing simultaneous phase matching in SD-OPO and SF-OPO experiments in Chapter 5 and 6. As a result, only OPO cavity design is necessary without any further modification. For example, if we compare our femtosecond SD-OPO experiments with our intracavity-doubled femtosecond OPO experiments in Chapter 5, our intracavity-doubled femtosecond OPO experiments has an extra intracavity focus provided with two extra mirrors. In addition to bring some design difficulties, these extra component and the second crystal also introduces additional loss into the OPO cavity.

Class	Rotation	OPO	SHG
A	no	type-I type-II	type-I
B	yes	type-II	type-I
C	yes	type-I type-II	type-II

Table 2.1: Phase matching geometries for SD-OPO.

Class	Rotation	OPO	SFG
A	none	type-I type-II	type-II
B	both	type-I type-II	type-II
C	pump	type-I type-II type-II	type-I type-I type-II
D	signal	type-II	type-II

Table 2.2: Phase matching geometries for SF-OPO.

Plane wave SD-OPO and SF-OPO interactions were classified and analyzed by Aytür *et al.* [42] and Dikmelik *et al.* [43]. These classifications of SD-OPOs and SF-OPOs are based on the polarization state of the interactions. Tables 2.1 and 2.2 show these classification of SD-OPOs and SF-OPOs. For class-B and class-C SD-OPOs, and class-B and class-D SF-OPOs, a rotation of the polarization of the intracavity signal field is necessary to achieve SHG or SFG. In addition to this, a rotation of the pump polarization is necessary for class-B and class-C SF-OPOs to achieve SFG. In our experiments, we designed SD-OPOs and a SF-OPO based on various nonlinear crystals and demonstrated class-A and class-C SD-OPOs and a class-C SF-OPO [4], [7], [8].

In our class-A SD-OPO, we employ type-I phase matching for both optical parametric oscillation and SHG. The signal and the fundamental fields are the same, and SHG is governed by Equations (2.54) and (2.55). The combined coupled-mode equations are

$$\frac{da_1(z)}{dz} = -\kappa_a a_3(z) a_2^*(z) e^{-j\Delta k_a z}, \tag{2.62}$$

$$\frac{da_2(z)}{dz} = -\kappa_a a_3(z) a_1^*(z) e^{-j\Delta k_a z} - \kappa_b a_6(z) a_2^*(z) e^{-j\Delta k_b z}, \tag{2.63}$$

$$\frac{da_3(z)}{dz} = \kappa_a a_1(z) a_2(z) e^{j\Delta k_a z}, \tag{2.64}$$

$$\frac{da_6(z)}{dz} = \frac{1}{2}\kappa_b a_2^2(z) e^{j\Delta k_b z}, \tag{2.65}$$

where κ_a and κ_b are the coupling coefficients of the optical parametric oscillation and SHG interactions, and indices 1, 2, 3, and 6 represents the idler, the signal, the pump, and the second harmonic fields, respectively.

In our class-C SD-OPO, we employ type-II phase matching both for both optical

parametric oscillation and SHG. The OPO generates a signal field with a polarization direction along only one of the eigenvectors. To have both fundamental field components, we couple some of the signal field inside the cavity to the other orthogonal polarization by linear polarization rotation element. The combined coupled-mode equations are

$$\frac{da_1(z)}{dz} = -\kappa_a a_3(z) a_2^*(z) e^{-j\Delta k_a z}, \tag{2.66}$$

$$\frac{da_2(z)}{dz} = -\kappa_a a_3(z) a_1^*(z) e^{-j\Delta k_a z} - \kappa_b a_6(z) a_5^*(z) e^{-j\Delta k_b z}, \tag{2.67}$$

$$\frac{da_3(z)}{dz} = \kappa_a a_1(z) a_2(z) e^{j\Delta k_a z}, \tag{2.68}$$

$$\frac{da_5(z)}{dz} = -\kappa_b a_6(z) a_2^*(z) e^{-j\Delta k_b z}, \tag{2.69}$$

$$\frac{da_6(z)}{dz} = \kappa_b a_2(z) a_5(z) e^{j\Delta k_b z}, \tag{2.70}$$

where indices 1, 2, 3, 5, and 6 represents the idler, the signal, the pump, the rotated signal, and the second harmonic fields, respectively.

Our class-C SF-OPO has the same combined coupled-mode equations as the class-C SD-OPO. We again employ type-II phase matching for both optical parametric oscillation and SFG. In this case, our OPO generates a signal field that is polarized along the same direction with the pump field and for type-II SFG, we need a pump field polarized orthogonal to the signal field and provide this field by coupling some of the pump to the other polarization by an extracavity linear polarization rotation element. As a result, indices 1, 2, 3, 5, and 6 represents the idler, the signal, the pump, the rotated pump and the sum frequency fields respectively.

Although, analytic solutions of the combined coupled-mode equations [see Equations (2.62)–(2.70)] do not exist as in the case of a single interaction [42],[43], the behavior of SD-OPO and SF-OPO interactions can still be characterized by the nonlinear drive of the OPO

$$D = (\kappa_a l)^2 \phi_3(z=0), \tag{2.71}$$

and the ratio of the coupling coefficients

$$\beta = \frac{\kappa_b}{\kappa_a}, \tag{2.72}$$

which represents how strong those two interaction coupled together. The intensity of the intracavity signal field can be found when the resonator losses and the angle

of polarization rotations are given. Plane wave analysis of SF-OPOs [43] show that depending on the nonlinear drive, β, and polarization rotation, SF-OPOs sometimes show period doubling and chaotic behavior.

In this chapter, we briefly presented the theory of optical parametric interactions. With this background information, we discussed the importance of the phase matching condition and the effective nonlinear coefficient. In addition, to complete the theoretical background on our experiments, we presented the combined coupled-mode equations that describe the simultaneous nonlinear interactions.

Chapter 3

Phase Matching

As mentioned in the previous chapter, solutions of the coupled-mode equations of three-wave mixing show that, for efficient transfer of energy between the interacting waves, the phase matching condition $\Delta k = 0$ must be satisfied. There are two methods to phase match an interaction, namely BPM and QPM. In this chapter, we present these two methods as background information with a discussion on the phase matching equation. In addition, we introduce the simultaneous phase matching concept and our methods of simultaneous BPM and QPM.

3.1 Birefringent Phase Matching

Birefringence is an effect shown by anisotropic materials. Anisotropic materials show two different values of refractive index for a single direction of propagation for two orthogonal eigenvectors of polarization direction [74], [80]–[89]. Unlike isotropic materials, these refractive indices also depend on the propagation direction. Depending on the phase velocity corresponding to each eigenvector, these two refractive indices are called "fast" or "slow" refractive indices [86]. Similarly, directions corresponding to the polarization eigenvectors are called "slow-axis" or "fast-axis." There are eight possible polarization combinations for second-order nonlinear interactions of three waves due to two possible polarization directions of each wave and each of them has a different phase mismatch

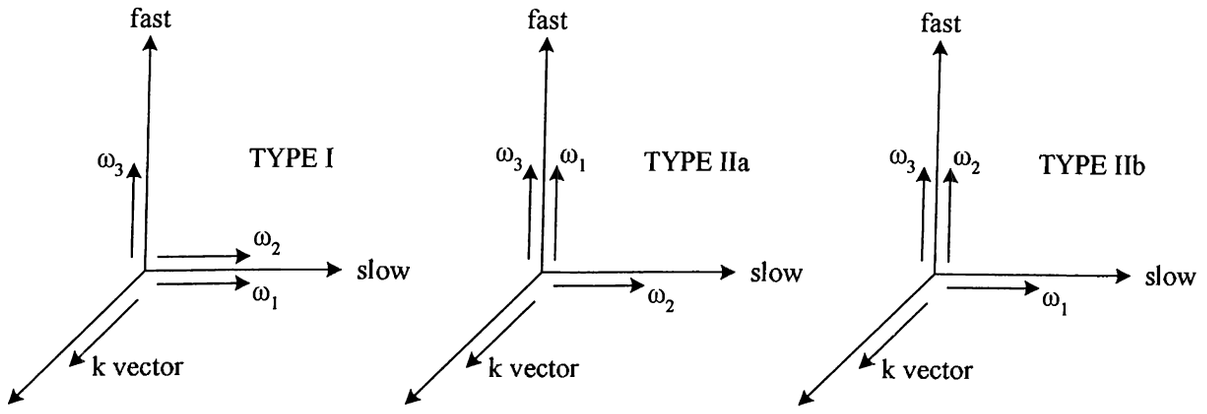

Figure 3.1: Directions of polarizations for ω_1, ω_2, and ω_3 for type-I and type-II phase matching in the three-wave mixing ($\omega_1 + \omega_2 = \omega_3$).

value.

The simplest geometry for the interacting waves is the collinear propagation in which all of the wavevectors are in the same direction of propagation. In this case, the phase matching condition takes a scalar form [see Equation (2.44)], and it is possible only for three of the eight polarization configurations shown in Figure 3.1 to satisfy the phase matching condition [83]. The common part in the polarization geometries in Figure 3.1 is that the wave at the highest frequency ω_3 is polarized along the fast-axis. Other configurations, in which either all the polarizations are the same or the wave at the highest frequency ω_3 is polarized along the slow-axis, cannot be phase-matched. The reason for this is equivalent to the reason for the phase matching condition in the isotropic materials not to be satisfied; the dispersion curve of each of the slow or fast refractive indices shows normal dispersion and, similar to the case of the isotropic materials, it is impossible to satisfy the phase matching condition [74]. Open forms of the phase matching condition [see Equation (2.44)] for these three cases are

$$n_f(\omega_3)\omega_3 - n_s(\omega_2)\omega_2 - n_s(\omega_1)\omega_1 = 0, \tag{3.1}$$

$$n_f(\omega_3)\omega_3 - n_s(\omega_2)\omega_2 - n_f(\omega_1)\omega_1 = 0, \tag{3.2}$$

$$n_f(\omega_3)\omega_3 - n_f(\omega_2)\omega_2 - n_s(\omega_1)\omega_1 = 0, \tag{3.3}$$

where n represents the refractive index, and subscripts f and s are the abbreviations for "fast" and "slow." These polarization configurations are referred to as type-I, type-IIa, and type-IIb, (or type-I, type-II and type-III) respectively [74], [80], [82]-[84], [86].

In a more complex geometry, the wavevectors of the three waves are not in the same direction and the phase matching equation is a vector equation [see Equation (2.35)]. This is called non-collinear phase matching. For this case, there are some situations where the phase matching condition is satisfied for the forbidden cases of collinear phase matching [87], i.e., one can employ any one of the eight possible combinations, because different propagation directions result in different dispersion curves.

It is important to have freedom in choosing a particular polarization geometry, because the effective nonlinear coefficient d_{eff} can be maximized using this freedom. In other words, different polarization geometries for all of which $\Delta k = 0$, usually have different effective nonlinear coefficients. Although non-collinear phase matching provides greater freedom [87], it has a big disadvantage. In non-collinear phase matching, the interaction length is restricted by the overlap volume of the three waves inside a nonlinear material, since in nonlinear frequency conversion systems, a wave provided by a laser source or a wave oscillating inside a cavity form a beam of limited transverse extent.

3.2 Quasi-Phase Matching

As we discussed in Chapter 2, the phase mismatch Δk effects the nonlinear driving terms in Equations (2.41)–(2.43). A distance $\Delta l = \pi/\Delta k$ of a travel in the z-direction changes the sign of the term $e^{-j\Delta kz}$. If one applies π radians phase corrections at the end of distance Δl of every travel, there can be an efficient energy conversion.

A phase shift of π radians can be obtained by passing the three waves into another nonlinear material of the same type, whose crystalline orientation is obtained by the inversion of the first material. As a result, the sign of the nonlinear coefficient is changed and the signs of the nonlinear driving terms are corrected in the second material. Although the interaction is not phase-matched in the usual sense, when this method is repeatedly applied whenever necessary, there can be an efficient energy conversion like a phase-matched interaction. This is called QPM.

One of the methods used to form a sequence of inverted crystal structure of a nonlinear material is electric field poling. In this method, a high voltage pulse is applied to

electrodes formed by lithographic processes on a nonlinear crystal. The voltage pulse creates a high electric field under the electrodes that can alter the crystalline structure of the material directly underneath. As a result, inverted crystal regions (inverted domains) that modulate the sign of the nonlinear coefficient in the direction of propagation can be permanently formed [21].

The resulting nonlinear coefficient $d(z) = g(z)d_{\text{eff}}$ is a function of distance z, where $g(z)$ is the grating modulation function that can only take values of $+1$ or -1. A periodic grating function with period Λ can be expressed as a Fourier series

$$g(z) = \sum_{p=-\infty}^{\infty} G_p e^{jk_p z}, \tag{3.4}$$

where G_p are the Fourier series coefficients, k_p are the magnitude of the grating vector of the pth Fourier component and

$$k_p = \frac{2\pi p}{\Lambda}. \tag{3.5}$$

Replacing d_{eff} by $d(z)$, the coupled-mode equations [see Equations (2.41)–(2.43)] become

$$\frac{dA_1(z)}{dz} = -j\frac{\omega_1 d_{\text{eff}} G_q}{cn_1} A_3(z)A_2^*(z) - j\frac{\omega_1 d_{\text{eff}}}{cn_1} A_3(z)A_2^*(z) \sum_{p=-\infty, p\neq q}^{\infty} G_p e^{-j(\Delta k - k_p)z}, \tag{3.6}$$

$$\frac{dA_2(z)}{dz} = -j\frac{\omega_2 d_{\text{eff}} G_q}{cn_2} A_3(z)A_1^*(z) - j\frac{\omega_1 d_{\text{eff}}}{cn_2} A_3(z)A_1^*(z) \sum_{p=-\infty, p\neq q}^{\infty} G_p e^{-j(\Delta k - k_p)z}, \tag{3.7}$$

$$\frac{dA_3(z)}{dz} = -j\frac{\omega_3 d_{\text{eff}} G_q}{cn_3} A_1(z)A_2(z) - j\frac{\omega_3 d_{\text{eff}}}{cn_3} A_1(z)A_2(z) \sum_{p=-\infty, p\neq q}^{\infty} G_p e^{j(\Delta k - k_p)z}, \tag{3.8}$$

where

$$\Delta k = k_3 - k_2 - k_1 \tag{3.9}$$

when

$$k_q = \Delta k. \tag{3.10}$$

Over many periods of the inverted crystal structure, only one second-order interaction that is satisfies Equation (3.10) results in efficient conversion. This is a quasi-phase-matched interaction and Equation (3.10) is a modified version of the phase-matching equation including QPM with the additional term k_q. We can ignore non-phase-matched components in Equations (3.6) to and the coupled-mode equations approximating the

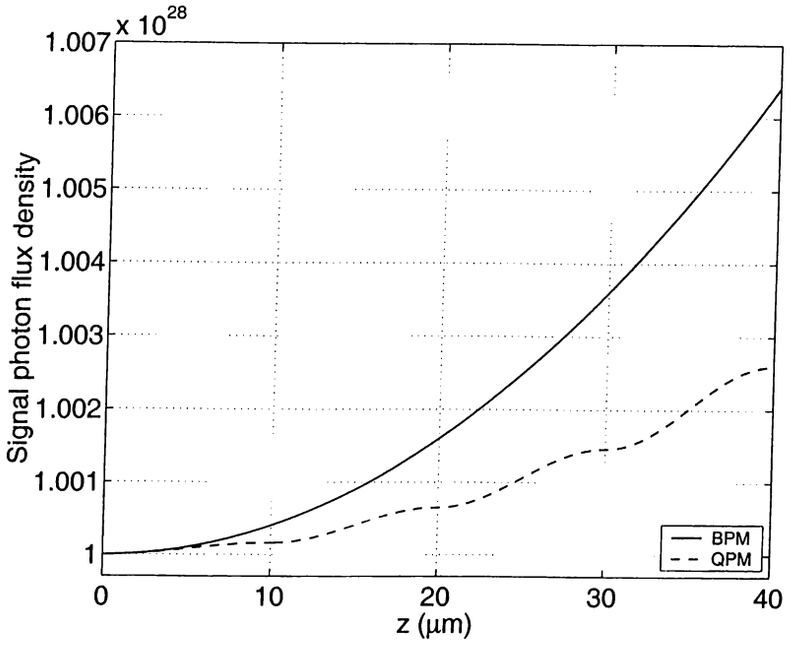

Figure 3.2: A phase-matched parametric amplification using BPM and QPM. First 4 cycles of quasi-phase-matched interaction is shown.

quasi-phase-matched interaction are

$$\frac{dA_1(z)}{dz} = -j\frac{\omega_1 d_{\text{eff}} G_q}{cn_1} A_3(z) A_2^*(z), \tag{3.11}$$

$$\frac{dA_2(z)}{dz} = -j\frac{\omega_2 d_{\text{eff}} G_q}{cn_2} A_3(z) A_1^*(z), \tag{3.12}$$

$$\frac{dA_3(z)}{dz} = -j\frac{\omega_3 d_{\text{eff}} G_q}{cn_3} A_1(z) A_2(z). \tag{3.13}$$

These approximate equations and the coupled-mode equations [see Equations (2.41)–(2.43)] with $\Delta k = 0$ are same except for the Fourier series coefficient G_q.

Figure 3.2 shows an example of evolution of the signal field of a parametric amplifier in a material with and without periodic poling. In the poled crystal, the interaction is phase-matched using QPM for $q = 1$ and the period $\Lambda = 20$ μm and the other crystal employs BPM. Although the amplifiers using BPM and QPM have the same d_{eff}, the energy conversion in poled crystal is low due to G_q. Since the maximum value of the Fourier coefficients is $|G_1| = 2/\pi$ which is less than unity, the quasi-phase-matched interactions always have a penalty.

QPM has important advantages over BPM in spite of its penalty. The additional grating vector k_q in Equation (3.10) is used to satisfy any phase matching condition

without any restrictions to the polarization states of the interacting waves. QPM is achieved by adjusting the period Λ so that the natural phase mismatch $\Delta k = k_3 - k_2 - k_1$ is canceled by one of the Fourier components of the grating function [21],[77]. As a result, with a choice of $\Lambda = 2\pi q/(k_3 - k_2 - k_1)$, the QPM condition can be satisfied for each configuration of the polarizations of the three waves. Usually, the interacting waves have the same polarization direction in QPM because the largest element of the nonlinear coefficient tensor is a diagonal element for common crystals such as lithium niobate, and such a polarization arrangement facilitates the use of the largest nonlinear coefficient ($\overleftrightarrow{\chi}^{(2)}_{ZZZ}$ for lithium niobate). In addition, it is common practice to set Λ to a value that will satisfy Equation (3.10) for $q = 1$ (first-order QPM) and set the duty-cycle of the grating modulation function to 50%. Therefore, $d_{\text{eff}}G_q$ is maximized.

3.3 Calculation of Phase Matching Curves

In this section, we derive a general equation that we use to calculate the phase matching curves (or tuning curves). The phase matching condition in Equation (3.10) is different from the usual phase matching equation [see Equation (2.52)]; it includes a grating momentum k_q. For BPM, this grating momentum term is zero. From this point of view Equation (3.10) is more general than Equation (2.52).

In general, the interacting waves do not necessarily propagate in the same direction (noncolinear propagation) in addition their propagation direction might not coincide with the direction of grating. Therefore, the general form of the phase matching condition in Equation (3.10)

$$\mathbf{k}_q = \mathbf{k}_3 - \mathbf{k}_2 - \mathbf{k}_1 \tag{3.14}$$

is a vector equation where $\mathbf{k}_q$ is the qth grating momentum vector defined by

$$\mathbf{k}_q = \frac{2\pi}{\Lambda}\hat{\mathbf{a}}_\mathbf{q}, \tag{3.15}$$

where $\hat{\mathbf{a}}_\mathbf{q}$ is a unit vector showing the direction of the grating. A wavevector inside a material is given by

$$\mathbf{k} = \frac{\hat{\mathbf{a}}(\theta,\phi)n_r(\theta,\phi,\omega)\omega}{c}, \tag{3.16}$$

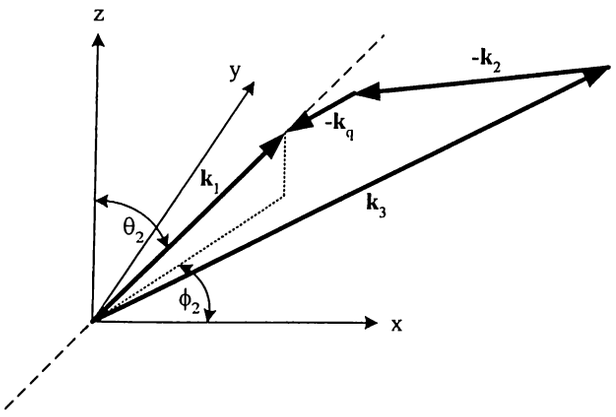

Figure 3.3: The direction of the first wavevector is determined by the other vectors if the phase matching condition is assumed to be satisfied.

where $\hat{\mathbf{a}}$ is a unit vector showing the direction of propagation in spherical coordinates θ and ϕ in the reference frame of the material. The refractive index n of an anisotropic material is depend on the direction of propagation and the polarization direction of the field. The polarization direction is taken into account by the subscript r representing the fast-axis or slow-axis. Phase matching curves show the relation between various parameters of the wavevectors. Therefore, in this problem, we wish to determine the frequencies and the angles θ and ϕ that satisfies Equation (3.14).

Given the polarization geometry (phase matching type) for a crystal with a grating structure that results in a grating vector $\mathbf{k}_p$, the phase matching condition can be represented by three scalar equations written in terms of the components of the wavevectors [87]

$$n_{1,r_1}a_{1x}\omega_1 + n_{2,r_2}a_{2x}\omega_2 - n_{3,r_3}a_{3x}\omega_3 = -k_{qx}c, \tag{3.17}$$

$$n_{1,r_1}a_{1y}\omega_1 + n_{2,r_2}a_{2y}\omega_2 - n_{3,r_3}a_{3y}\omega_3 = -k_{qy}c, \tag{3.18}$$

$$n_{1,r_1}a_{1z}\omega_1 + n_{2,r_2}a_{2z}\omega_2 - n_{3,r_3}a_{3z}\omega_3 = -k_{qz}c. \tag{3.19}$$

Figure 3.3 shows the geometric interpretation of the problem. Imposing the frequency condition $\omega_3 = \omega_1 + \omega_2$ and introducing a constant $\tau = \omega_1/\omega_3$, we can rewrite Equations (3.17)–(3.19) and define three values, ρ_x, ρ_y and ρ_z as

$$\rho_x = \tau n_{1,r_1}a_{1x} = n_{3,r_3}a_{3x} - (1-\tau)n_{2,r_2}a_{2x} - k_{qx}c/\omega_3, \tag{3.20}$$

$$\rho_y = \tau n_{1,r_1}a_{1y} = n_{3,r_3}a_{3y} - (1-\tau)n_{2,r_2}a_{2y} - k_{qy}c/\omega_3, \tag{3.21}$$

$$\rho_z = \tau n_{1,r_1}a_{1z} = n_{3,r_3}a_{3z} - (1-\tau)n_{2,r_2}a_{2z} - k_{qz}c/\omega_3. \tag{3.22}$$

Using these values, we can find the angles θ_1 and ϕ_1 for the second wave as a function of the angles of the first and the third waves using

$$\cos^2\phi_1 = \frac{\rho_x^2}{\rho_x^2+\rho_y^2}, \tag{3.23}$$

$$\sin^2\phi_1 = \frac{\rho_y^2}{\rho_x^2+\rho_y^2}, \tag{3.24}$$

$$\cos^2\theta_1 = \frac{\rho_z^2}{\rho_x^2+\rho_y^2+\rho_z^2}, \tag{3.25}$$

$$\sin^2\theta_1 = \frac{\rho_x^2+\rho_y^2}{\rho_x^2+\rho_y^2+\rho_z^2}, \tag{3.26}$$

and their solution

$$\theta_1 = \Theta_1(\theta_2,\phi_2,\theta_3,\phi_3), \tag{3.27}$$

$$\phi_1 = \Phi_1(\theta_2,\phi_2,\theta_3,\phi_3). \tag{3.28}$$

As a result, we can reduce our problem to a single scalar equation

$$n_{1,r_1}\tau + (1-\tau)n_{2,r_2}\mathbf{a}_2\cdot\mathbf{a}_1 - n_{3,r_3}\mathbf{a}_3\cdot\mathbf{a}_1 = -\mathbf{k}_p\cdot\mathbf{a}_1/\omega_3, \tag{3.29}$$

and six unknowns θ_2, ϕ_2, θ_3, ϕ_3, τ, and ω_3. For example, by specifying ω_3, ω_2 (as a result τ) and the direction in which the third beam is propagating, one can find curves for the directions of the first beam; or by specifying the directions of both the first and the third beams, one can find curves relating ω_3 and ω_2, hence ω_1.

A collinear propagation case is a special case in which all directions of the wavevectors are the same i.e.,

$$\theta_1 = \theta_2 = \theta_3 \tag{3.30}$$

and

$$\phi_1 = \phi_2 = \phi_3. \tag{3.31}$$

As a result, we have four unknowns in this case, namely θ_1, ϕ_1, ω_2, and ω_3; by specifying two of these, we can find curves relating the remaining two. For example, by specifying θ_1 and ϕ_1 (collinear propagation direction), we can find tuning curves relating the frequencies ω_2 and ω_3, hence ω_1 for an interaction.

The general convention in the selection of the reference frame of the crystal is such that only the diagonal elements of the linear susceptibility tensor are nonzero. This

rectangular coordinate system defines the principal axes of the crystal, and is referred to by lower case x, y and z [80]. The refractive indices and the nonzero elements of the linear susceptibility tensor are related by

$$\overline{\overline{\chi}}^{(1)}_{xx} = n_x^2 - 1, \tag{3.32}$$

$$\overline{\overline{\chi}}^{(1)}_{yy} = n_y^2 - 1, \tag{3.33}$$

$$\overline{\overline{\chi}}^{(1)}_{zz} = n_z^2 - 1. \tag{3.34}$$

The refractive indices n_x, n_y and n_z are known as the principal refractive indices, and their frequency and temperature dependent values are provided by Sellmeier equations. These equations are numerical fits of experimental measurements of refractive index data for a range of frequencies and temperatures. When the values of all three principle refractive indices are different, the crystal is called biaxial. If only two of the indices are the same, the crystal is called uniaxial. By convention, the labeling of the axes satisfies

$$n_x \leq n_y \leq n_z, \tag{3.35}$$

but the naming of the coordinate system in which the spherical coordinates θ and ϕ are defined is not always consistent with this convention [80].

The rectangular coordinate system in which the second-order nonlinear susceptibility tensor is reported can also be different than the principle coordinate system and the reference frame of the crystal. Axes of this coordinate system are labeled by upper case X, Y and Z. It is important to note coordinate system differences when calculating d_{eff}. In this thesis, we obey IEEE/ANSI standard definitions for the coordinate system of nonlinear crystals. Detailed investigation of conventions, and information on refractive index calculations and the polarization directions of corresponding eigenvectors can be found in [74], [80]–[89].

In this section, we derived a general equation for the calculation of phase matching curves. In this equation, using the directions of the wavevectors and the frequencies, one needs to calculate refractive indices for the polarization geometry at hand. The directions and the tensors necessary for these calculations are defined in rectangular coordinate systems. The relation between these coordinate systems and the calculations of the refractive index for a given direction of propagation can be found in [74], [80]–[89].

3.4 Simultaneous Phase Matching

When two separate processes are simultaneously phase-matched, the phase-mismatch terms of both processes

$$\Delta k_a = k_3 - k_1 - k_2 \tag{3.36}$$

$$\Delta k_b = k_6 - k_4 - k_5 \tag{3.37}$$

have to vanish for the same direction of propagation and for the same temperature within the crystal. Here a and b denote the two parametric processes and process b is associated with waves at frequencies ω_4, ω_5 and ω_6. These are general expressions of phase mismatch and due to the nature of the interaction, one or two waves and/or some frequency values might be the same.

3.4.1 Simultaneous Phase Matching with BPM

In BPM of a single nonlinear process, the interacting waves have different polarization directions. When two processes are phase-matched simultaneously with BPM, a number of different polarization configurations are possible. In general, these polarization configurations can be grouped into various classes depending on the common waves in the processes, and each class being governed by a different set of coupled-mode equations [42], [43].

If possible, for the same direction of propagation, tuning curves relating the frequencies of two simultaneously-phase-matched processes can be found using the phase matching conditions

$$\Delta k_a = 0, \tag{3.38}$$

$$\Delta k_b = 0. \tag{3.39}$$

As we explained in Section 3.3, for a collinear propagation direction, we can find tuning curves relating any two frequencies of each individual processes. However, we need tuning curves relating the frequencies that are common to both interactions for simultaneous phase matching. There are two different cases; when a single frequency is common for

the two processes, we may find continuous curves relating the frequencies of the first interaction to the frequencies of the second interaction; when we relate the common frequency ω_c to one of the remaining two frequencies of the first process ($\omega_{a,1}$ and $\omega_{a,2}$) by a function $\omega_c = f_k(\omega_{a,k})$ where k=1,2 using Equation (3.29), we may have continuous range of values for both ω_c and $\omega_{a,k}$. Similarly, when we relate the common frequency ω_c to one of the remaining two frequencies of the second process ($\omega_{b,1}$ and $\omega_{b,2}$) by a function $\omega_{b,m} = g_m(\omega_c)$ where m=1,2, the continuous $\omega_{a,k}$ values may map to a continuous values $\omega_{b,m}$ with the composite function $\omega_{b,m} = g_m(f_k(\omega_{a,k}))$. Simultaneous phase matching for a SD-OPO belong to this case. Although the optical parametric oscillation interaction provides a continuous range of frequencies for the signal wave, SHG of the signal wave occurs at discrete frequencies at the same direction of propagation. Therefore, simultaneously-phase-matched processes of SD-OPO occur at discrete frequencies for a given direction.

The second case is when there are two common frequencies between the two processes. Simultaneous phase matching occurs at discrete points. When we relate the first common frequency $\omega_{c,1}$ to the other common frequency $\omega_{c,2}$ through the first process by a function $\omega_{c,1} = h_a(\omega_{c,2})$ using Equation (3.29), we may have continuous range of values for both $\omega_{c,1}$ and $\omega_{c,2}$. Similarly, when we relate the first common frequency $\omega_{c,1}$ to the other one through the second process by a function $\omega_{c,1} = h_b(\omega_{c,2})$, we can find solution for $\omega_{c,1}$ and $\omega_{c,2}$ at the intersection points of the two curves represented by the functions $h_a(\omega)$ and $h_b(\omega)$. Simultaneous phase matching for a SF-OPO belong to this case because the signal and the pump waves are both common to parametric oscillation and SFG. Therefore, there are only a few handfuls of processes and wavelengths that provide simultaneous phase matching for SD-OPO and SF-OPO for common nonlinear crystals using BPM.

3.4.2 Simultaneous Phase Matching with Periodic QPM

In QPM, the phase matching of the first process is satisfied by selecting a proper grating period Λ as explained in Section 3.2. Simultaneous phase matching of a second process is possible only if the phase-mismatch term of the second process Δk_b happens to coincide with one of the non-zero harmonics of the grating modulation function. More generally,

higher-order simultaneous phase matching with a periodic grating is possible only when both

$$\Delta k_a = \frac{2\pi}{\Lambda} p \tag{3.40}$$

$$\Delta k_b = \frac{2\pi}{\Lambda} q \tag{3.41}$$

are satisfied for some particular set of Λ, and integer p and q. Although we can phase match any arbitrary interaction in QPM, it is not possible to achieve simultaneous phase matching with periodic gratings for two arbitrary phase-mismatch terms Δk_a and Δk_b.

For the same direction of propagation and grating period Λ, tuning curves relating the frequencies of the two processes can be found using the phase matching conditions in Equations (3.40) and (3.41) in a similar way in Section 3.4.1 for a particular values of p and q. For the simple case of a square wave grating function with variable duty cycle, if one can find a simultaneously-phase-matched processes for Λ, $p \neq 1$, and $q \neq 1$, the interaction will be weak. Although we have different values of the ratio β of coupling coefficients for different values of p and q, another handicap of this periodic grating is that the ratio of the effective nonlinear coefficients

$$\frac{d_{Qb}}{d_{Qa}} = \left|\frac{G_q}{G_p}\right|, \tag{3.42}$$

which is proportional to the ratio β of coupling coefficients, cannot be adjusted freely without severe degradation in the absolute values of the Fourier series coefficients.

3.4.3 Simultaneous Phase Matching with Aperiodic QPM

We found that it is possible to satisfy any simultaneous phase matching for two arbitrary processes with a predefined β using an aperiodic grating structure. An aperiodic grating function can be expressed as

$$g(z) = \frac{l_c}{2\pi} \int_{-\infty}^{\infty} G(\Delta k) \exp(j\Delta k\, z)\, d(\Delta k), \tag{3.43}$$

where

$$G(\Delta k) = \frac{1}{l_c} \int_0^{l_c} g(z) \exp(-j\Delta k\, z)\, dz \tag{3.44}$$

is the normalized Fourier transform in Δk domain, and l_c is the length of the crystal in which the inverted domains are formed. Simultaneous phase matching is achieved when $|G(\Delta k)|$ has peaks located at both Δk_a and Δk_b in the transform domain. The effective nonlinear coefficients are given by

$$d_{Qa} = |G(\Delta k_a)||d_{\text{eff}}|, \tag{3.45}$$

$$d_{Qb} = |G(\Delta k_b)||d_{\text{eff}}|, \tag{3.46}$$

and their ratio is

$$\frac{d_{Qb}}{d_{Qa}} = \left|\frac{G(\Delta k_b)}{G(\Delta k_a)}\right|. \tag{3.47}$$

The total energy of the grating function

$$\int_{-\infty}^{\infty} |G(\Delta k)|^2 \, d(\Delta k) = \frac{2\pi}{l_c} \tag{3.48}$$

is distributed amongst all the Fourier components. The fraction of grating energy that is spent towards simultaneous phase matching is

$$\frac{1}{2\pi/l_c}\left[\int_{\Delta k_a-\epsilon/2}^{\Delta k_a+\epsilon/2} |G(\Delta k)|^2 \, d(\Delta k) + \int_{\Delta k_b-\epsilon/2}^{\Delta k_b+\epsilon/2} |G(\Delta k)|^2 \, d(\Delta k)\right], \tag{3.49}$$

where ϵ is the width of the Fourier peaks in Δk domain. This quantity should be made as large as possible to maximize the effective nonlinear coefficients. The phase matching bandwidth ϵ is equal to the natural phase matching bandwidth $4\pi/l_c$ regardless of the specific grating function as long as the longest domain length in the crystal is much shorter than l_c, a condition that is always satisfied. Therefore, maximizing $|G(\Delta k_a)|^2 + |G(\Delta k_b)|^2$ achieves the same result as maximizing Equation (3.49). Since the ratio d_{eb}/d_{ea} is fixed ahead of time, then maximizing either Fourier component peak assures that the total energy in the "wasted" components is minimized.

For a given pair of arbitrary phase-mismatch terms Δk_a and Δk_b, the problem of simultaneous phase matching becomes finding a grating modulation function $g(z)$ so that:

- $g(z)$ can only assume values of $+1$ and -1,
- $|G(\Delta k)|$ has peaks at $\Delta k = \Delta k_a$ and $\Delta k = \Delta k_b$,

- the ratio $|G(\Delta k_b)/G(\Delta k_a)|$ is equal to a predetermined constant α which is proportional to β in Equation (2.72),
- $|G(\Delta k_a)|^2$ (or $|G(\Delta k_b)|^2$) is as large as possible.

3.5 Aperiodic Grating Design Method

In this section, we describe a simple *ad hoc* method for designing an aperiodic grating function $g(z)$ for the simultaneous phase matching of two arbitrary second-order nonlinear processes [8]. Our method is numerical and iterative; we make a guess at the grating function $g(z)$, calculate its Fourier components $G(\Delta k_a)$ and $G(\Delta k_b)$, determine how well the design requirements are satisfied, and modify our initial guess. Various technical restrictions (such as the minimum domain length) are also imposed on $g(z)$ at each iteration.

For a given pair of Δk_a and Δk_b values, we start out with a continuous-valued function

$$f(z) = \cos(\Delta k_a z) + A\cos(\Delta k_b z + \phi) \tag{3.50}$$

that is composed of the sum of two harmonic functions at Δk_a and Δk_b with amplitudes unity and A, respectively, and a phase difference ϕ. At the first iteration, we set the ratio of the two amplitudes to the targeted effective nonlinear coefficient ratio; i.e., $A = \alpha$. We also set the phase difference ϕ to zero. For this $f(z)$, we calculate $g(z)$ as

$$g(z) = \mathrm{sgn}[f(z)], \tag{3.51}$$

where sgn represents the signum function. In other words, we calculate the roots of $f(z)$ and set these to be the locations of the domain walls along the direction of propagation.

The grating mask used in the fabrication of the poled crystal is specified with a certain spatial resolution. This resolution is 0.05 μm in the fabrication process that we used. Therefore, at this stage we round off the domain wall locations to the nearest 0.05 μm increment. In addition, domain walls that form after electric field poling are guaranteed to be uniform only if the separation between two domain walls is larger than a certain distance called the minimum domain length, d_{min}. This distance is typically

a few micrometers. We tried to be conservative and took this distance to be 5 μm. In general $g(z)$ may come out to have a number of domains whose lengths are shorter than this distance. At this stage we simply discard such domains. In other words, the sign of any domain whose length is less than 5 μm is flipped, thereby transforming this and the two adjacent domains into a single domain. This is done at each iteration by sequentially flipping the sign of the shortest domain whose length is less than 5 μm until there are no domains left shorter than this critical length. This elimination method assures that the critical length restriction effects the grating minimally.

The resulting $g(z)$ becomes our first guess at a grating function. We then calculate the Fourier transform $G(\Delta k)$. The magnitude of the Fourier transform naturally has peaks located at $\Delta k = \Delta k_a$ and $\Delta k = \Delta k_b$, in addition to various other components located elsewhere. We calculate the magnitudes of these peaks $|G(\Delta k_a)|$ and $|G(\Delta k_b)|$, compare the ratio $|G(\Delta k_b)/G(\Delta k_a)|$ to α, and modify the value of A accordingly for the next iteration in small steps. This iterative method converges to a final $g(z)$ with the desired properties.

This procedure results in an aperiodic grating function $g(z)$ that has relatively high peaks at Δk_a and Δk_b, no domain lengths smaller than the critical fabrication length, and the desired ratio for the effective nonlinear coefficients. The only question that remains uncertain is whether the resulting effective nonlinear coefficients are as large as possible or not, i.e., whether $|G(\Delta k_a)|$ is maximized under the current constraints or not. We are not aware of any rigorous method that can answer this question. However, we maintain that as long as the effective nonlinear coefficients are "high enough," whether the grating function at hand is optimum or not is a mute point from a practical point of view. We can get a feel for whether $|G(\Delta k_a)|$ is high enough or not by comparing its magnitude with $2/\pi$, the largest Fourier coefficient of a periodic grating with $D_c = 0.5$. Since there are two "useful" components, it makes more sense to compare $|G(\Delta k_a)|^2 + |G(\Delta k_b)|^2$ with $(2/\pi)^2$.

At this point, the minimum domain length $d_{\min}$ is an important design parameter. For a periodic grating, the minimum possible value of the period Λ is twice $d_{\min}$ because a period consist of a pair of inverted and non-inverted domains. Therefore, the maximum

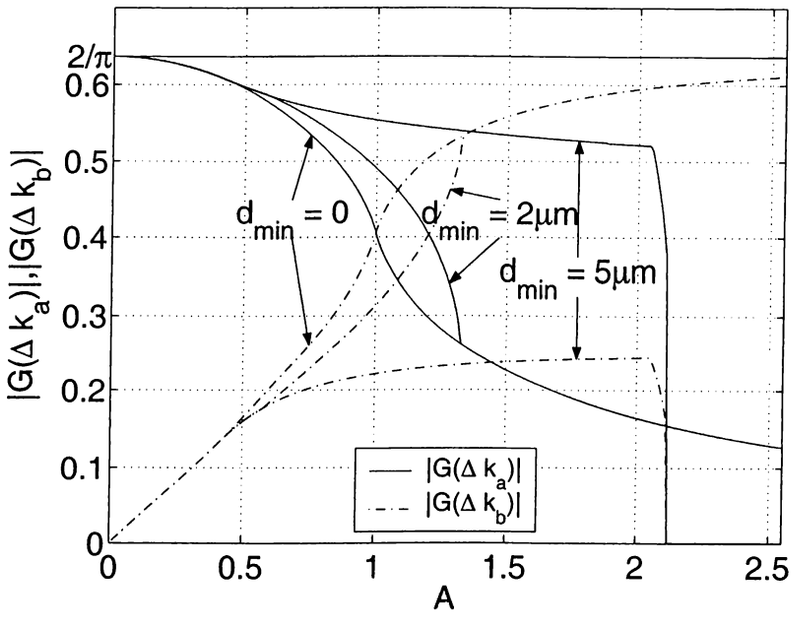

Figure 3.4: $|G(\Delta k_a)|$ and $|G(\Delta k_b)|$ for $d_{\min} = 0$, 2μm, and 5μm.

value of a phase mismatch Δk, that can be compensated with first order QPM, has a limit.

Similarly, the minimum domain length $d_{\min}$ restricts our design method. When Δk_a and Δk_b are both less than the maximum phase mismatch $\Delta k_{max} = \pi/d_{\min}$, it is possible to find a value of the parameter A that can satisfy any desired ratio of $|G(\Delta k_b)/G(\Delta k_a)|$. If the larger of Δk_a and Δk_b is close to Δk_{max} or exceeds this value, the grating design

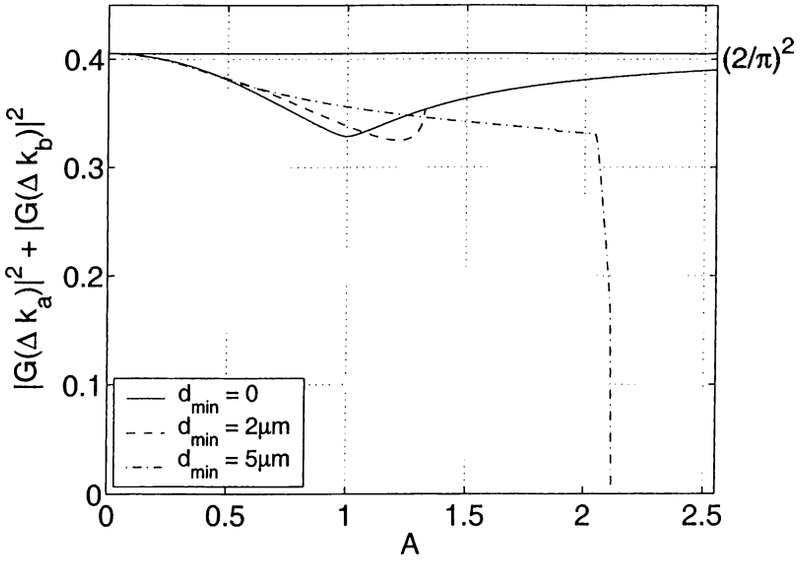

Figure 3.5: $|G(\Delta k_a)|^2 + |G(\Delta k_b)|^2$ for $d_{\min} = 0$, 2μm, and 5μm.

fails for some values of A. When both Δk_a and Δk_b exceed Δk_{max}, desired peaks at the phase mismatches Δk_a and Δk_b disappear completely. Figure 3.4 shows $|G(\Delta k_a)|$ and $|G(\Delta k_b)|$ as a function of A with $\Delta k_a = 3.06663 \times 10^5$ m^{-1} and $\Delta k_b = 7.671 \times 10^5$ m^{-1} for $d_{\min} = 0$, 2μm, and 5μm. These Δk_a and Δk_b values are taken from our experiments. For $d_{\min} = 5\mu$m, Δk_b exceeds the maximum frequency and the grating design fails for $A > 2.1$. For $d_{\min} = 2\mu$m, both Δk_a and Δk_b are smaller than the maximum frequency. Although the curve associated with $d_{\min} = 2\mu$m has different values for some range, it follows the curve with no restriction ($d_{\min} = 0$) for limiting values of $A = 0$ and $A \to \infty$. In this figure, we provide a flat line with a value of $2/\pi$ for the comparison purposes of the Fourier component magnitudes. Figure 3.5 shows $|G(\Delta k_a)|^2 + |G(\Delta k_b)|^2$ as a function of A. A flat line with a value $(2/\pi)^2$ is also provided. When we compare the curve for $d_{\min} = 5\mu$m in the range $A < 2.1$ (a range that Fourier peaks exist) with the flat line, we deduce that our designs at least employ 82% of the power available to a first order QPM.

We also investigated the iteration process by using the phase difference ϕ as another freely adjustable parameter. We found that even though the value of ϕ changes the grating function and does influence both the individual magnitudes and the ratio of the two Fourier components, its effects are usually within a few percent, as long as the crystal length is much larger than the average domain size. For the sake of simplicity, we set $\phi = 0$ at the beginning and do not modify this value.

In this chapter, we reviewed BPM and QPM methods. In the QPM method, an arbitrary interaction can be phase-matched with periodic grating structure. Both BPM and QPM allow room for simultaneously-phase-matched interactions, but they are limited in number. A general method for simultaneous phase matching of two arbitrary interactions needs aperiodic grating structures. Our design method provides such grating structures. In our method, we take into account the physical fabrication restrictions such as the minimum structure length.

Chapter 4

Overview of Experimental Work

This chapter provides an overview of the wavelength conversion experiments that we performed. In this thesis, we designed SD-OPOs and a SF-OPO based on KTP, KTA, PP-KTP, BBO, and APLN crystals pumped with cw and femtosecond mode-locked pulsed lasers. Here, we describe the operation principles of our OPOs, and provide information on the equipment and measurement techniques that we used throughout our experiments. Also, details of the nonlinear crystals that we used in our OPOs are given.

4.1 Optical Parametric Oscillators

In our experiments, we designed singly-resonant femtosecond-pulsed and cw OPOs. In this Section, we outline the operation principles of these OPOs.

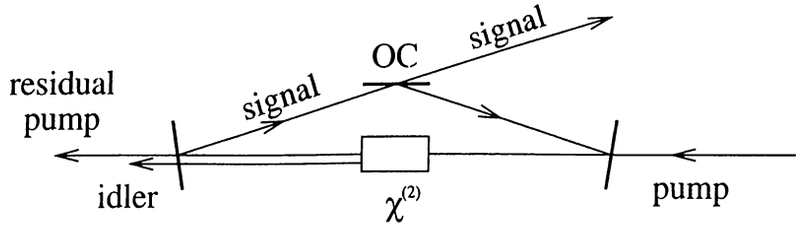

Figure 4.1: Schematic of an OPO.

4.1.1 Continuous-wave Optical Parametric Oscillators

The operational principles of cw OPOs follow the principles of optical parametric oscillation explained with plane wave solutions of the coupled-mode equations in Section 2.4.4. Figure 4.1 shows a schematic of a simple singly-resonant OPO. The signal field resonates inside a ring cavity formed by three mirrors. The output is obtained from a partially transmitting mirror called an output coupler (OC). All of the mirrors except the output coupler are high reflectors at the frequency of signal field. The pump beam, which provides the energy to the OPO, enters the cavity from one of the mirrors. This mirror also has special coatings making it transparent to the pump wavelength for better coupling into the cavity. Next the pump beam passes through the nonlinear crystal, providing parametric gain, and the remaining (residual) pump leaves the cavity from another mirror. There is also an idler beam that is generated in optical parametric amplification. All mirrors are also transparent to the idler beam, so that singly-resonant operation of the OPO is guaranteed.

A simple model of an OPO is shown in Figure 4.2. The parametric amplifier is modeled as a gain medium where the gain saturates with the increasing signal input as described by Equation (2.58) in Section 2.4.4. The output coupler has less than unity reflectance R_{OC}. This nonzero transmittance provides the output beam of the OPO. Unavoidable losses such as less than unity reflectance of highly reflecting mirrors, losses in the nonlinear material, and diffraction losses, can be taken into account as a single source of loss which is represented by a lumped reflectance R_{L}. Therefore, the total cavity round-trip loss is defined to be

$$\sigma_T = 1 - R_{\mathrm{L}} R_{\mathrm{OC}}. \tag{4.1}$$

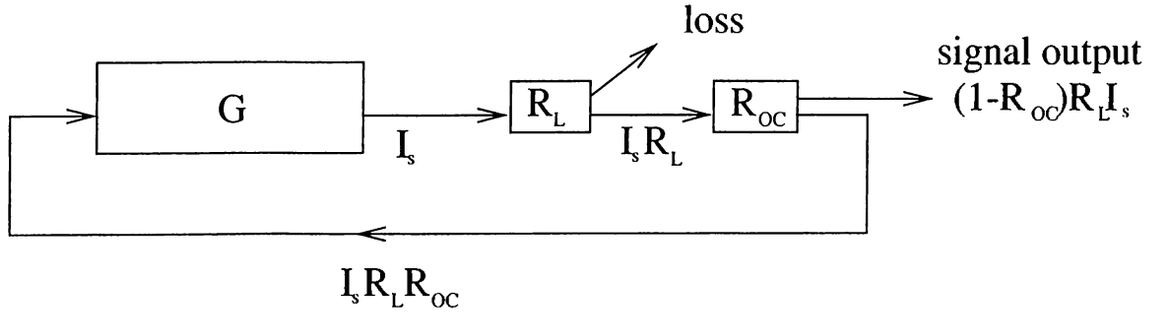

Figure 4.2: A model of an OPO. The signal intensity I_s is resonating inside the OPO.

A cavity equation corresponding to steady-state operation for a cw OPO can be written by equating the total round trip loss to the parametric gain

$$G = \frac{1}{1 - \sigma_T}, \tag{4.2}$$

where G is the saturated parametric gain. An important consequence of this equation together with the maximum value of gain [the unsaturated gain G_0 in Equation (2.61)] is that the OPO has a threshold value of nonlinear drive D_T provided by a pump beam intensity, and this value is determined by

$$G_0(D_T) = \frac{1}{1 - \sigma_T}. \tag{4.3}$$

When the unsaturated gain is less than the total cavity loss, there is no solution for Equation (4.2). When the input pump intensity is increased at this point, the unsaturated gain also increases. At a point where the unsaturated gain is equal to the total cavity loss, Equation (4.2) has a solution with zero signal intensity. After that point, as we further increase the pump intensity, oscillation starts and the signal intensity increases to a value such that the saturated gain is equal to the loss of the cavity at steady-state. Therefore, Equation (4.2) is used to determine the steady-state signal field intensity of the cw OPO above threshold.

The signal output of the OPO is provided by the output-coupler. Similarly, there is a non-resonant idler output in addition to the signal output. Therefore, the conversion efficiency of the OPO is defined as the ratio of the output power to the input pump power

$$\eta = \frac{P_{out}}{P_{pump}} \tag{4.4}$$

for each output. However, it may be more meaningful to define photon conversion efficiency

$$\frac{P_{out} \times \lambda_{out}}{P_{pump} \times \lambda_{pump}}, \tag{4.5}$$

because for each converted pump photon in parametric amplification, a signal and an idler photon are created.

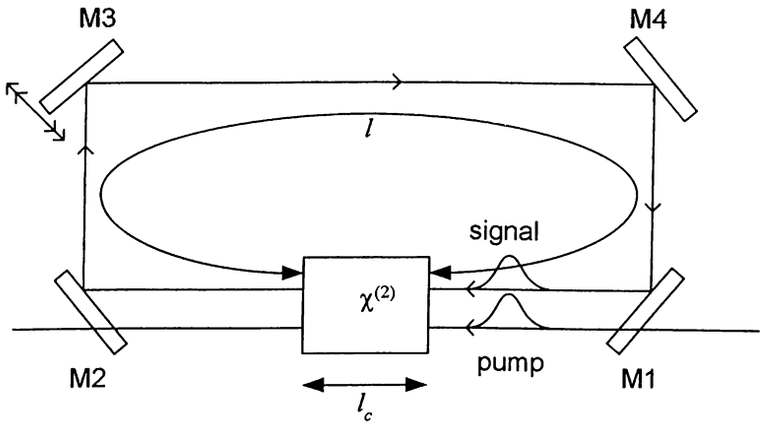

Figure 4.3: Synchronous pumping.

4.1.2 Femtosecond Optical Parametric Oscillators

In contrast to cw OPOs, our femtosecond OPOs operate with a train of pulses. A femtosecond mode-locked laser provides these pulses at a constant repetition rate. The operation scheme of femtosecond OPOs is called synchronous-pumping. In this scheme, the cavity length of the OPO is adjusted by moving one of the cavity mirrors such that in each round-trip, a signal pulse in the OPO cavity meets the incoming pump pulse in the nonlinear crystal (see Figure 4.3) and gets amplified. Figure 4.3 also shows a schematic of our femtosecond OPOs in the form of a four-mirror ring cavity. The pump pulses enter the cavity through M1 and pass through the nonlinear material and contribute to parametric amplification. Synchronization of the signal pulse resonating inside the cavity with the pump pulses is adjusted by moving M3. As the signal pulse grows with the energy provided by the pump pulses, it saturates the gain of the parametric amplifier and reaches a steady level where the energy just compensates for the losses of the signal pulse in the cavity. Therefore, operation of our femtosecond OPOs are similar to the cw OPOs as long as synchronization is maintained. The signal pulses are produced at a repetition rate which is equal to the repetition rate of the femtosecond pump laser.

The round-trip travel time of the signal pulse in the OPO cavity determines the repetition rate. The relation between the repetition rate r of the femtosecond laser and the round-trip travel time of a signal pulse in the OPO cavity is

$$\frac{1}{r} = \frac{l}{c} + \frac{l_c}{v_{gs}(\omega_s)}, \tag{4.6}$$

where l is the cavity round-trip length outside the nonlinear crystal, l_c is the nonlinear crystal length, ω_s is the signal frequency, and $v_{gs}(\omega_s)$ is the group velocity inside the nonlinear crystal. This travel time depends on the frequency of the signal pulse because, except for the distance l in air between the mirrors, the signal pulse travels through the nonlinear material with a frequency-dependent group velocity $v_{gs}(\omega_s)$. As a result, an important point about synchronous-pumping is that a change in the physical round-trip cavity length results in a change in the signal frequency ω_s within the gain bandwidth of the optical parametric amplifier. This can be used to tune the OPO within the OPO gain bandwidth [28], [69].

The group velocities of the pump, signal, and idler pulses are all different. This concept is known as GVM. The amount of GVM between two pulses is defined as the amount of pulse separation in time for a unit length of travel, and given by

$$\mathrm{gvm}_{mn} = \frac{l}{v_{gm}(\omega_m)} - \frac{1}{v_{gn}(\omega_n)}. \tag{4.7}$$

When GVM is high, the interaction length is limited by the overlap of the pump, signal, and idler pulses, since the pulses walk away from each other as they travel inside the nonlinear crystal. As a result, GVM between the pump, signal, and idler pulses may limit the interaction length, hence the strength of nonlinear interaction for longer crystals.

4.1.3 SHG and SFG with Optical Parametric Oscillation

In our experiments, we employ simultaneous phase matching of optical parametric oscillation together with SHG of the signal wave or SFG between the pump and the signal waves. As a result, the operation of our OPOs are different from the operation of simple OPOs. In our experiments, we try to generate efficient second-harmonic or sum-frequency. Therefore, we replace the output-coupler mirror of the normal OPO with another high reflector mirror to obtain high signal intensity levels inside the OPO cavity. Our OPO cavities are under-coupled cavities for the signal, but power output is provided with SHG or SFG through transparent mirrors for the second-harmonic or sum-frequency beams. As a result, the SHG or SFG processes provide nonlinear output-coupling. This nonlinear power coupling may provide efficient conversion. The conversion efficiency is

the ratio of the output power to the input pump power as defined in Equation (4.4), but the photon conversion efficiency

$$\frac{P_{out} \times \lambda_{out}}{P_{pump} \times \lambda_{pump}} \times 2 \tag{4.8}$$

is different from Equation (4.5), because two pump photons are converted to generate a second-harmonic or a sum-frequency photon. Our SD-OPO and SF-OPO models are different from a regular OPO. In our OPOs, the resonant signal field experiences a nonlinear loss mechanism in addition to the linear cavity losses. In our SD-OPOs, we have one additional source of linear loss, a polarization rotation device. The loss caused by this device depends on the rotation angle φ as $1 - \cos^2(\varphi)$.

4.2 Simultaneous Phase Matching

In this section, we present information on the nonlinear crystals that we used in our experiments, and explain how we achieved simultaneous phase matching.

4.2.1 Simultaneous Phase Matching with $KTiOPO_4$

In the SD-OPO and the SF-OPO experiments in Sections 5.1 and 5.3, 1 mm and 5 mm long, bulk KTP crystals were used. These custom-made crystals were provided by Cleveland Crystals with dimensions, cut angles, and coatings specified by us. These are

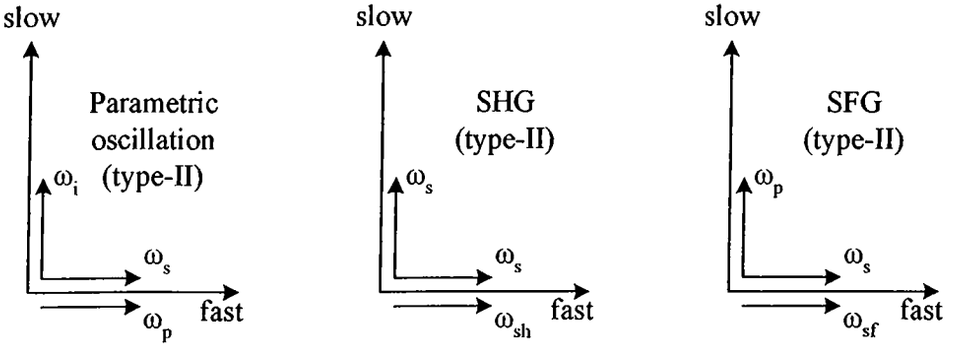

Figure 4.4: Phase matching configurations of the pump (p), the signal (s), and the idler (i) for parametric oscillation, the signal and the second-harmonic (sh) for SHG and the pump the signal, and the sum-frequency (sf) for SHG and SFG.

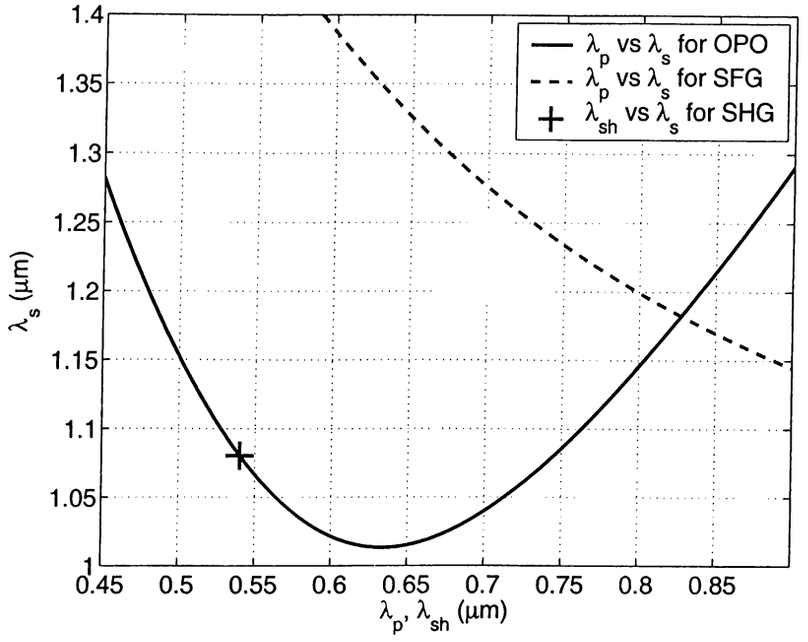

Figure 4.5: The phase matching curves of the pump (p) versus signal (s) for OPO, the pump versus signal for SFG and the second-harmonic (sh) versus signal for SHG.

all cut at $\theta = 90°$ and $\phi = 0°$ for collinear phase matching (coordinate system definition in IEEE/ANSI standard: $x = Y$, $y = -X$, $z = Z$). We use type-II phase matching for optical parametric oscillation and simultaneous SHG or SFG in which the fast-axis and the slow-axis coincide with y and z directions, respectively (see Figure 4.4). As a result, we utilize the nonlinear coefficient $\overleftrightarrow{\chi}^{(2)}_{XXZ} = 7.2$ pm/V (for SHG at 1064 nm) as specified in [80]. Approximate values of the nonlinear coefficient for nonlinear interactions other than SHG at 1064 nm is calculated using Miller's Rule factor (see Appendix A). The Sellmeier equations for the KTP crystals [90] used to calculate the phase matching curves are

$$n_x^2 = 3.0065 + \frac{0.03901}{\lambda^2 - 0.04251} - 0.01327\lambda^2, \tag{4.9}$$

$$n_y^2 = 3.0333 + \frac{0.04154}{\lambda^2 - 0.04547} - 0.01408\lambda^2, \tag{4.10}$$

$$n_z^2 = 3.3134 + \frac{0.05694}{\lambda^2 - 0.05658} - 0.01682\lambda^2, \tag{4.11}$$

where λ is the wavelength.

In the SD-OPO and the SF-OPO experiments in Sections 5.1 and 5.3, the signal and the pump waves are both p-polarized, (horizontal, fast axis), and the idler is s-polarized (vertical, slow axis). In the SF-OPO, the pump and the signal wavelengths

are common for parametric oscillation and SFG. The sum-frequency and the signal are both p-polarized and the pump is s-polarized in SFG. In the SD-OPO, only the signal wavelength is common for parametric oscillation, and SHG. The signal has both s and p-polarized components, and the second-harmonic is p-polarized. Figures 4.5 shows the phase matching curves (see Section 3.3) of all the interactions (note that the SHG phase matching curve is actually a single point). To find the simultaneously-phase-matched operation points for the SF-OPO at $\theta = 90°$ and $\phi = 0°$, we checked the intersection points of optical parametric oscillation and SFG phase matching curves as described in Section 3.4.1. The signal and the pump wavelengths corresponding to the intersection point in Figure 4.5 are 1182.4 nm and 827.4 nm, respectively. The single SHG point marked by + for the second-harmonic versus the signal curve in the figure determines the signal wavelength of 1080.4 nm for SD-OPO. As a result, the pump wavelength is 744.8 nm for the simultaneously-phase-matched operation of the SD-OPO.

4.2.2 Simultaneous Phase Matching with $KTiOAsO_4$

In the femtosecond and cw experiments in Section 5.2 and 6.2, a 20 mm long bulk KTA crystals was used. This custom-made crystal was provided by Crystal Associates with dimensions, cut angles, and coatings specified by us. It is cut at $\theta = 90°$ and $\phi = 0°$ for collinear phase matching (coordinate system definition in IEEE/ANSI standard: $x = Y$, $y = -X$, $z = Z$). We use type-II phase matching for optical parametric oscillation and simultaneous SHG in which the fast-axis and the slow-axis coincide with y and z

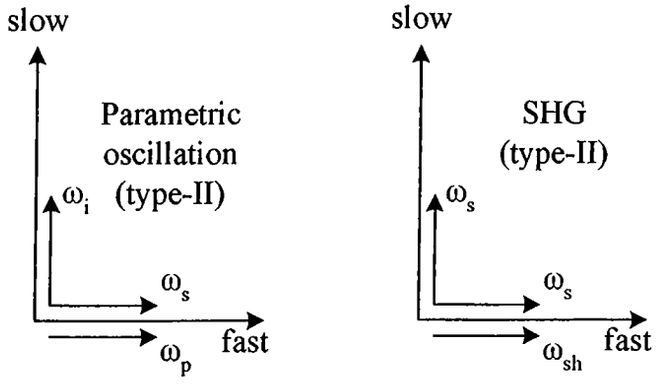

Figure 4.6: Phase matching configurations of the pump (p), the signal (s) and the idler (i) for parametric oscillation, the signal and the second-harmonic (sh) for SHG.

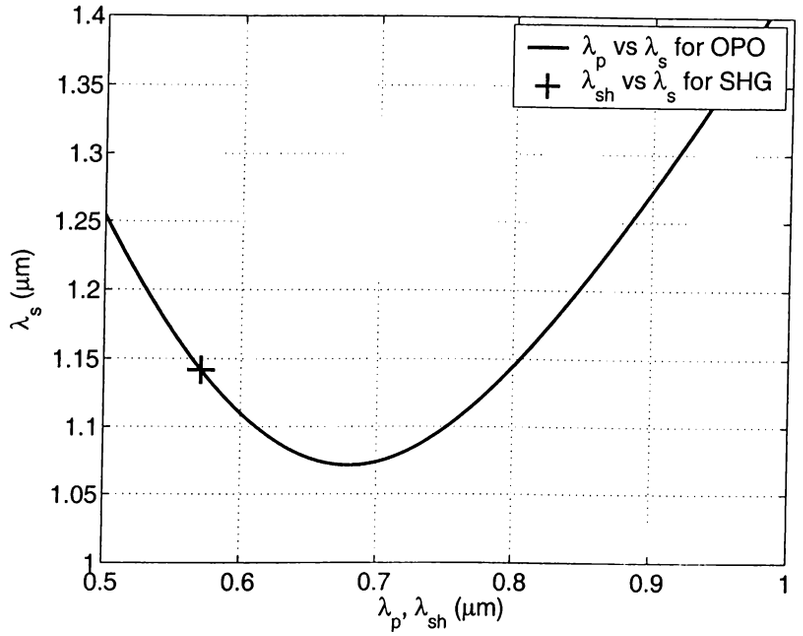

Figure 4.7: The phase matching curves of the pump (p) versus the signal (s) and the second-harmonic (sh) versus the signal for KTA.

directions, respectively (see Figure 4.6). As a result, we utilize the nonlinear coefficient $\overleftrightarrow{\chi}^{(2)}_{XXZ} = 10.4$ pm/V (for SHG with 1064 nm) as specified in [80]. The Sellmeier equations for the KTA crystal [91] used to calculate the phase matching curves are

$$n_x^2 = 2.1495 + \frac{1.0203\lambda^{1.9951}}{\lambda^{1.9951} - 0.042378} + \frac{0.5531\lambda^{1.9567}}{\lambda^{1.9567} - 72.3045}, \tag{4.12}$$

$$n_y^2 = 2.1308 + \frac{1.0564\lambda^{2.0017}}{\lambda^{2.0017} - 0.042523} + \frac{0.6927\lambda^{1.7261}}{\lambda^{1.7261} - 54.8505}, \tag{4.13}$$

$$n_z^2 = 2.1931 + \frac{1.2382\lambda^{1.8920}}{\lambda^{1.8920} - 0.059171} + \frac{0.5088\lambda^2}{\lambda^2 - 53.2898}. \tag{4.14}$$

In these SD-OPO experiments in Sections 5.2 and 6.2, the signal and the pump waves are both p-polarized, (horizontal, fast axis), and the idler is s-polarized (vertical, slow axis) in OPO. In the SD-OPO, only the signal wavelength is common for parametric oscillation and SHG. The signal has both s and p-polarized components and the second-harmonic is p-polarized, similar to the SD-OPO based on the KTP crystal. Figures 4.7 shows the phase matching curves (see Section 3.3) of both interactions (note that the SHG phase matching curve is actually a single point). The single SHG point marked by + for the second-harmonic versus the signal curve in the figure determines the signal wavelength of 1141.8 nm for SD-OPO. As a result, the pump wavelength is 797.6 nm for the simultaneously-phase-matched operation of the SD-OPO.

4.2.3 Periodically-Poled $KTiOPO_4$ Crystal

In the intracavity-doubled OPO experiment in Section 5.4, a z-cut 1 mm thick and 8 mm long hydrothermally grown KTP crystal is used for parametric amplification. This crystal was manufactured and provided by William P. Risk [92] without any coatings. The pump, signal, and idler beams are polarized along the z-axis of the PP-KTP crystal to utilize the large nonlinear coefficient $\overleftrightarrow{\chi}^{(2)}_{ZZZ} = 33.4\text{pm/V}$ of KTP [89]. The Sellmeier equations for the KTP crystal [89] used to calculate phase matching curves are

$$n_x^2 = 2.1146 + \frac{0.89188\lambda^2}{\lambda^2 - 4.35181321 \times 10^{-2}} - 0.01320\lambda^2, \tag{4.15}$$

$$n_y^2 = 2.1518 + \frac{0.87862\lambda^2}{\lambda^2 - 4.75283601 \times 10^{-2}} - 0.01327\lambda^2, \tag{4.16}$$

$$n_z^2 = 2.3136 + \frac{1.00012\lambda^2}{\lambda^2 - 5.67916561 \times 10^{-2}} - 0.01679\lambda^2. \tag{4.17}$$

4.2.4 β–Ba_2BO_4 Crystal

A 5 mm long BBO that is cut for type-I phase matching along the $\theta = 20.8°$ and $\phi = 90°$ direction is used for SHG in the intracavity-doubled OPO experiment for SHG in Section 5.4 (coordinate system definition in IEEE/ANSI standard: $x = X$, $y = Y$, $z = Z$). This custom-made crystal was provided by Cleveland Crystals with dimensions, cut angles, and coatings specified by us. The angular dependence of the effective nonlinear coefficient is

$$d_{\text{eff}} = \frac{1}{2}\left[\overleftrightarrow{\chi}^{(2)}_{ZXX}\sin(\theta) + \overleftrightarrow{\chi}^{(2)}_{YXX}\cos(\theta)\sin(3\phi)\right], \tag{4.18}$$

where $\overleftrightarrow{\chi}^{(2)}_{ZXX} = 0.2$ pm/V and $\overleftrightarrow{\chi}^{(2)}_{YXX} = -4.6$ pm/V [89]. The Sellmeier equations for the KTP crystal [89] used to calculate phase matching curves are

$$n_x^2 = 2.3753 + \frac{0.01224}{\lambda^2 - 0.01667} - 0.01516\lambda^2, \tag{4.19}$$

$$n_z^2 = n_y^2 = 2.7359 + \frac{0.01878}{\lambda^2 - 0.01822} - 0.01354\lambda^2. \tag{4.20}$$

4.2.5 Aperiodically-Poled $LiNbO_3$ Crystal Design

Using our method described in Section 3.5, we designed gratings for a SD-OPO that is based on an aperiodically-poled $LiNbO_3$ (APLN) crystal, with the aim of converting the output of a laser at 790 nm to the visible at 570 nm. Given these pump and second-harmonic wavelengths, the signal and idler wavelengths come out to be 1140 nm and 2573 nm, respectively. We designed four different gratings with prescribed β values of 0.39, 0.50, 0.61, and 0.72. These β values were chosen based on our estimate of the nonlinear drive we would achieve in our setup. The 20 mm-long $LiNbO_3$ crystal was x-cut, and all beams were taken to be polarized along the z-axis of the crystal in order to utilize the highest nonlinear coefficient ($\overleftrightarrow{\chi}^{(2)}_{zzz} = -54$ pm/V for SHG with 1064 nm as specified in [80]). This custom-made crystal was provided by Deltronics Crystals with the lithographic mask design, dimensions, cut angles, and coatings specified by us. Lithographic restrictions limited the poled length of the crystal to 18 mm. The aperture size for each grating is 0.47 $\times$ 0.5 mm, with 0.5 mm being the crystal thickness. The

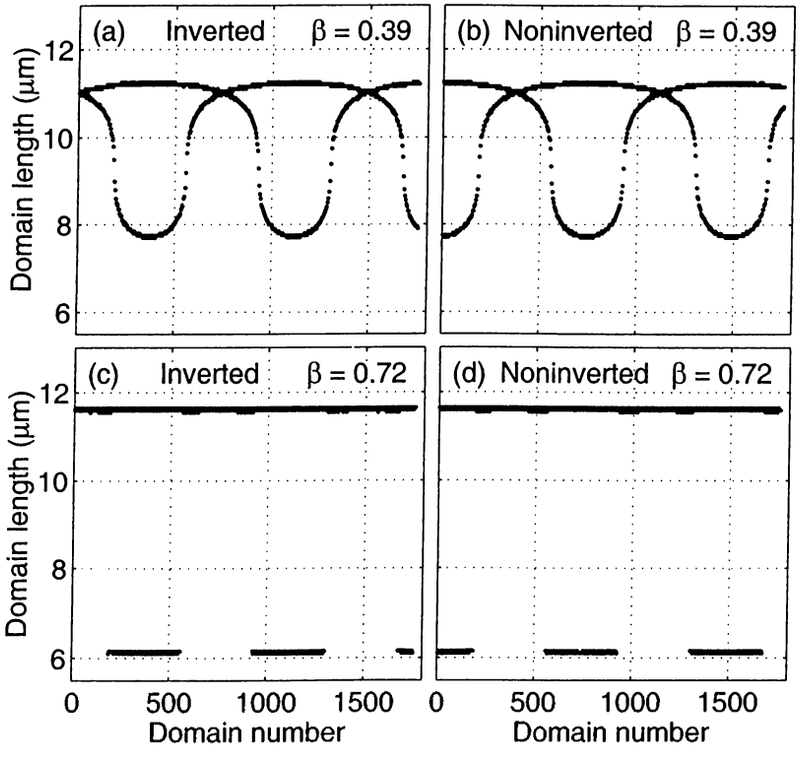

Figure 4.8: Lengths of (a) inverted and (b) noninverted domains of the first grating (β = 0.39), and (c) inverted and (d) noninverted domains of the second grating (β = 0.72), as functions of domain number.

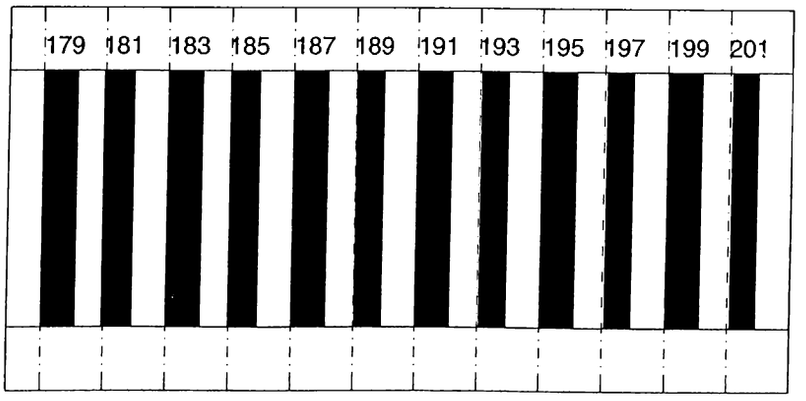

Figure 4.9: Expanded diagram illustrating a segment of the first grating ($\beta = 0.39$). Black (white) stripes represent inverted (noninverted) domains. The grid lines are equally spaced.

temperature-dependent Sellmeier equations given in [93] were used for calculating the refractive indices. The crystal temperature was chosen to be 130 °C in order to avoid photorefractive damage. The phase-mismatch terms for the OPO and SHG processes at the chosen wavelengths were $\Delta k_a = 3.06663 \times 10^5$ m^{-1} and $\Delta k_b = 7.67070 \times 10^5$ m^{-1}, respectively. The target α values for our two gratings came out to be 0.203, 0.260,

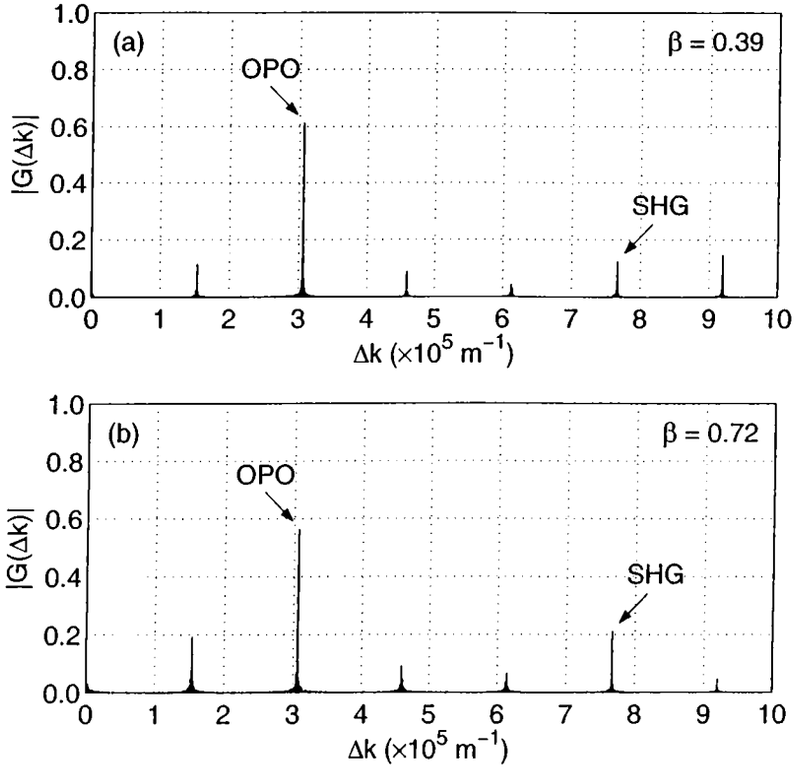

Figure 4.10: Magnitude of the normalized Fourier transform $|G(\Delta k)|$ for the (a) first ($\beta = 0.39$) and (b) second ($\beta = 0.72$) gratings.

0.317, and 0.375, and our method converged to $A = 0.385$, $A = 0.486$, $A = 0.622$, and $A = 0.847$, for the $\beta = 0.39$, $\beta = 0.50$, $\beta = 0.61$ and $\beta = 0.72$ gratings, respectively.

For the gratings with $\beta = 0.39$ and $\beta = 0.72$, the fractional error in achieving the prescribed β values was within 2×10^{-5}, much smaller than what is necessary to influence the resulting conversion efficiency appreciably. When we calculated β using Equation (2.72), we took the dispersion in the nonlinear coefficients into account by employing Miller's rule [80].

There are 1756 domains in each grating. The smallest domain length is 7.7 μm (6.1 μm) whereas the largest domain length is 15.2 μm (14.8 μm) for the first (second) grating. The average domain length for both gratings is 10.3 μm. Figure 4.8 shows the length of the inverted and noninverted domains for the two gratings. Figure 4.9 is an expanded diagram illustrating domains with domain numbers in the 178—202 range for the first grating ($\beta = 0.39$). The aperiodic nature of the grating function is evident.

Figure 4.10 shows the magnitude of the normalized Fourier transform ($|G(\Delta k)|$) of the grating modulation functions for the two grating structures. For the first grating ($\beta = 0.39$), the fractional errors in placing the first and second Fourier transform peaks at Δk_a and Δk_b ($\left|(\text{peak location})_{a,b} - \Delta k_{a,b}\right| / \Delta k_{a,b}$) are 2.9×10^{-6} and 3.1×10^{-6}, respectively; whereas for the second grating ($\beta = 0.72$), the corresponding fractional errors are 6.1×10^{-6} and 2.1×10^{-6}. For both gratings, these errors correspond to a shift on the order of 10^{-3} nm in the prescribed wavelengths of the pump, signal and second-harmonic beams.

When the newer temperature-dependent Sellmeier equations given in [94] are used, the phase-matched pump, signal and second-harmonic wavelengths with these gratings are off by 0.48 nm, 0.34 nm and 0.17 nm, respectively.

The total useful Fourier components $|G(\Delta k_a)|^2 + |G(\Delta k_b)|^2$ come out to be 0.39 ($\beta = 0.39$) and 0.36 ($\beta = 0.72$). Comparing these values with $(2/\pi)^2 = 0.41$, we note that the gratings designed using our method yield effective nonlinear coefficients that are almost as high as possible.

4.3 Experimental Devices

In this section, we present general information on the equipment used in our experiments.

4.3.1 Continuous-wave Argon-ion Laser

An argon-ion laser (Coherent, Innova 300) provides a 8 W pump beam to a femtosecond Ti:sapphire laser. The argon-ion laser operates in a multi-line configuration for visible wavelengths in the range 457.9–514.5 nm. In cw experiments, we also use this laser to pump our cw Ti:sapphire laser that is described in Section 6.1.

4.3.2 Femtosecond Laser Source

In the femtosecond experiments presented in Chapter 5, we use a mode-locked Ti:sapphire laser (Coherent, Mira-900F). This laser is tunable within a range between 700 and 1000 nm. It generates pulses with a repetition rate of 76 MHz corresponding to its longitudinal-mode separation. Its pulse widths can be adjusted in the range 100–180 fs.

4.3.3 Laser Optics

In the experiments, we used various custom made optics such as mirrors, lenses, polarizers, wave-retarders, and prisms. We determined their properties such as their dimensions, surface coating, surface curvature when we were designing an experiment. For example, our lenses have anti-reflection coatings for a range of wavelengths and our mirrors have coatings for reflection of various beam such as the signal beam of an OPO. Some mirrors called dichroic mirrors have two coating specifications, one for reflection and one for transmission. These are used to separate two beams at different wavelengths. We also specify the surface curvatures of the mirrors and the lenses to have a specific focal length. Polarizers and wave-retarders like lenses are transmissive components and have anti-reflection coatings. Wave-retarders are wavelength dependent devices and we also specify their operation wavelength. These optics are mostly provided from CVI

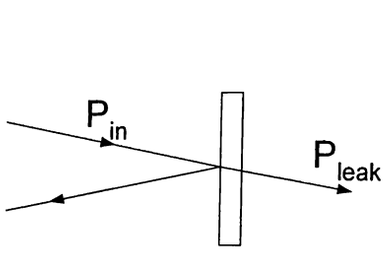

Figure 4.11: Mirror power calibration.

Laser Corp.

4.4 Measurement Techniques and Instruments

We performed power, pulse width, and spectral measurements on various beams in our experiments. We also observe shape of these beams with CCD camera.

Average power measurements were made using a Molectron Detector PowerMax 5100 Laser Power Meter and a Coherent Labmaster Ultima Power Meter. These calibrated power meters provide 10 mW to 10 W range readings. Low power measurements in the range of several 1 μW to 10 mW were made with a Newport Optical Power Meter model 840, which is a calibrated large area silicon photodetector, and other large area RCA photodiodes (type C30822) that we calibrate using calibrated power meters.

Intracavity power measurements also require calibration. The leakage power measurements at the back of high reflector mirrors are converted to the intracavity power measurements by using the measured ratio of the leakage power P_{leak} to the incident power P_{in} (see Figure 4.11).

Pulse width measurements are made using Femtochrome Research FR103 autocorrelator. This device provides intensity autocorrelations for a wavelength range between 430 nm and 1080 nm for pulses as short as 30 fs.

Spectral measurements are performed by CVI Laser Digikröm 110 1/8 Meter and CVI Laser Digikröm 240 1/4 Meter monochromators. The Digikröm 110 monochromator used in femtosecond experiments has two diffraction gratings with 600 lines/mm and 1200 lines/mm. With the diffraction grating of 1200 lines/mm and the minimum slit widths of 150 μm, it has 0.5 nm resolution. The Digikröm 240 monochromator also has

three diffraction gratings with 300 lines/mm, 600 lines/mm, and 1200 lines/mm. With the diffraction grating of 1200 lines/mm and the minimum slit widths of 20 μm, it has 0.01 nm resolution.

Beam profile observations are performed by Spiricon Laser Beam Analyzer Model LBA-100A. The beam analyzer provides numerical beam profile analysis. We used it with a COHU 6400 series CCD camera.

Chapter 5

Femtosecond Experiments

In this chapter, we present our experiments on femtosecond OPOs and simultaneous phase matching for frequency upconversion. In these experiments, we performed three SD-OPO experiments based on KTP, KTA, and APLN crystals. In addition, we performed a SF-OPO experiment based on a KTP crystal. In these experiments, we demonstrate class-A and class-C interactions of simultaneous phase matching.

Other than these experiments where we employ simultaneous phase matching, we performed an experiment of an intracavity-doubled OPO. In this device, a PP-KTP crystal provides parametric gain and a BBO crystal provides intracavity SHG of a signal wave.

5.1 Self-doubling KTP OPO

In this experiment, a 5 mm long KTP crystal that is cut for collinear phase matching ($\theta = 90°$, $\phi = 0°$) is used. As described in Section 4.2.1, we use type-II phase matching for both optical parametric oscillation and simultaneous SHG; the pump beam at 745 nm and the signal beam at 1080 nm are both p-polarized (horizontal, fast crystal axis), and the idler beam at 2400 nm is s-polarized (vertical, slow crystal axis), the fundamental beam at 1080 nm has both p-polarized and s-polarized components, and the second-harmonic beam at 540 nm is p-polarized. This polarization geometry belongs to class-C

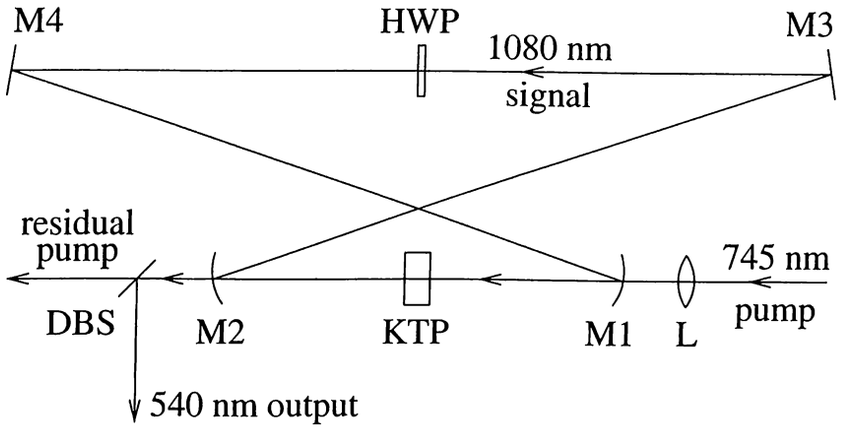

Figure 5.1: Self-doubling OPO setup. The pump beam is provided by a mode-locked Ti:Sapphire laser that has 150 fs long pulses.

SD-OPOs. The crystal has antireflection coatings for the signal wavelength (1080 nm) on both surfaces, the pump wavelength (745 nm) on the input surface, and the second-harmonic wavelength (540 nm) on the output surface.

Figure 5.1 shows the experimental setup. A mode-locked Ti:Sapphire laser (see Section 4.3.2) provides the pump beam to the OPO at a wavelength of 745 nm with a pulse width of 150 fs (225 fs autocorrelation). A ring cavity consisting of four mirrors M1, M2, M3 and M4 is constructed. All mirrors are high reflectors at 1080 nm. M1 and M2 are 100 mm radius of curvature concave, and M3 and M4 are flat. The KTP crystal is positioned at the intracavity focus between M1 and M2. The pump beam is focused into the crystal with a lens (L) of focal length 50 mm and enters the cavity through M1, which has high transmission coatings for this purpose. At this point, the pump beam experiences a total loss of 3% propagating through the lens and M1. The lowest order transverse mode of the cavity has a 30 μm diameter (calculated), and the focused pump beam has a 60 μm diameter (measured) at the crystal. A half-wave plate (HWP) at 1080 nm is placed inside the OPO cavity which is used to rotate polarization of the signal beam. Thus, we can couple some p-polarized signal beam to s-polarization which is necessary for type-II SHG. In order to achieve synchronous-pumping as described in Section 4.1.2, the length of the cavity is manually adjusted by moving M3. The frequency-doubled green beam at 540 nm exits the cavity through M2, which has high transmission coatings for this purpose. This optic is also transparent to the pump and the idler wavelength at 2400 nm. We use a dichroic beamsplitter (DBS) which separates

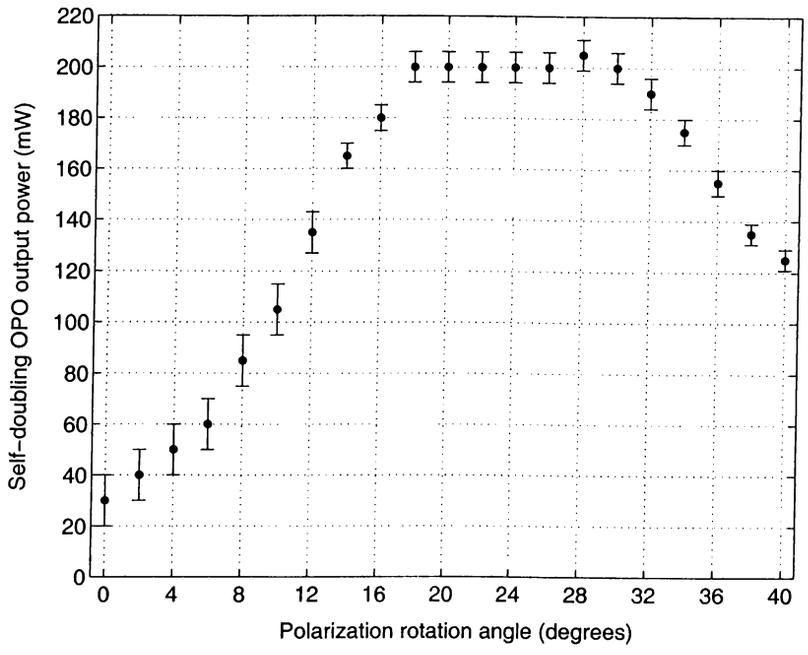

Figure 5.2: Self-doubling OPO output power at 540 nm as a function of a polarization rotation angle.

the output green beam from the residual pump beam and the generated idler beam. The diverging output beam is collimated with a lens (not shown). At this point, the green beam experiences a total loss of 9% propagating through M2, the collimating lens, and the DBS. In addition, intracavity signal power and polarization is observed using the relatively weak 1080 nm beam coming out through M3 (see Section 4.4).

When the fast and slow axis of the HWP are aligned with those of the crystal, there is no polarization rotation. Hence we observe little frequency doubling, only due to parasitic interactions. This results in a severely undercoupled OPO cavity for the signal beam. In this case, we measured the OPO threshold to be 25 mW before the lens. At an input pump power of 700 mW, the pump beam is depleted by 62%, showing strong parametric conversion and the signal output from M3 is 45 mW.

For simultaneously-phase-matched frequency doubling in the KTP crystal, a portion of the p-polarized signal beam must be coupled to s-polarization. This is achieved by a rotation of the intracavity signal polarization by rotating the HWP. This polarization rotation introduces a linear loss to the p-polarized signal beam which results in an increase in the OPO threshold. In addition, the p-polarized signal beam experiences a nonlinear loss due to SHG but this does not effect the OPO threshold, because, there

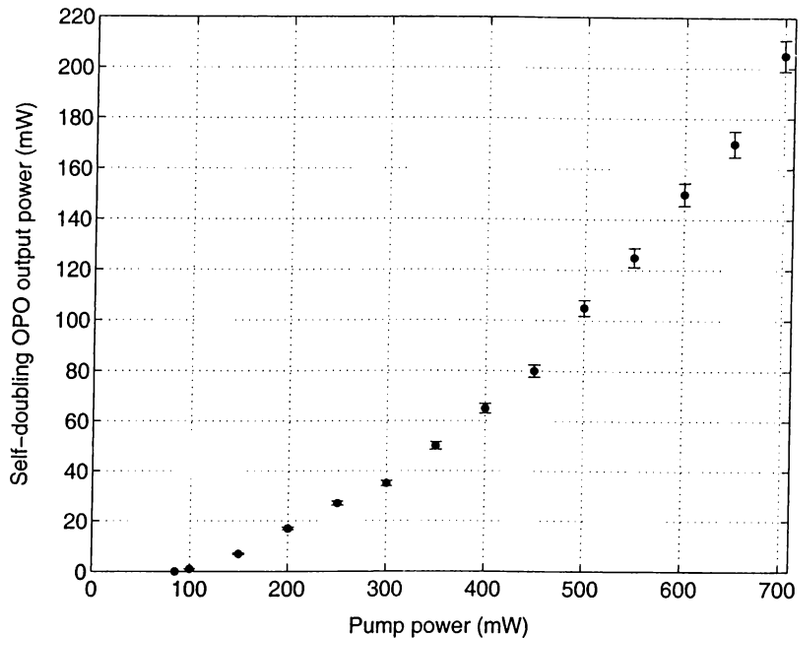

Figure 5.3: Self-doubling OPO output power at 540 nm as a function of input pump power while the polarization rotation angle is held fixed at 28°.

is very little signal power, and as a result very little SHG near threshold. Figure 5.2 shows the 540 nm green output power from the SD-OPO as a function of the polarization rotation angle of the intracavity signal for a pump power of 700 mW. A maximum of 205 mW green output power is obtained at a polarization rotation angle of 28°. At this point, the conversion efficiency of the input pump power to the output green power is 29%, and the pump depletion is 71%. The 1080 nm signal output from M3 drops to 11 mW at this point and the *s*-polarized component in the cavity is depleted by the SHG process at the output of the crystal. Since, two 745 nm photons are used up to create one 540 nm photon, the photon conversion efficiency [95] for the SD-OPO is given by the number of output 540 nm photons divided by twice the number of input 745 nm photons. (Full conversion yielding a photon conversion efficiency of 100%.) Our 29% power conversion efficiency corresponds to a photon conversion efficiency of 42%. When the extra losses sustained by the pump at the input (L and M1) and by the green at the output (M2, collimating lens, and DBS) are taken into account, we deduce a power conversion efficiency of 34% and a photon conversion efficiency of 48%. Figure 5.3 shows the green output power as a function of input pump power. The polarization rotation angle at each input pump power is not optimized to yield the maximum green output power but kept constant at 28°. The increased OPO threshold due to an additional

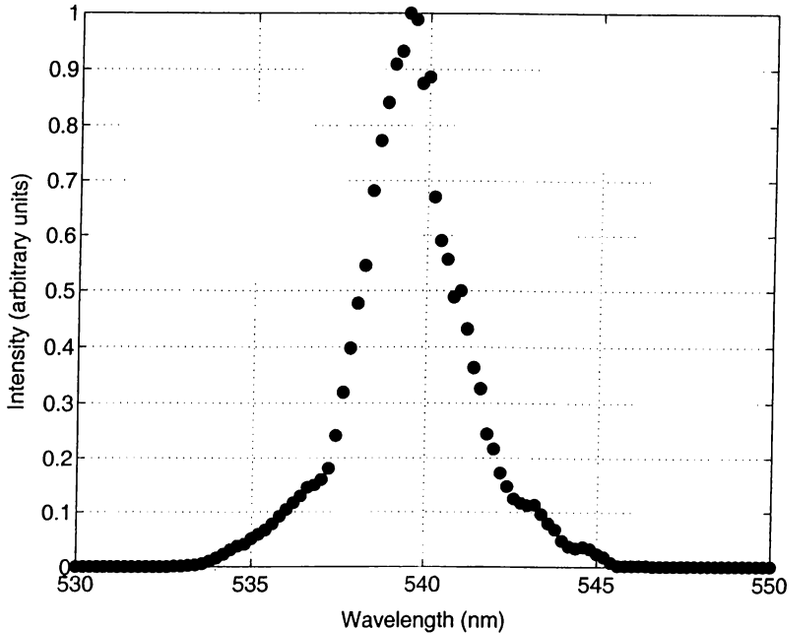

Figure 5.4: Spectrum of the self-doubling OPO output at 540 nm.

linear loss of HWP is measured to be 85 mW.

Figure 5.4 shows the spectrum of the green output beam as measured by a monochromator (CVI Laser Digikröm 110). The output spectrum is narrower than

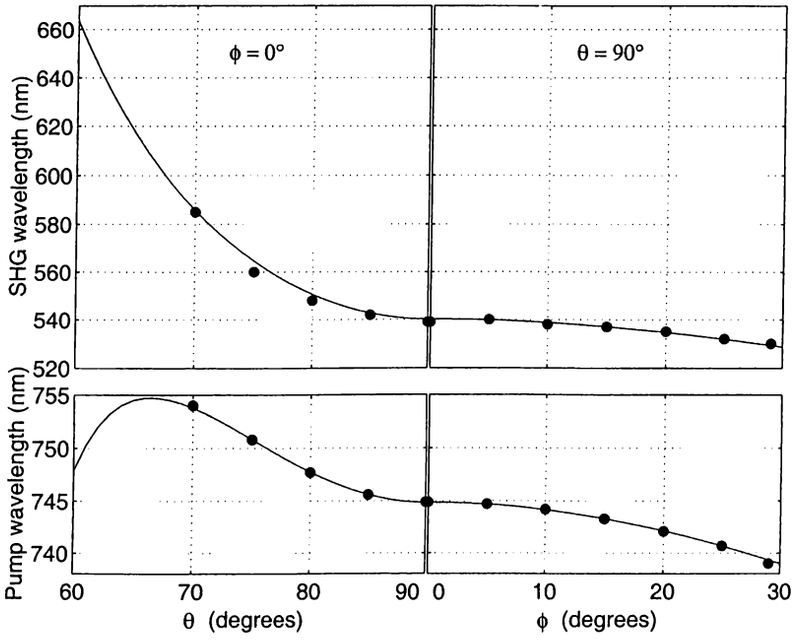

Figure 5.5: Calculated tuning curves for the self-doubling OPO. Angles are internal to the crystal. The circles represent experimental data points.

those of the pump and the intracavity signal. The autocorrelation width of the second-harmonic and the signal pulses are measured to be 480 fs and 415 fs, respectively. This pulse broadening in the second-harmonic pulse is due to GVM between the components of the signal and the second-harmonic pulses in the crystal [37]. It can be reduced by use of a shorter crystal. In addition, the use of intracavity dispersion compensation prisms may also be necessary to decrease pulse duration, because this compensation system prevents the signal pulse broadening due to group velocity dispersion (GVD) in the KTP crystal. The beam profile of the green OPO output is measured with a beam profiler to be nearly Gaussian.

It is possible to tune the SD-OPO output. Since, for a fixed propagation direction, there is a specific wavelength for simultaneous phase matching of parametric oscillation and SHG (see Section 3.4.1), we need to vary the wavelength of the pump beam in conjunction with the crystal angles to tune the SD-OPO. Figure 5.5 shows calculated tuning curves for the SD-OPO together with experimental data points. We demonstrated tunability in the 530 to 585 nm range. Although theoretical tuning curves allow us to achieve much higher tuning ranges, the tunability range in the experiment is limited due to reflection losses from the crystal surfaces at high incidence angles and mechanical constraints. The relatively long crystal poses a number of minor inconveniences in tuning. Rotating the crystal not only changes the optical cavity length, but also shifts the beams laterally. These effects are easily compensated for by translating M3 and slightly realigning M2. The size of the transverse cavity mode and hence its overlap with the pump is strongly influenced by the distance between M1 and M2, which also has to be readjusted after a rotation of the crystal. The use of a shorter crystal should decrease the sensitivity of the cavity to crystal rotation.

In this experiment, we observed damage on the KTP crystal. At high second-harmonic output powers (> 100 mW), we observe power drop 10% for an approximately 10 min of operation. This drop in second-harmonic power become fast near the maximum output power. Another consequence of this damage may be the flat-top shape of the second-harmonic power output graphic in Figure 5.2.

In summary, we have demonstrated a SD-OPO that employs a single nonlinear

crystal for both parametric oscillation and SHG. The two step conversion from the pump wavelength to the second-harmonic of the signal wavelength is very efficient since both nonlinear conversion processes are phase-matched in the same crystal. In this experiment, we also demonstrated the tuning of such device by rotating the crystal in conjunction with changing the pump laser wavelength. To our knowledge, this experiment is the first demonstration of an OPO employing simultaneous phase matching.

5.2 Self-doubling KTA OPO

This experiment is very similar to the experiment based on the KTP crystal described in Section 5.1. In this SD-OPO, we use a 20-mm-long KTA crystal that is cut for collinear phase matching along the $\theta = 90°$ and $\phi = 0°$ direction. As described in Section 4.2.2, we use type-II phase matching for both optical parametric oscillation and simultaneous SHG; the pump beam at 796 nm and the signal beam at 1150 nm are both p-polarized (horizontal, fast crystal axis), and the idler beam at 2586 nm is s-polarized (vertical, slow crystal axis), the fundamental beam at 1150 nm has both p-polarized and s-polarized components, and the second-harmonic beam at 575 nm is p-polarized. This polarization geometry belongs to class-C SD-OPOs. The crystal has antireflection coatings for the signal, pump, and second-harmonic wavelengths on both surfaces.

Our experimental setup shown in Figure 5.6 is similar to the experimental setup in Section 5.1 with some major differences. A mode-locked Ti:Sapphire laser provides the

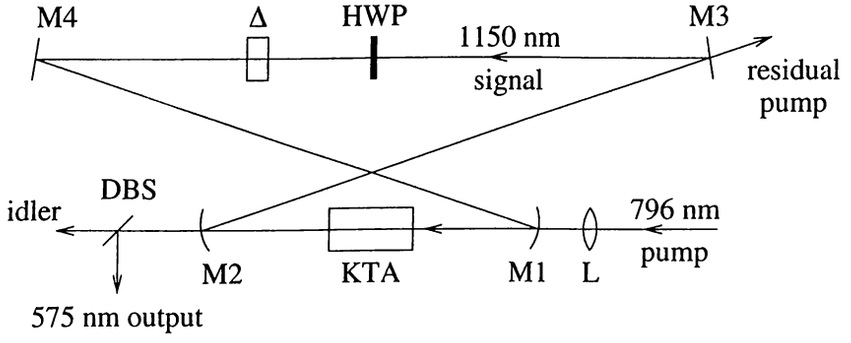

Figure 5.6: Experimental setup of the SD-OPO. A mode-locked Ti:sapphire laser at a wavelength of 796 nm provides the pump beam.

pump beam to the OPO at a wavelength of 796 nm with a pulse width of 140 fs. We constructed a ring cavity consisting of four mirrors M1, M2, M3 and M4. Although the curvature of the mirrors are same as those in the KTP experiment (M1 and M2 are 100 mm radius of curvature concave, and M3 and M4 are flat), their coatings are different. All mirrors are high reflectors at the signal wavelength. The KTA crystal is again positioned at the intracavity focus between M1 and M2. The fast axis of the crystal is parallel to the horizontal plane coinciding with the polarization of the pump beam. The pump beam is focused into the crystal with a lens (L) of focal length 50 mm and enters the cavity through M1, which has high transmission coatings for this purpose. The lowest order transverse mode of the cavity has a 30 μm diameter (calculated), and the focused pump beam has a 62 μm diameter (measured) at the crystal. We also use an intracavity HWP to rotate the polarization of the signal beam. The frequency-doubled yellow beam at 575 nm exits the cavity through M2, which is coated for high-transmission at this wavelength and high-reflection at the pump wavelength. This optic is also transparent to the idler beam. An external DBS is used to separate the output yellow beam from the idler beam. The diverging output beam is collimated with a lens (not shown). The residual pump beam leaves the cavity through M3.

In this experiment, to increase the interaction length of SHG inside the KTA crystal, we try to achieve better temporal overlap between the s and p-polarized components of the signal pulses (see Section 4.1.2) by using a birefringent crystal as a retarder (Δ). The retarder provides a fixed time delay between the these components of the signal beam after the intracavity signal polarization is rotated with the HWP. If this time delay were not present, the two orthogonally-polarized signal pulses would enter the crystal synchronously, and start walking away from each other due to GVM. (The calculated GVM for these pulses is 300 fs/mm.) However, the retarder provides a fixed time delay of 1.48 ps, so that the s-polarized signal pulse leads the p-polarized signal pulse by approximately 0.45 mm before entering the crystal. Once inside the crystal, the p-polarized pulse catches up with the s-polarized pulse approximately 5 mm from the input facet. As a result, this arrangement essentially doubles the effective crystal length that is available for SHG.

As in the case of the KTP SD-OPO experiment in Section 5.1, the resonant intracavity

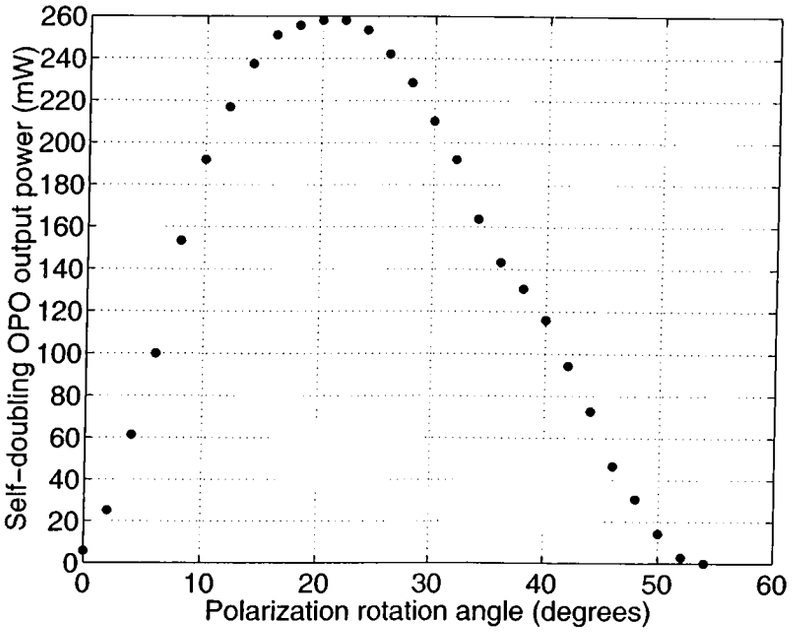

Figure 5.7: SD-OPO output power at 575 nm as a function of polarization rotation angle.

signal power is coupled out of the cavity by means of nonlinear SHG. When there is no intracavity polarization rotation, the intracavity signal beam does not have an s-polarized component, resulting in little frequency doubling. In this case, the OPO threshold is 51 mW. At an input pump power of 655 mW, the pump beam is depleted by 87%, showing strong parametric conversion.

As we start rotating the intracavity signal polarization by rotating the HWP, a portion of the p-polarized intracavity signal is coupled into s-polarization, and phase-matched SHG begins to take place. Figure 5.7 shows the output second-harmonic power at 575 nm as a function of the intracavity polarization rotation angle. As the polarization rotation angle is increased, the second-harmonic output power increases up to a maximum, and then begins to decrease as a consequence of reduced intracavity signal power. Rotating the signal polarization effectively increases linear cavity losses as in the case of the experiment in Section 5.1, and the OPO falls below threshold at one point. At a pump power of 655 mW, the second-harmonic output power reaches a maximum value of 258 mW at a polarization rotation angle of 22°, and the OPO falls below threshold at 54°. At the maximum point, the power conversion efficiency from the input pump beam to the output second-harmonic beam is 39.4%, and the pump depletion is 82%. We note that in this case the s-polarized signal component is completely depleted at the

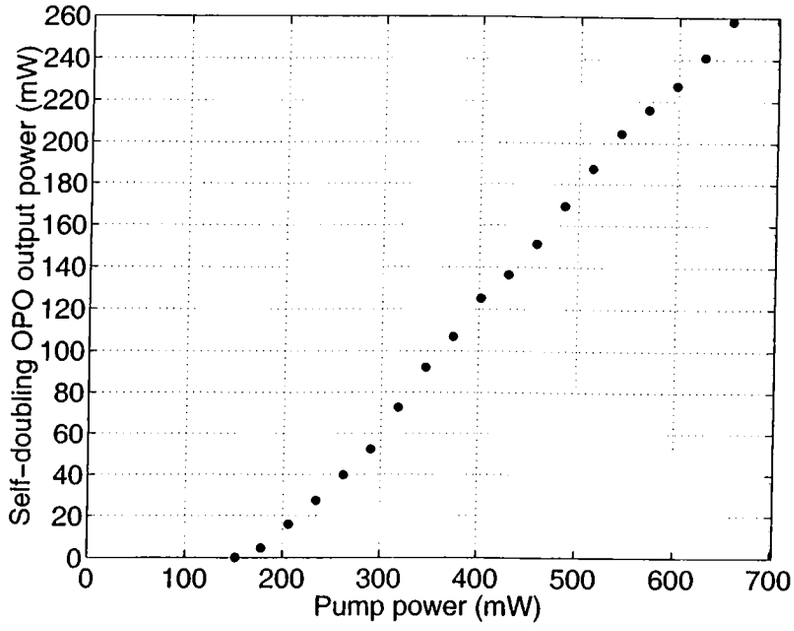

Figure 5.8: SD-OPO output power at 575 nm as a function of input pump power while the retarder rotation angle is held fixed at 22°.

exit facet of the crystal. Our 39.4% power conversion efficiency corresponds to a photon conversion efficiency of 56.4%. Figure 5.8 shows the output second-harmonic power as a function of input pump power at a constant polarization rotation angle of 22°. In this case, the increased OPO threshold is 151 mW.

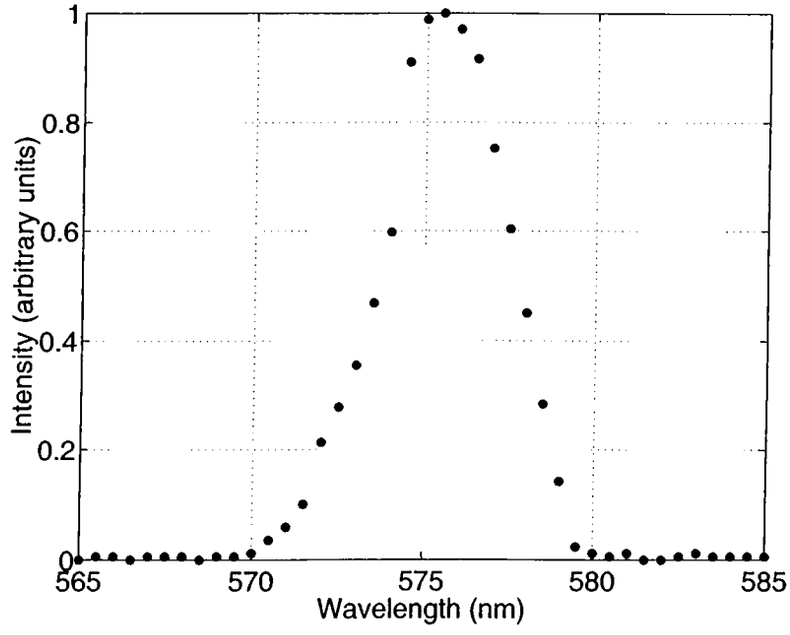

Figure 5.9: Spectrum of the SD-OPO output.

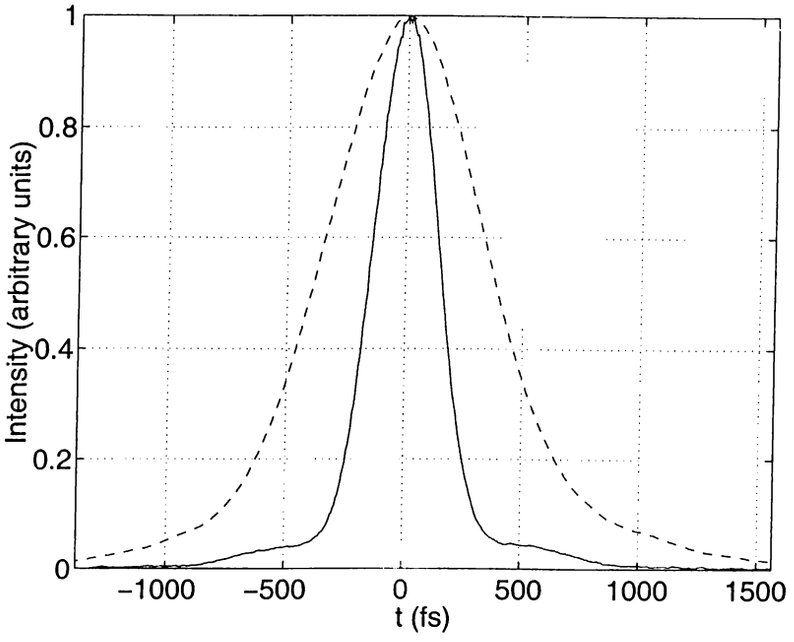

Figure 5.10: Autocorrelation traces of the SD-OPO output before (dashes line) and after (solid line) external pulse compression.

The spectrum of the yellow output beam as measured by a monochromator is shown in Figure 5.9. The output spectrum is narrower than those of the pump and the intracavity signal. The autocorrelation width of the yellow output pulses is measured to be 789 fs. Compared to the previous SD-OPO experiments based on KTP, it is longer by 64%. This pulse broadening is due to both GVM in the KTA crystal and group velocity dispersion in the KTA and retarder crystals. In this case, we used an external two-prism double-pass pulse compressor composed up of two SF-10 isosceles Brewster prisms, and reduced the autocorrelation width of the output to 318 fs. Figure 5.10 shows the autocorrelation of the output pulses before and after the pulse compressor. The transverse profile of the yellow output beam as measured with a CCD camera is nearly Gaussian.

In summary, we have demonstrated a SD-OPO that employs a single KTA crystal. The two-step conversion from the pump wavelength to the second-harmonic of the signal wavelength is again very efficient. Providing a delay between the two orthogonally polarized signal components to partially alleviate GVM effects that reduce interaction length contributes to this high efficiency. To our knowledge, our conversion efficiency from the pump to the second-harmonic is the highest value reported to date for an intracavity frequency-doubled OPO.

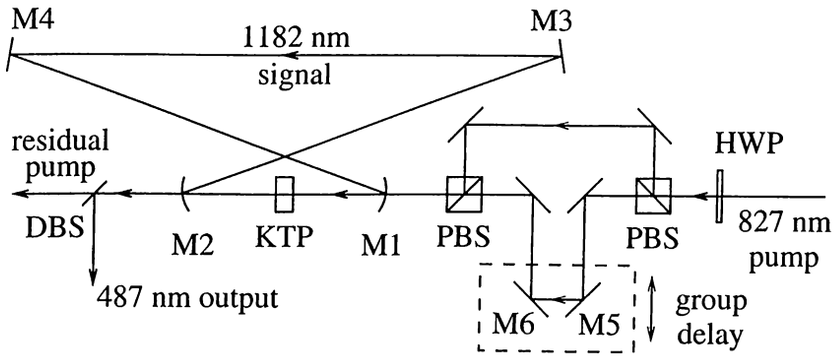

Figure 5.11: The experimental setup for the SF-OPO. A mode-locked Ti:Sapphire at a wavelength of 827 nm is used as the pump beam.

5.3 Sum-frequency-generating KTP OPO

In these experiments, we employ one of two KTP crystals (1.5 mm and 5 mm long). Both of these are cut for collinear phase matching with $\theta = 90°$ and $\phi = 0°$. As described in Section 4.2.1, we use type-II phase matching for both optical parametric oscillation and simultaneous SFG between the pump and the signal beams; the pump beam at 827 nm and the signal beam at 1182 nm are both p-polarized (horizontal, fast crystal axis), and the idler beam at 2756 nm is s-polarized (vertical, slow crystal axis), the sum-frequency beam at 487 nm is p-polarized. In this experiment, we need a polarization rotation of the pump beam (instead of a signal beam as in the case of the SD-OPO experiments based on KTP and KTA). The polarization geometry of this experiment belongs to class-C SF-OPOs.

Figure 5.11 shows our experimental setup where we use a ring cavity similar to those in the SD-OPO experiments which consist of four mirrors that are high reflectors at the signal wavelength. M1 and M2 are 100 mm radius of curvature concave, and M3 and M4 are flat. The 5 mm long KTP crystal is placed at the intracavity focus between M1 and M2 with the fast axis parallel to the horizontal plane. The KTP crystal has anti-reflection coatings at the signal wavelength.

A mode-locked Ti:Sapphire laser that has 170 fs long pulses provides the p-polarized pump beam at a wavelength of 827 nm. A HWP placed at the output of the laser provides adjustable polarization rotation for the pump beam. For a polarization rotation angle of φ, a $\cos^2\varphi$ fraction of the laser beam becomes the p-polarized OPO pump, whereas the

remaining $\sin^2\varphi$ fraction provides the s-polarized SFG input. These two polarization components are separated and recombined with the use of two polarizing beamsplitters (PBS). As a result, a variable group delay can be introduced between the pulses to compensate for the GVM experienced by the two polarization components inside the KTP crystal.

The recombined pump beam is focused with a lens (not shown) of focal length 50 mm and enters the cavity through M1 which has high transmission coatings at the pump wavelength. The maximum pump power available to us in these experiments is 525 mW, measured before the focusing lens and is dropped to 515 mW going through the focusing lens and M1, experiencing a total loss of 1.9%. The lowest order transverse mode of the cavity has a 35 μm diameter (calculated) and the focused pump beam has a 48 μm diameter (measured) at the crystal. The blue sum-frequency beam exits the cavity through M2 which has 83% transmittance at this wavelength. This optic is also transparent at the pump and idler wavelengths. The diverging output beams are collimated with a lens (not shown) after M2. The sum-frequency beam is separated from the residual pump and the idler beams with a dichroic beam-splitter (DBS). This beam experiences a total loss of 24% going through the second KTP surface (4.3%), M2 (17%), the recollimating lens (2.5%), and DBS (2.6%), since these surfaces were not coated specifically at the sum-frequency wavelength. The signal beam coming out through M3 is used to measure the intracavity signal power.

When the polarization rotation angle is zero, we observe a weak blue output beam ($\sim$ 4 mW at 515 mW pump power) resulting from polarization impurity of the pump and/or non-phase-matched SFG because there is no s-polarized component at 827 nm. As we increase the polarization rotation angle φ, a portion of the pump beam is coupled to s-polarization and phase-matched SFG between the the resonant intracavity signal beam and the s-polarized pump beam begins to take place. This decreases the resonant intracavity signal beam. Rotating the pump polarization also decreases the p-polarized pump power available for the parametric generation process, decreasing the intracavity signal further. There is an optimum polarization rotation angle at which the blue output power is maximized. Further increase of the polarization angle decreases the output power until the SF-OPO falls below threshold.

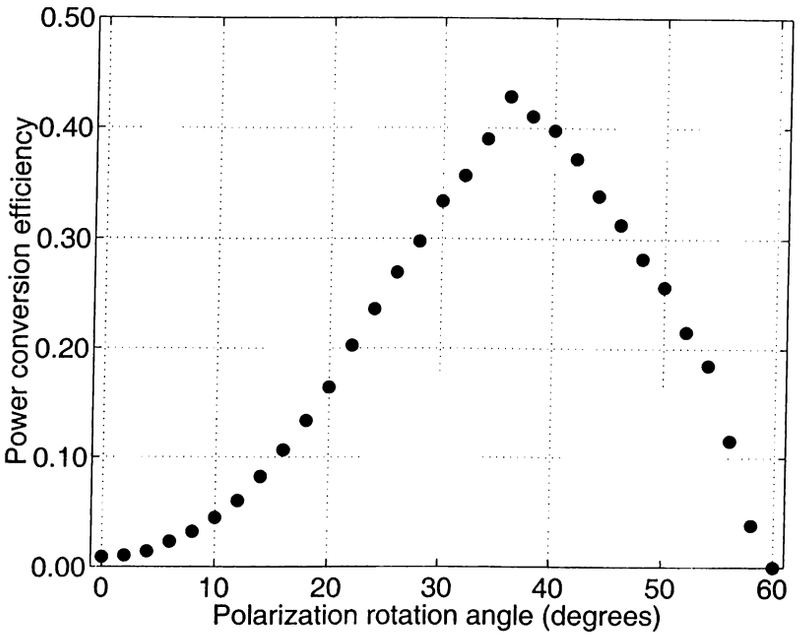

Figure 5.12: Power conversion efficiency as a function of polarization rotation angle. The pump power is 515 mW and the group delay is 2 ps.

The sum-frequency power show strong dependence to the delay introduced between the p and s-polarized components of the pump beam. We found that maximum conversion to the sum-frequency is achieved when the s-polarized component leads the p-polarized component by 2 ps.

The power conversion efficiency of the SF-OPO is the ratio of the sum-frequency power to the total pump power. Extra linear losses incurred by the pump beam at the input and by the sum-frequency beam at the output are taken into account to reflect the true conversion efficiency in the KTP crystal. Figure 5.12 shows the power conversion efficiency as a function of polarization rotation angle at a pump power of 515 mW and a delay of 2 ps. The highest output power is 221 mW at a polarization angle of 36°, corresponding to a power conversion efficiency of 43%.

The SF-OPO falls below threshold at a polarization angle of 60°. The p-polarized component of the pump at this angle is 129 mW, which is much larger than the 25 mW threshold of the OPO at zero polarization angle. This demonstrates that the parametric generation and SFG processes are strongly coupled to each other and s-polarized pump beam introduces. Since, the SFG process provides a nonlinear output

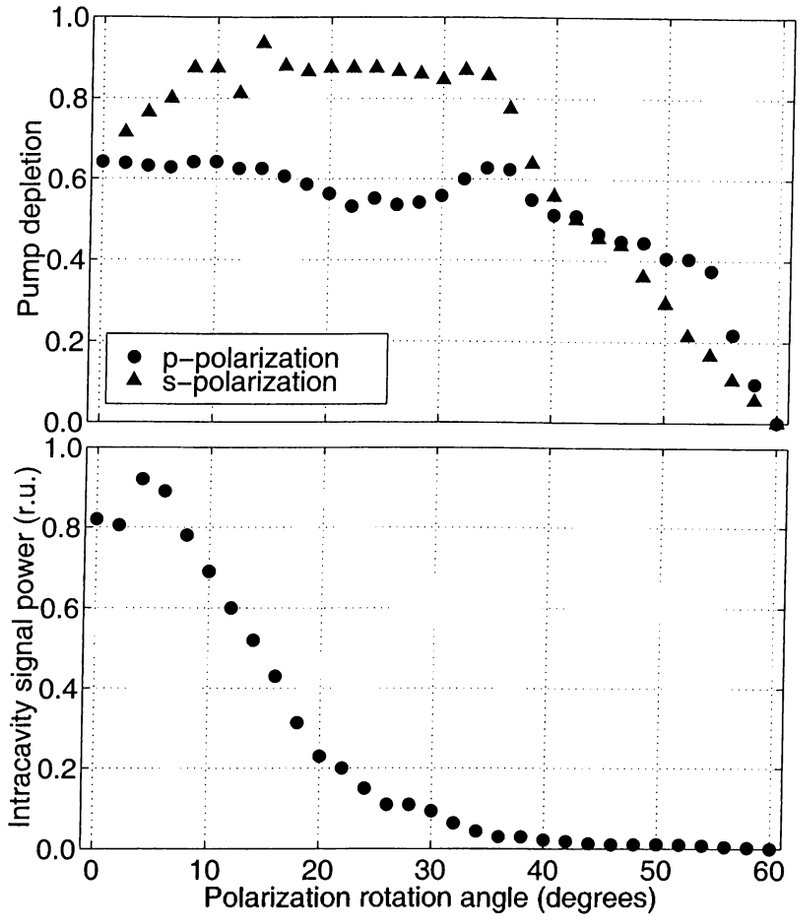

Figure 5.13: Pump depletion for the p-polarized (circles) and s-polarized (triangles) components and intracavity signal power (in relative units) as functions of polarization rotation angle. The pump power is 515 mW and the group delay is 2 ps.

coupling mechanism for the resonant signal field, the intracavity signal is decreased due to extra nonlinear loss caused by SFG. In contrast to the nonlinear loss introduced by SHG in the SD-OPO experiments based on KTP and KTA, the nonlinear loss caused by SFG effects the threshold of the OPO because there is always a s-polarized pump beam near the threshold power when the pump polarization is rotated.

Since two photons at the pump wavelength are annihilated to create one sum-frequency photon, the photon conversion efficiency of the SF-OPO is twice the ratio of the sum-frequency photon flux to the input pump photon flux, so that unity photon conversion efficiency as in the cases of the SD-OPO experiments represents total conversion. Our 43% power conversion efficiency corresponds to a photon conversion efficiency of 50%.

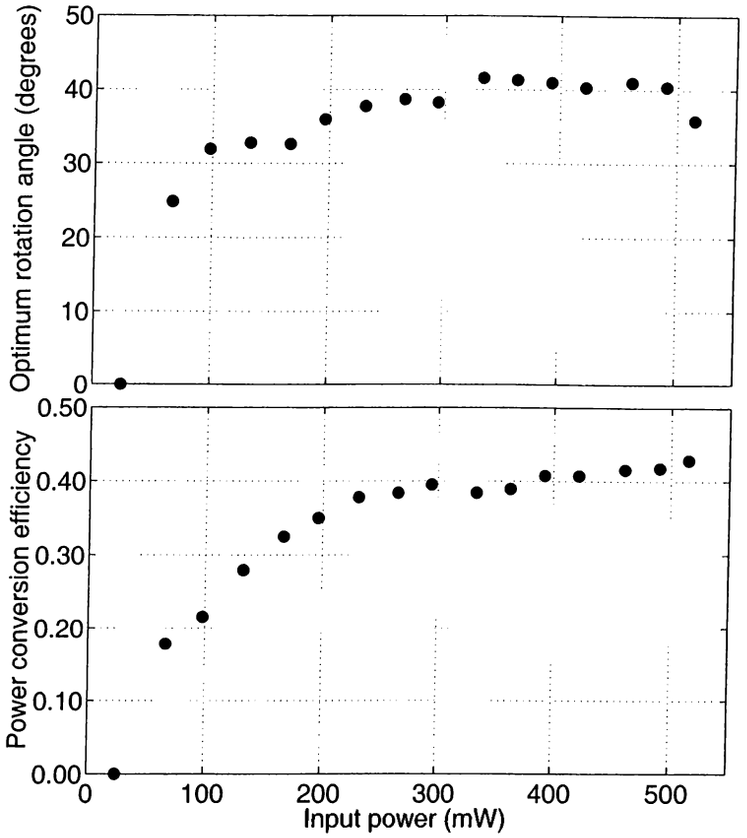

Figure 5.14: Optimum polarization rotation angle and maximum power conversion efficiency as functions of pump power.

Figure 5.13 shows the intracavity signal power and the depletion of the p and s-polarized components of the pump as functions of the polarization angle. At 36° where the conversion is highest, the intracavity signal power is only 3.7% of its value at 0°. Note that the depletion of the s-polarized component is very high and almost constant for a wide range of polarization angle values starting from a few degrees all the way to 36°. Increasing the polarization angle above its optimum value results in a rapid decline, since the intracavity signal power is no longer high enough to deplete the s-polarized pump component.

Figure 5.14 shows the power conversion efficiency as a function of pump power where at each power level the polarization angle is optimized to yield maximum output power. The polarization rotation angle that maximizes the output power at each pump power level is also shown in this figure. Note that neither the conversion efficiency nor the optimum angle change significantly for a wide range of the pump power.

As we mentioned before, the sum-frequency power has a strong dependence to the delay introduced between the p and s-polarized components of the pump beam because of the difference of the group velocities of the interacting pulses in the KTP crystal. The calculated group velocities of the interacting beams are 1.6631×10^8 m/s for the p-polarized pump, 1.5763×10^8 m/s for the s-polarized pump, 1.6896×10^8 m/s for the signal, 1.6094×10^8 m/s for the idler, and 1.5352×10^8 m/s for the sum-frequency [90]. Since the intracavity signal pulse is approximately synchronized with the p-polarized components of the pump pulse, it falls out of synchronization with the s-polarized components of the pump pulse, reducing the efficiency of the SFG process. To partially compensate for this mismatch, we adjust the group delay between the p and s-polarized components before the pump beam enters the cavity by translating M5 and M6.

Figure 5.15 shows the power conversion efficiency of the SF-OPO as a function of the

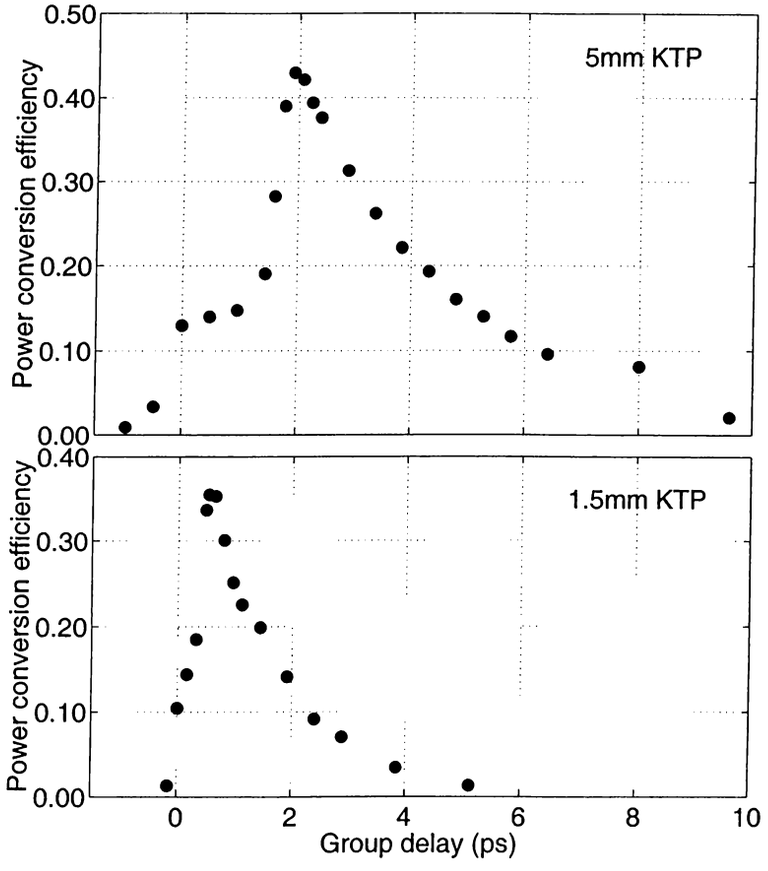

Figure 5.15: Power conversion efficiencies as functions of the group delay between the p and s-polarized pump components for 5 mm and 1.5 mm long KTP crystals. The p-polarized component is lagging the other for positive group delay values.

group delay between the orthogonally polarized pump components at the entrance of the crystal. At each value of the delay, the polarization angle is adjusted to maximize the output power, while the input pump power is kept constant at 515 mW. With no group delay adjustment setup, or with the delay adjusted to zero, we measure a maximum of 13% power conversion efficiency, at a polarization angle of 33°. Introducing a group delay of 2 ps increases the conversion efficiency by over three fold. This delay is approximately equal to the group velocity delay between the signal and the *s*-polarized pump component over 5 mm of KTP. For comparison, Figure 5.15 also shows a set of similar data with a 1.5 mm long KTP crystal instead. The power conversion efficiency is 10.5% with no delay. A 530 fs delay maximizes the power conversion efficiency to 35%. Since this crystal is shorter, it requires a shorter group delay at the input for maximum conversion.

It is possible to tune the SF-OPO output. Since, for a propagation direction, there

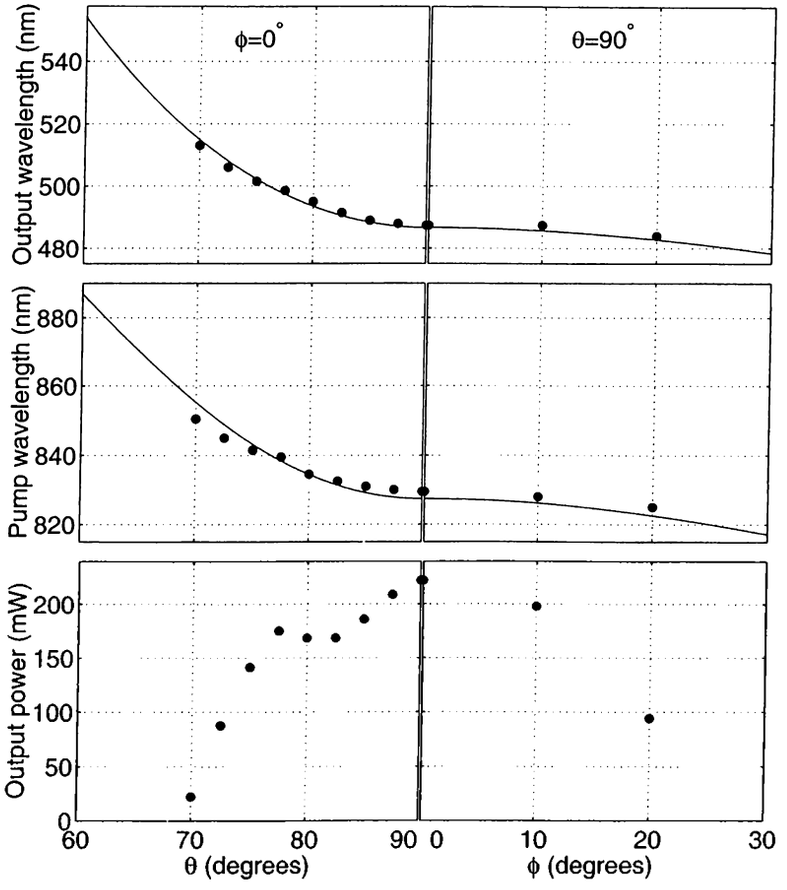

Figure 5.16: Calculated tuning curves and measured values of output wavelength, pump wavelength, and output power across the tuning range for the SF-OPO. Angles are internal to the crystal. The circles represent experimental data points.

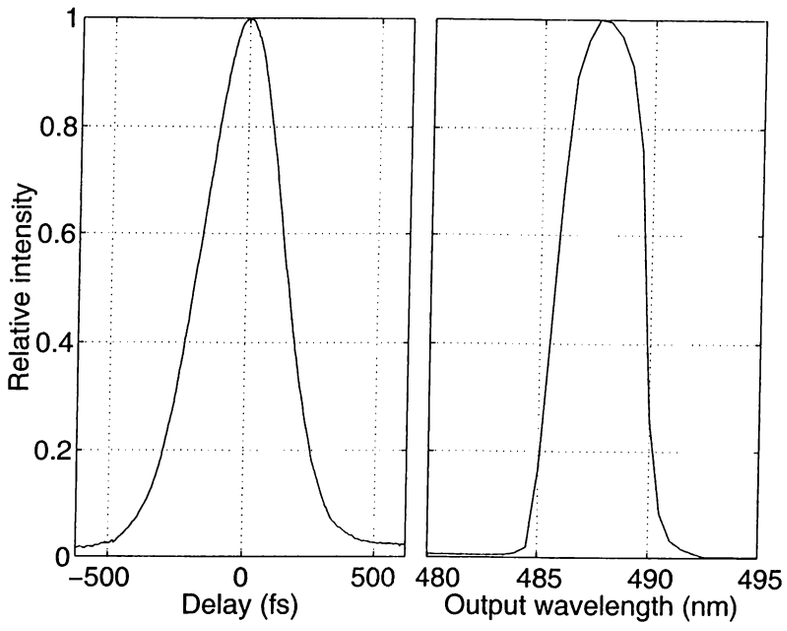

Figure 5.17: Autocorrelation trace (left) and spectrum (right) of the sum-frequency output beam.

is only one pair of a pump and a signal wavelengths for simultaneous phase matching of parametric oscillation and SFG (see Section 3.4.1), we need to vary the wavelength of the pump beam in conjunction with the crystal angles to tune the SF-OPO. Calculated tuning curves for the SF-OPO are shown in Figure 5.16 together with experimental data points. We have demonstrated tunability in the 484–512 nm range, being limited by the bandwidth of the cavity mirrors and reflection losses from the crystal surfaces. The experimental data shown in Figure 5.16 were obtained by maximizing the output power by adjusting the pump wavelength at each phase matching angle.

In the tuning of the device, the relatively long crystal causes some minor alignment problems like in the case of the SD-OPO with KTP crystal. Rotating the crystal not only changes the optical cavity length, but also shifts the beams laterally. These effects are easily compensated for by translating M3 and slightly realigning M2. The size of the transverse cavity mode and hence its overlap with the pump is influenced by the distance between M1 and M2, which also has to be readjusted after a rotation of the crystal.

The spectrum and the autocorrelation of the sum-frequency output are shown in Figure 5.17. The bandwidth of the spectrum is approximately 3.5 nm. The autocorrelation width of the sum-frequency pulses is measured to be 345 fs. When

deconvolved assuming a secant hyperbolic (sech) shape, this corresponds to a pulse width of 225 fs. This pulse broadening is again due to group velocity dispersion and GVM between the p-polarized pump and the signal pulses in the KTP crystal. When we use a 1.5 mm-long KTP crystal, the pulse width of the sum-frequency beam reduces to 195 fs because of reduced temporal overlap between the s-polarized pump and the signal.

In summary, we have demonstrated a SF-OPO where both parametric generation and SFG are phase-matched in a single nonlinear crystal for the same direction of propagation. This SF-OPO provides upconversion of an ultrafast Ti:sapphire laser with 43% power conversion efficiency (50% photon conversion efficiency) in the two step process from the pump to the signal and then to the sum-frequency. To our knowledge, this conversion efficiency is the highest value ever reported for an upconversion OPO.

5.4 PP-KTP OPO and SHG with BBO Crystal

In recent years QPM has emerged as a very promising alternative to birefringent phase-matching. A number of OPOs based on periodically-poled lithium niobate with cw, Q-switched, and short-pulse pumping have been recently demonstrated [21], [46], [95], indicating a great potential for quasi-phase-matched nonlinear crystals for use in broadly-tunable laser systems.

The technology for electric-field poling of lithium niobate has quickly matured relative to other ferroelectric materials, primarily due to the wide availability of high quality and inexpensive crystal substrates. One disadvantage of periodically-poled lithium niobate is that the large coercive field of $\sim$ 21 kV/mm limits the poled crystal thickness to approximately 0.5 mm. Another significant disadvantage is the presence of photorefractive damage. Although the photorefractive damage threshold is reduced in periodically-poled lithium niobate relative to bulk lithium niobate [96], satisfactory operation still requires heating the crystal in a temperature-controlled oven. Another material that has much promise for periodically-poled nonlinear optics applications is KTP. KTP has a much higher photorefractive damage threshold than lithium niobate,

permitting room-temperature operation without temperature control. The much lower coercive field of $\sim$ 2 kV/mm permits successful electric-field poling on samples of at least 1 mm thickness [92]. Many recent advances have been made in electric-field poling of KTP, indicating that PP-KTP may become the material-of-choice for many frequency conversion applications [97]. We designed the first femtosecond OPO based on a PP-KTP crystal in 1998 [69]. In the PP-KTP OPO, the conversion efficiency was considerably high, despite the presence of high cavity losses other than output coupling and a wide tunability range was demonstrated by changing the cavity length and the pump wavelength. As a result, in this experiment we tried intracavity SHG employing wide tunability of the PP-KTP OPO.

In our experiments, we use a z-cut 1 mm thick and 8 mm long hydrothermally grown KTP crystal for parametric amplification. Periodic domain inversion in the crystal was achieved by applying an electric field along the z-axis (1-mm dimension) with a 24 μm period electrode [92]. The resulting domain grating occupies the central 7 mm of the crystal. The orientation of the grating with respect to the polished crystal surfaces could not be controlled accurately, and there may be an angle of a few degrees between these surfaces and the grating. The polished crystal surfaces do not have any anti-reflection coatings. QPM allow phase matching of parametric oscillation, where the pump, signal and idler beams are all p-polarized (horizontal, slow axis, z-axis). As a result we utilize the large $\overleftrightarrow{\chi}^{(2)}_{ZZZ}$ nonlinear coefficient of KTP.

A second crystal of a 5 mm long BBO that is cut for a type-I phase matching along $\theta =$

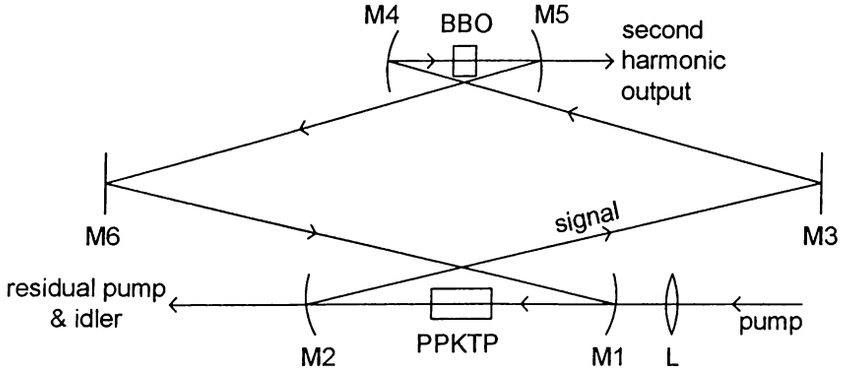

Figure 5.18: The intracavity-doubled OPO setup. The pump beam is provided by a mode-locked Ti:Sapphire laser.

20.8° and $\phi = 90°$ is employed to achieve intracavity SHG, where the fundamental beam is p-polarized (horizontal, slow axis, x-axis) and the second-harmonic beam is s-polarized (vertical). This crystal has anti-reflection coatings on both surfaces at wavelengths of 1300 nm and 650 nm.

A mode-locked Ti:Sapphire laser provides the pump beam to the OPO at a wavelength of 760 nm. The pump pulses are 180 fs in duration. We constructed a ring cavity consisting of six mirrors as shown in Figure 5.18. M1 and M2 are 150 mm radius of curvature concave, M4 and M5 are 50 mm radius of curvature concave and M3 and M6 are flat mirrors. All of the cavity mirrors are high reflectors at the signal wavelength. The PP-KTP crystal is positioned at the intracavity focus between M1 and M2 and BBO crystal is positioned at the intracavity focus between M4 and M5. The pump beam is focused with a lens (L) of focal length 75 mm and enters the cavity through M1, which has high transmission coatings for this purpose. The lowest order transverse mode of the cavity has 48 μm and 15 μm waist diameters (calculated) in the PP-KTP and the BBO crystals, respectively, and the focused pump beam has a 70 μm waist diameter (measured) in the PP-KTP crystal. M3 is placed on an open-loop piezo-controlled translation stage with the purpose of adjusting the cavity length

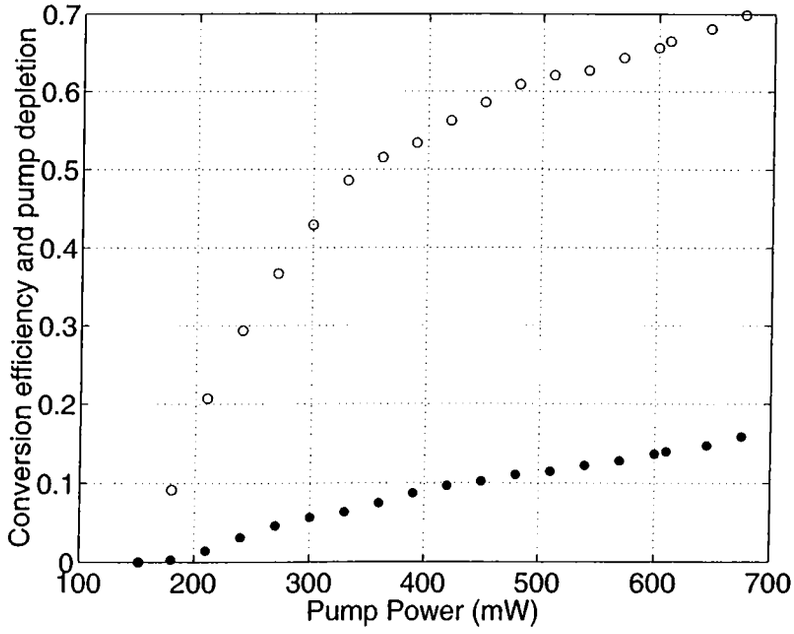

Figure 5.19: Conversion efficiency (filled circles) and pump depletion (open circles) versus pump power.

for synchronizing the pump and signal pulses. The idler and the residual pump beams exit the cavity through M2. Various visible beams resulting from non-phase-matched interactions (frequency-doubled pump and signal, sum of pump with signal and idler) also exit the cavity through M2.

The threshold of the OPO is measured to be 150 mW (measured pump power before the lens). At an input pump power of 675 mW, the maximum second-harmonic output from M5 is 107 mW, corresponding to a 15.9% power conversion efficiency, corresponding to a photon conversion efficiency of 19.5%. At this point, the pump depletion is measured to be 69%. Figure 5.19 shows the second harmonic power conversion efficiency and pump depletion as functions of the input pump power. Reflection losses suffered by the signal and the pump beams at the uncoated surfaces of the PP-KTP crystal are the most important factors limiting the performance of this OPO. The total loss experienced by the pump at the input (L, M1, and first crystal surface) is measured to be 10%. For the resonant signal beam, surface reflection losses per pass through the crystal are calculated to be 16%. It is expected to play a significant role in increasing the threshold and decreasing the conversion efficiency. This relatively high loss and the high pump depletion values suggest that the parametric gain in the PP-KTP crystal is very high.

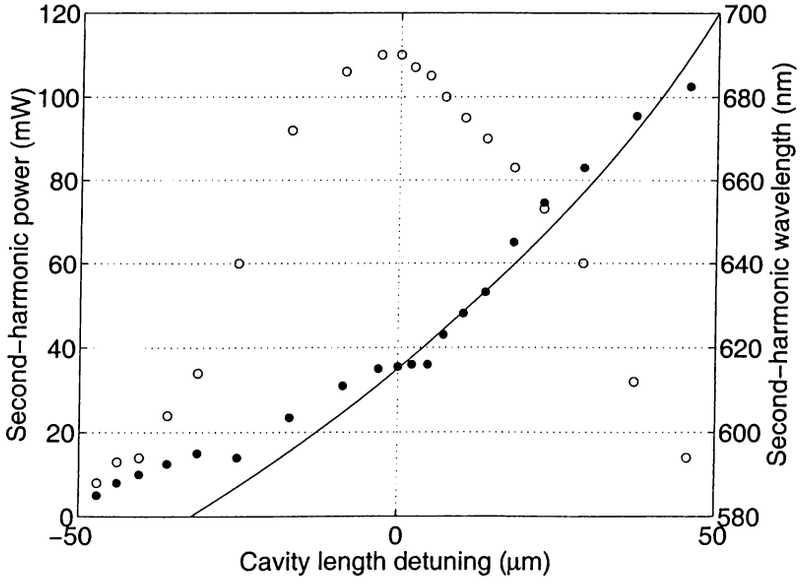

Figure 5.20: Measured second-harmonic output wavelength (filled circles) and power (open circles) versus cavity length detuning. The solid line is a calculated theoretical curve based on equating the wavelength dependent signal pulse round-trip time to the pump pulse period.

The second harmonic output of the PP-KTP OPO can be tuned over a 90 nm wide wavelength range by only changing the cavity length [69]. As we explained in Section 4.1.2, this effect is a consequence of the cavity round trip time for the signal pulse being dependent on wavelength through the contribution of the group velocity inside the crystal [28]. Detuning the cavity length by moving one of the cavity mirrors (M3) changes the wavelength of the signal pulses that are synchronous with the pump pulses. Figure 5.20 shows the measured second-harmonic wavelength as a function of cavity length detuning for a fixed pump wavelength of 760 nm and a fixed BBO angle. The theoretical tuning curve, based on the calculated cavity length dependence of the signal wavelength, is almost in agreement with the data. Figure 5.20 also shows the second-harmonic output power variation as the OPO is tuned by changing the cavity length. We use the location of the maximum second-harmonic output power to define the zero detuning point for the cavity length. The variation of second-harmonic output power with cavity length detuning is influenced by many factors such as the bandwidth of the cavity mirrors, and the GVM dependence of the parametric gain [98]. In this experiment, the cavity mirrors become poor reflectors above 1350 nm and below 1200 nm. Even though GVM between the signal and pump pulses limits the parametric interaction length to less than 1 mm, the much longer physical length of the crystal allows for cavity tuning of the signal wavelength. The autocorrelation width of the second-harmonic pulses are measured to be 360 fs. This pulse broadening is due to GVM between the signal and pump pulses in the PP-KTP crystal and GVM between the fundamental and second-harmonic pulses in the BBO crystal [98], [99].

In conclusion, we have demonstrated the first Ti:sapphire laser pumped femtosecond intracavity-doubled PP-KTP OPO operating in the 585-680 nm wavelength range. The conversion efficiency of the OPO is high, despite the presence of high cavity losses. Fast tunability is demonstrated by changing the cavity length.

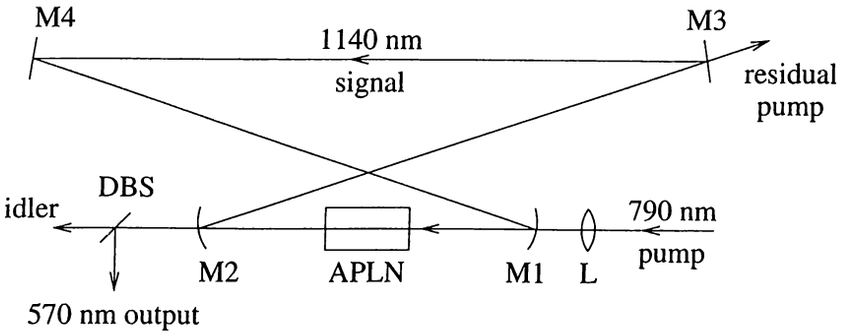

Figure 5.21: Femtosecond self-doubling OPO setup.

5.5 Self-doubling APLN OPOs

Our APLN crystal (see Section 4.2.5) was designed with an intracavity-pumped cw SD-OPO in mind, hence the crystal length is relatively long. However, by constructing a simple externally-pumped femtosecond SD-OPO [8], we wished to demonstrate the validity of our design method. As described in Section 4.2.5, the 20 mm-long $LiNbO_3$ crystal was x-cut and lithographic restrictions limited the poled length of the crystal to 18 mm. The pump beam at 790 nm, the signal beam at 1140 nm, the idler beam at 2573 nm and the second-harmonic beam at 570 nm are all p-polarized (horizontal, z-axis of the crystal). As a result we utilize the large $\overleftrightarrow{\chi}^{(2)}_{zzz}$ nonlinear coefficient of $LiNbO_3$.

The experimental setup shown in Figure 5.21 is similar to the SD-OPO experiments based on KTP and KTA in Sections 5.2 and 5.1. A singly-resonant ring cavity is formed by four mirrors that are highly reflecting at the signal wavelength. Mirrors M1 and M2 are 100-mm radius-of-curvature concave, and M3 and M4 are flat. The APLN crystal is placed in an oven that is kept at a temperature of 130 °C and positioned at the intracavity focus between M1 and M2. The crystal has antireflection coatings for the pump, signal, and second-harmonic wavelengths on both surfaces. A mode-locked Ti:Sapphire laser with 180 fs-long pulses provides the pump beam at 790 nm. The pump beam is focused with a lens (L) of focal length 50 mm and enters the cavity through M1. The focused pump has a 62-μm diameter (measured) and the lowest-order transverse mode of the cavity has a 30-μm diameter (calculated) at the crystal. We achieve the synchronization of signal and pump pulses by moving M3 with a piezo-electrically controlled mount. Mirror M2 is designed to transmit the second-harmonic beam and reflect the pump

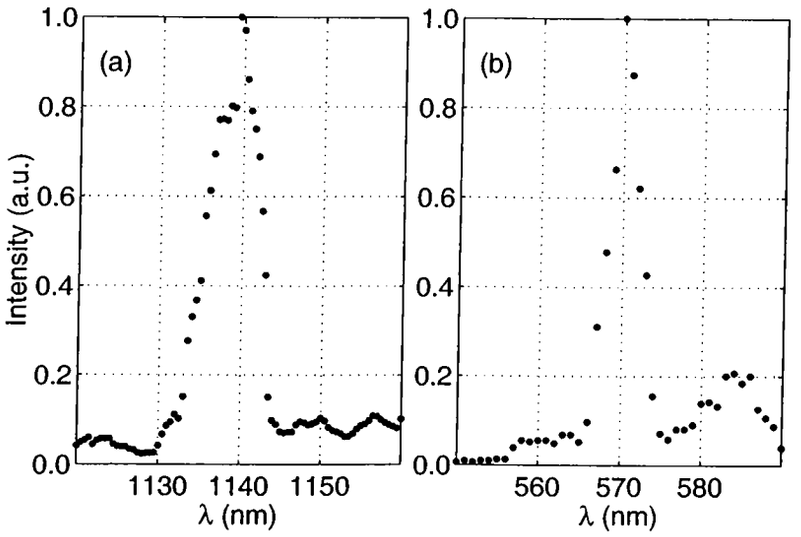

Figure 5.22: (a) Signal and (b) second-harmonic spectra at a pump wavelength of 790 nm for the second grating ($\beta = 0.72$).

beam. The residual (depleted) pump beam is separated from the second-harmonic beam at M2, and leaves the cavity through M3. A dichroic beam-splitter (DBS) separates the second-harmonic beam from the idler beam at the output.

When the pump beam is tuned to a wavelength other than the design wavelength of 790 nm, the signal beam that resonates inside the cavity assumes a value that keeps the

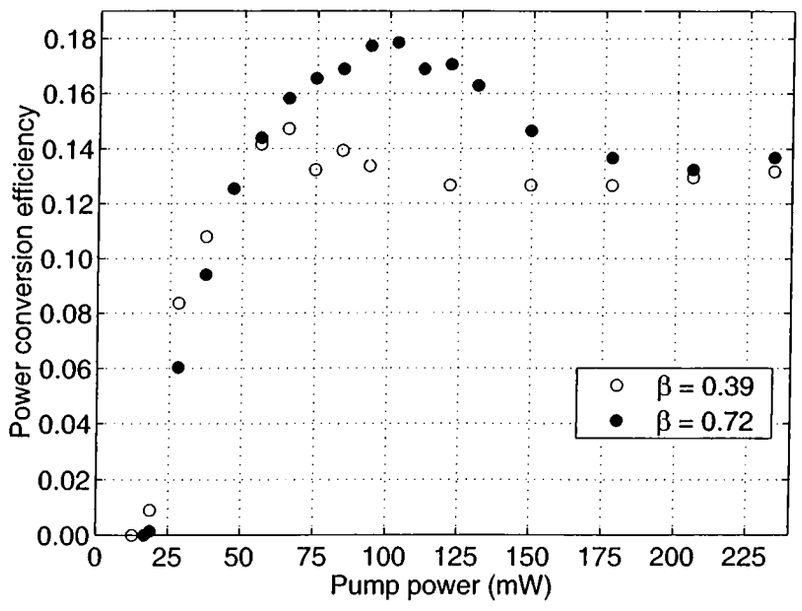

Figure 5.23: Power conversion efficiency as a function of the pump power for the first ($\beta = 0.39$, empty circles) and second ($\beta = 0.72$, filled circles) gratings.

OPO process phase-matched (if possible). In this case the SHG process is not phase-matched, and only a weak parasitic second-harmonic beam is produced. Since there is no output coupler at the signal wavelength, the OPO cavity is severely under-coupled. When the pump beam is tuned to 790 nm, the SHG process becomes simultaneously-phase-matched with the OPO process, and a strong second-harmonic beam is produced. This reduces the intracavity signal power, since the SHG process draws power from the signal beam. We measured the wavelengths of the pump, signal and second-harmonic beams to be consistent with those initially chosen. Figure 5.22 shows the signal and second-harmonic spectra for the grating with $\beta = 0.72$ when the pump wavelength is 790 nm. The spectra for the grating with $\beta = 0.39$ are similar.

Figure 5.23 shows the power conversion efficiency as a function of the input pump power for both gratings. The threshold of the SD-OPO with the $\beta = 0.72$ grating is 17 mW. This device produces 32 mW of output power at the second-harmonic wavelength when the pump power is 234 mW, corresponding to a power conversion efficiency of 13.7%. The maximum power conversion efficiency is 17.9% at 103 mW of pump power. This corresponds to a photon conversion efficiency of 25.7%. For the SD-OPO with the $\beta = 0.39$ grating, the maximum second-harmonic output power is 31 mW at a pump power of 234 mW, corresponding to a 13.2% power conversion efficiency. The maximum power conversion efficiency is 14.7% at 65 mW of pump power, corresponding to a photon conversion efficiency of 21.2%. The general shape of the efficiency curves in Figure 5.23 are consistent with the plane-wave results of class-A SD-OPOs as reported in [42].

Group velocities of the pump, signal, idler, and second-harmonic pulses propagating inside the APLN crystal are all different. This group velocity mismatch (GVM) results is a spatial separation of these pulses as they propagate. This effect has profound consequences on the behavior of the femtosecond SD-OPO. The effective interaction length is limited to distances dictated by GVM. Calculated inverse GVM terms for the pump–signal, pump–idler, signal–idler, and second-harmonic–signal pulses are 222 fs/mm, 286 fs/mm, 64 fs/mm, and 699 fs/mm, respectively [93]. The effective interaction length of the pump and signal pulses in the OPO process is approximately 0.8 mm. Even for such a short interaction length, we achieve large pump depletion ($> 50\%$), indicating a strong pump–signal interaction. However, the relatively high

GVM between the signal and second-harmonic pulses is the limiting factor for the overall conversion efficiency. Another consequence of GVM is a severe broadening of the second-harmonic pulses. A signal pulse generates second-harmonic power as it propagates over the whole length of the crystal; the second harmonic generated at earlier portions travel slower than the signal pulse and fall behind as new second harmonic is generated further down the crystal. We measured the second-harmonic output pulse-width to be 2.4 ps. This value is on the same order of magnitude with the total delay between the signal and second-harmonic pulses over the entire length of the crystal.

Photon conversion efficiencies reaching 26% is a strong indication that the OPO and SHG interactions are simultaneously-phase-matched in the APLN crystal. Detuning the pump wavelength by less than 0.5 nm from the peak reduces the second-harmonic output by more than 90%.

In summary, our method described in Section 3.5 facilitates the design of aperiodic grating structures to simultaneously quasi-phase match two arbitrary second-order nonlinear processes within the same crystal. This method is much simpler than previous approaches to the same problem. Since the relative strength of the two processes can be adjusted freely, the conversion efficiency of the overall process can be optimized. The femtosecond SD-OPO provides experimental verification of our method.

Chapter 6

Continuous-wave Experiments

In this chapter, we present our experiments on cw OPOs that employ simultaneous phase matching for frequency upconversion. We performed two SD-OPO experiments based on KTA and APLN crystals. In these experiments, we designed a cw Ti:sapphire laser and a cw intracavity OPO to reach high intensity necessary for the cw OPO. This design technique is used in various singly-resonant cw OPOs [70]–[73].

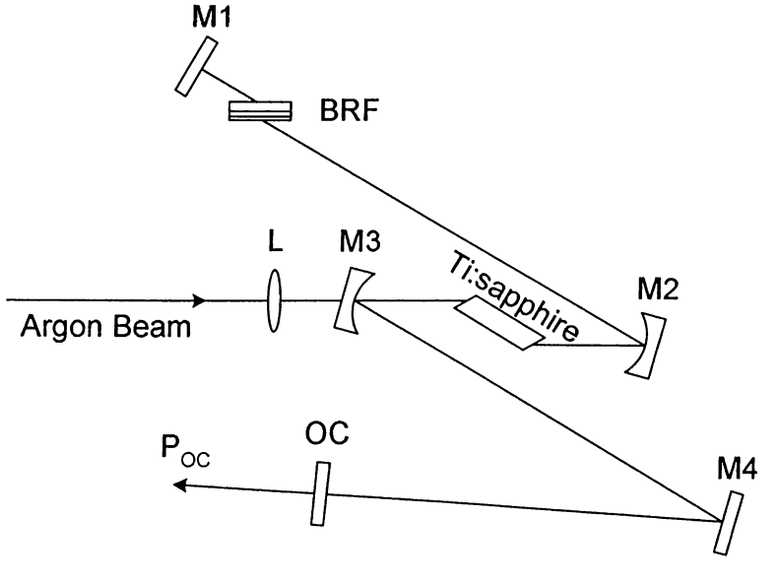

Figure 6.1: Ti:sapphire laser setup.

6.1 Continuous-wave Ti:sapphire Laser

In this laser, a 2-cm-long Brewster-cut Ti:sapphire crystal is used. The figure of merit (the ratio of absorption coefficients at 514 nm and 800 nm) of this crystal is measured to be 80 ± 20. Figure 6.1 shows the laser setup. It is based on a linear cavity made up of five mirrors. All mirrors except the output-coupler (OC) are high reflectors; M1 and M4 are flat, M2 and M3 are 150-mm radius-of-curvature concave. OC is a flat output-coupler mirror with 83% reflectivity. The Ti:sapphire crystal is positioned at the intracavity focus between M2 and M3 with horizontal plane of incidence at Brewster surfaces. An argon-ion laser (Coherent, Innova 300) provides the p-polarized pump beam to the Ti:sapphire laser. This beam is focused with a lens (L) of focal length 100 mm and enters the cavity through M3, which has high transmission coatings for this purpose. Horizontal and vertical beam diameters inside the Ti:sapphire crystal are 38×22 μm for the Ti:sapphire beam and 49×30 μm for the argon pump beam. This cavity design provides an elliptic beam of 0.7×1.2 mm dimensions on the output-coupler mirror in the horizontal and the vertical directions, respectively. The thermal lensing effect in the Ti:sapphire crystal caused by high intensity of the Argon-ion laser made it difficult to design the Ti:sapphire laser cavity. The threshold of the Ti:sapphire laser with the output-coupler is 3.6 W. At an argon pump power of 7.7 W, the laser produces p-polarized output with a power of 1.6 W. When OC is replaced by a flat high-reflector mirror, the threshold of the Ti:sapphire laser is 1.1 W. The tuning of the laser is achieved by a birefringent tuner (BRF).

6.2 Continuous-wave Self-doubling KTA OPO

Our cw SD-OPO is based on a KTA crystal that we used in the femtosecond SD-OPO experiment in Section 5.2. The crystal is a 20-mm-long KTA crystal that is cut for collinear phase matching along the $\theta = 90°$ and $\phi = 0°$ direction. A type-II polarization geometry is employed to achieve parametric generation, where both the pump at 799.0 nm and the signal at 1148.5 nm are p-polarized (horizontal, fast axis, y-axis), and the idler is s-polarized (vertical, slow axis, z-axis). Frequency doubling of

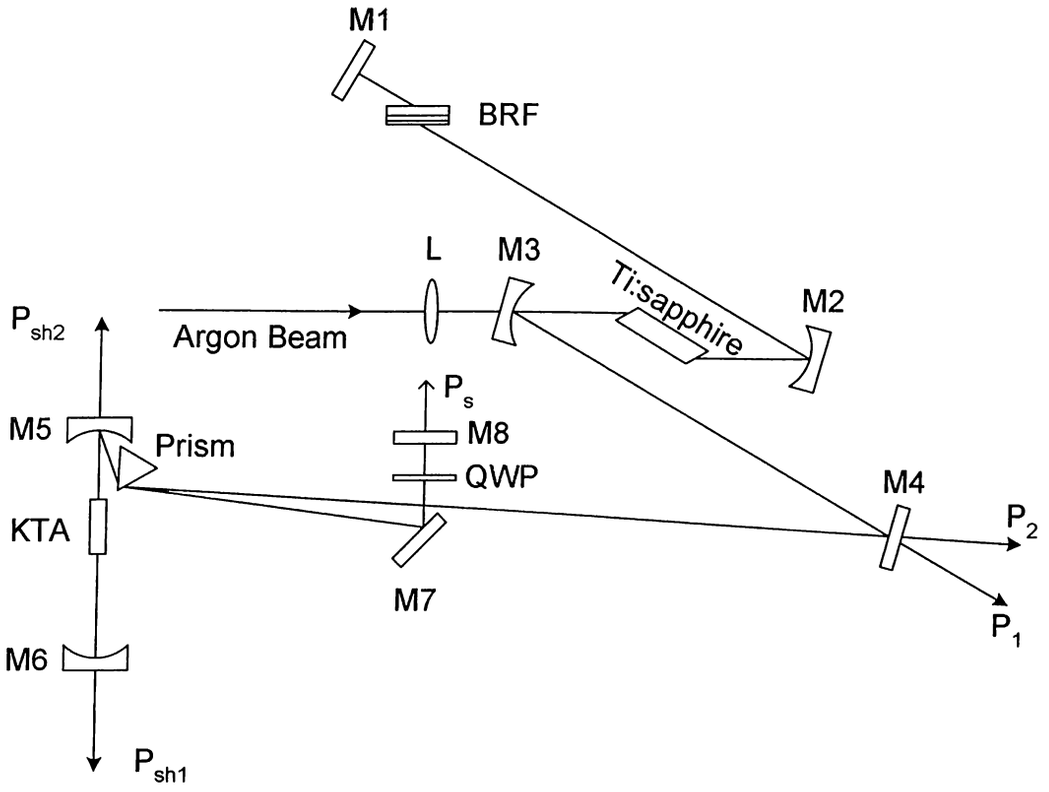

Figure 6.2: Continuous-wave SD-OPO setup.

the signal beam is also type-II phase-matched for the same direction of propagation; the fundamental beam at 1148.5 nm has both p-polarized and s-polarized components, and the yellow second-harmonic beam at 574.2 nm is p-polarized. This polarization geometry belongs to class-C SD-OPOs as defined in [42]. The crystal has antireflection coatings for the signal, pump, and second-harmonic wavelengths on both surfaces.

Our experimental setup is shown in Figure 6.2. The laser cavity formed by M1, M2, M3, M4, M5, and M6 and the OPO cavity formed by M8, M7, M5, and M6 are linear cavities and are coupled together using a SF-10 isosceles Brewster prism. M5 and M6 are common to both cavities. M5 is a 100-mm radius-of-curvature concave and M6 is a 75-mm radius-of-curvature concave. Both M5 and M6 are high-reflector for both the OPO signal beam and the pump beam produced by the Ti:sapphire laser. In addition, they have high transmission coatings for second-harmonic output. The cw Ti:sapphire laser used in this experiment is an extended version of the Ti:sapphire laser designed in Section 6.1. We removing the output-coupler mirror and extended its cavity by adding an OPO cavity part. The newly-added OPO cavity part after the output-coupler is

designed to preserve the mode shape at the place of the output-coupler and to provide a circular beam waist in the KTA crystal. The lowest order transverse mode of the cavity forms an intracavity focus with a diameter of 25 μm and 28 μm (calculated) for the signal and the pump beams respectively between M5 and M6 with the KTA crystal placed at the focus. The fast axis of the crystal is parallel to the horizontal plane coinciding with the polarization of the pump beam. M7 and M8, which are high reflectors at the signal wavelength, complete the SD-OPO cavity. An intracavity quarter-wave plate (QWP) is used to couple a portion of the *p*-polarized signal beam to *s*-polarization to facilitate type-II phase-matched SHG. We use the QWP instead of a HWP because the signal beam coming from the KTA crystal section of the cavity passes twice through the QWP before going into the KTA crystal section of the cavity again. The frequency-doubled yellow beam exits the cavity through M5 and M6. These optics are also transparent to the idler beam at 2625 nm. At each output, the diverging output beam is collimated with a lens (not shown) and the second-harmonic beam separated with a prism (not shown). Intracavity power measurements of the Ti:sapphire and the SD-OPO are made by using weak beams coming out through high reflectors M4 and M8 as described in Section 4.4.

With the addition of the OPO cavity, the Ti:sapphire laser threshold is increased to 2.12 W. When we block the OPO operation, the intracavity Ti:sapphire laser powers P_1 and P_2 (incoming and outgoing to the OPO section) are 30.9 W and 29.1 W at an argon power of 7.7 W. This corresponds to 5.8% losses in the OPO section including M4. When there is no intracavity polarization rotation (either the QWP is removed from the cavity or its fast and slow axes are aligned with those of the KTA crystal), the intracavity signal beam does not have an *s*-polarized component, resulting in little frequency doubling (only due to parasitic interactions). The threshold of this OPO is 3.6 W. The intracavity Ti:sapphire laser powers P_1 and P_2 and the intracavity signal power P_s are 14.1 W, 13.0 W and 5.7 W at an argon power of 7.7 W. When the OPO is working, the loss experienced by the Ti:sapphire laser in the OPO section is also increased to 7.8%. As we start rotating the intracavity signal polarization by rotating the QWP, a portion of the *p*-polarized intracavity signal is coupled into *s*-polarization,

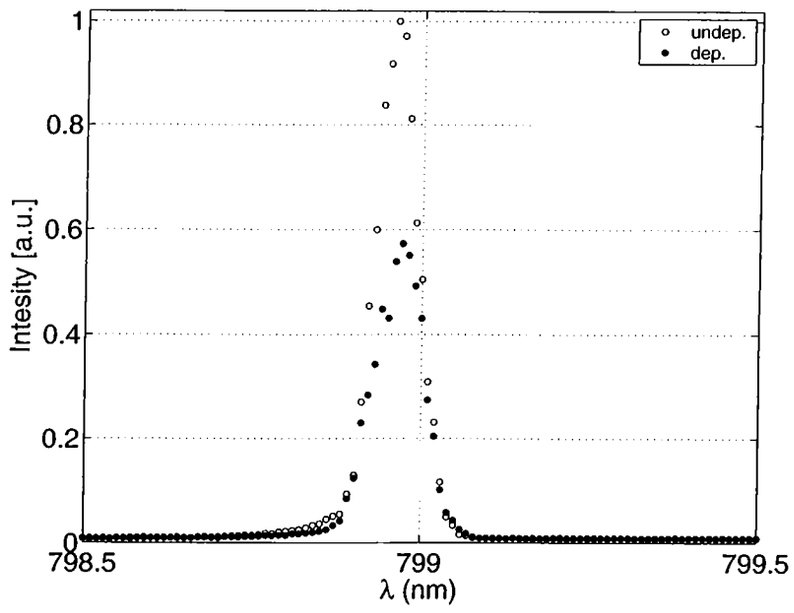

Figure 6.3: Pump spectrum with and without optical parametric oscillation.

and phase-matched SHG begins to take place. At an argon power of 7.7 W, the second-harmonic powers P_{sh1} and P_{sh2} reach their maximum values of 23 mW and 14 mW at a polarization rotation angle of 6°, respectively. At this maximum point, the threshold of the OPO is increased to 4.0 W. The intracavity Ti:sapphire laser powers P_1, P_2, and P_s are 19.7 W, 18.4 W, and 4.1 W at an argon power of 7.7 W, respectively. The intracavity signal power is reduced due to the linear loss caused by the QWP and the loss due to

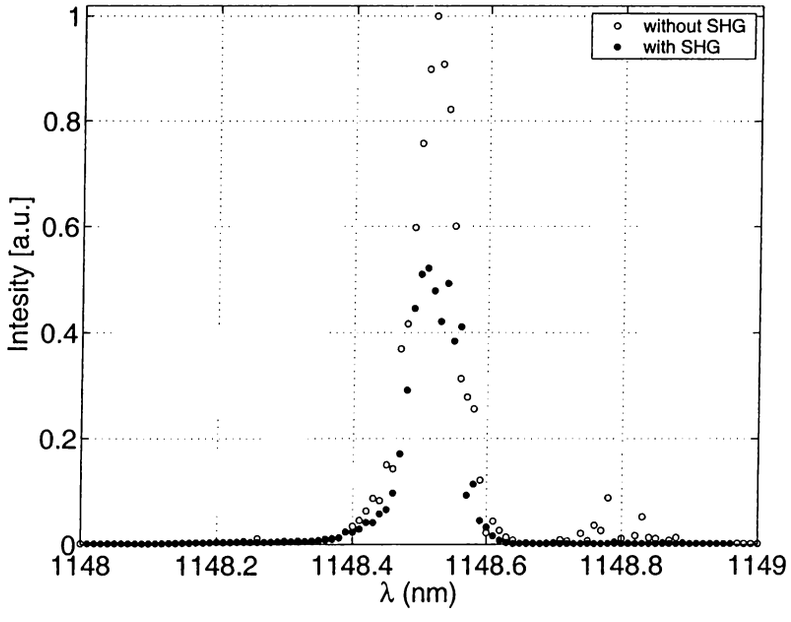

Figure 6.4: Signal spectrum with and without SHG.

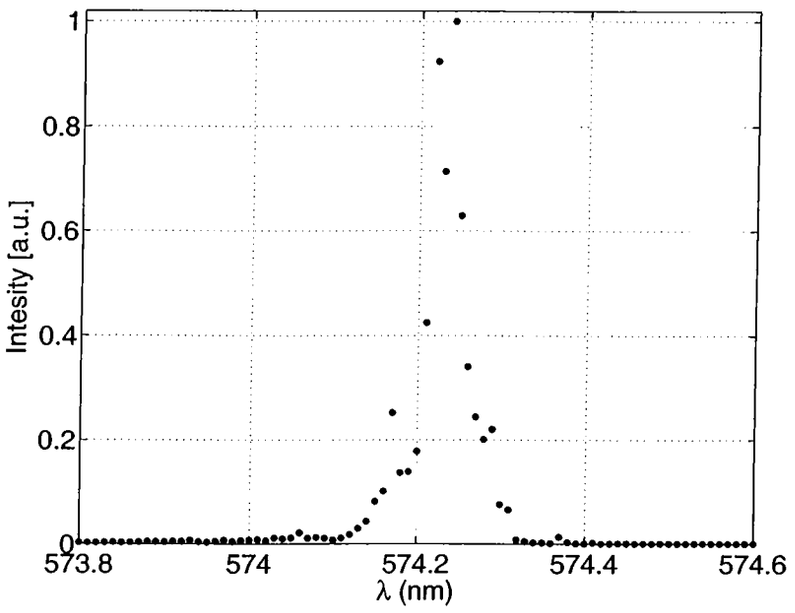

Figure 6.5: Second-harmonic spectrum.

SHG. This drop in the signal power also effects the nonlinear loss of Ti:sapphire pump beam. At this condition, the loss experienced by the Ti:sapphire laser in the OPO section is dropped to 6.6%. The OPO falls below threshold at 12°.

The spectrum of the pump beam with and without optical parametric oscillation as measured by a monochromator (CVI Laser Digikröm 240) is shown in Figure 6.3. This spectrum shows that the operation of the OPO does not affect the operation of the Ti:sapphire laser. Similarly, the spectrum of the signal beam with and without SHG is shown in Figure 6.4. SHG does not effect the operation of the OPO. The spectrum of the yellow output beam is also shown in Figure 6.5. The transverse profile of the yellow output beam as measured with a CCD camera is nearly Gaussian.

In summary, we have demonstrated a cw SD-OPO that employs a single KTA crystal for both parametric generation and frequency doubling. The output power of the cw OPO based on the KTA crystal is low because the OPO cavity losses are high and draw most of the power converted from the Ti:sapphire pump beam resulting very little room for SHG by rotating the intracavity QWP.

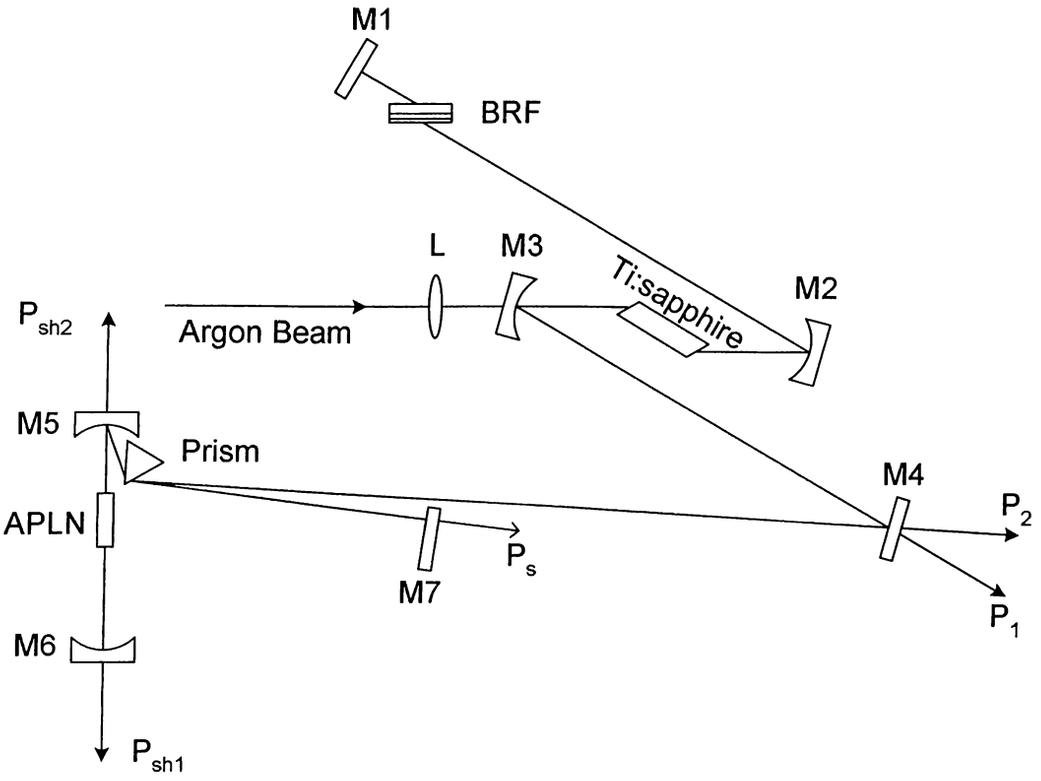

Figure 6.6: Continuous-wave SD-OPO setup.

6.3 Continuous-wave Self-doubling APLN OPOs

In this cw experiment, we use the APLN crystal that we used in the femtosecond SD-OPO experiment in Section 5.5. The detailed description of the aperiodic grating design of the crystal can be found in Section 4.2.5. However, in the experiment, the crystal temperature is at a higher temperature of 213 °C than the designed temperature of 130 °C because we observed an effect called photo refractive damage at the designed temperature. At this temperature, with the pump at 799.4 nm, the signal at 1151.4 nm and the second harmonic at 575.7 nm are generated. All the beams are polarized along the horizontal direction which is congruent to the z-axis of the crystal. This polarization geometry belongs to class-A SD-OPOs as defined in [42].

Our experimental setup is shown in Figure 6.6. It is very similar to the experimental setup described in Section 6.2. In this setup, the KTA crystal is replaced with the APLN crystal. The Ti:sapphire laser cavity is same except some modification to distances between the mirrors. However, the OPO cavity is formed by M6, M5 and M7. M7 is a flat high reflector mirror at the signal wavelength. The lowest order transverse mode of

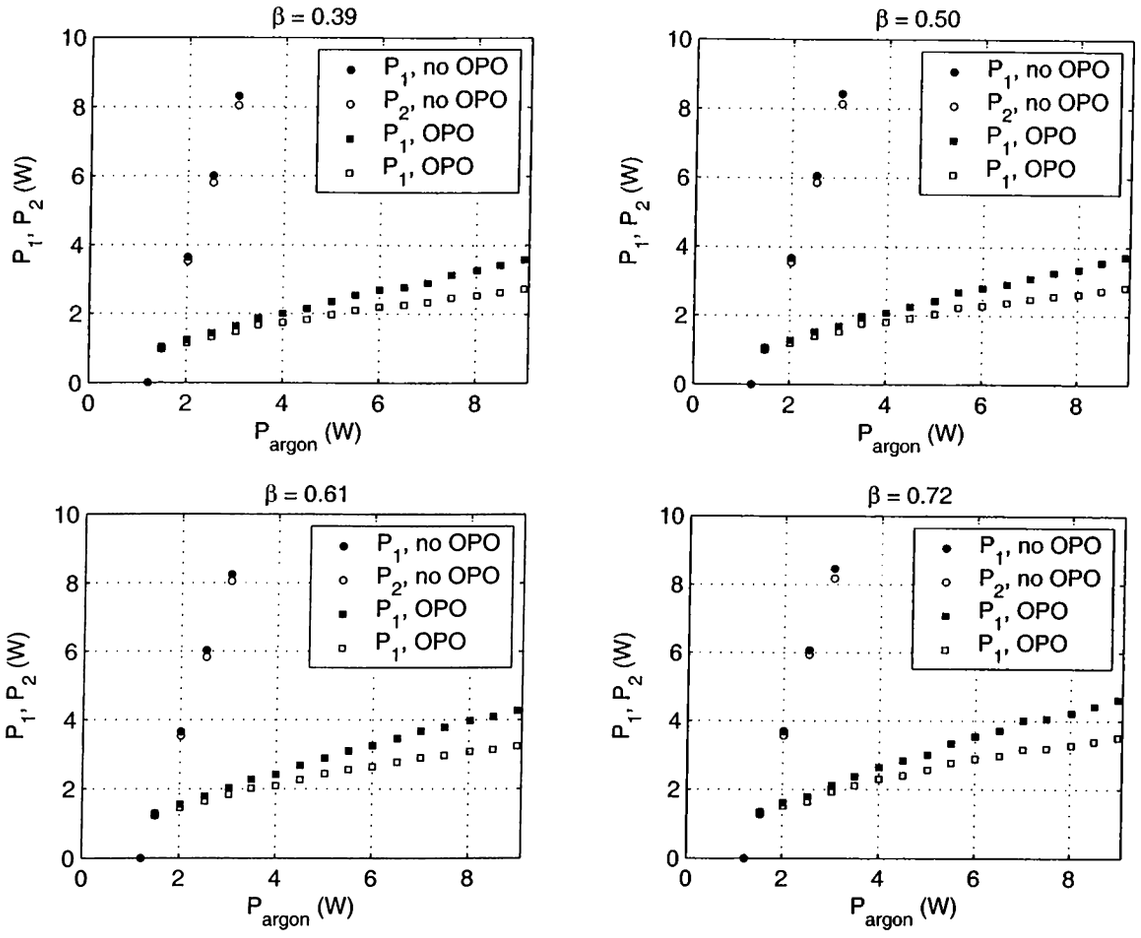

Figure 6.7: The intracavity Ti:sapphire laser powers P_1 and P_2 with or without optical parametric oscillation for $\beta = 0.39$, 0.50, 0.61 and 0.72.

the cavity forms an intracavity focus with a diameter of 25 μm and 28 μm (calculated) for the signal and the pump beams between M5 and M6 with the APLN crystal placed at the focus. The fast axis of the crystal is parallel to the horizontal plane coinciding with the polarization of the pump beam. We used same measurement setup in Section 6.2 but the intracavity signal power measurement made behind M7 in this experiment.

β	P_{TH} (W)	P_1 (W)	P_2 (W)
0.39	1.49	3.58	2.73
0.50	1.49	3.71	2.83
0.61	1.50	4.26	3.24
0.72	1.54	4.61	3.51

Table 6.1: APLN data.

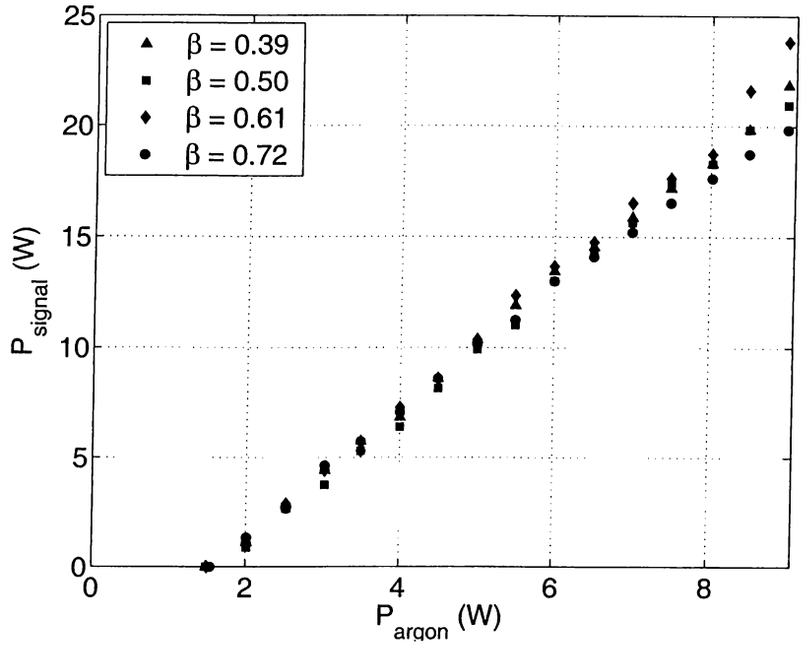

Figure 6.8: The intracavity signal power P_s for $\beta = 0.39$, 0.50, 0.61 and 0.72.

With the addition of the OPO section, Ti:sapphire laser threshold is 1.2 W. When we block the OPO operation, the intracavity Ti:sapphire laser powers P_1 and P_2 are 35.9 W and 34.7 W at the argon power of 9.0 W, respectively. This corresponds to 3.3% losses in the OPO section including M4. Figure 6.7 shows the intracavity Ti:sapphire power

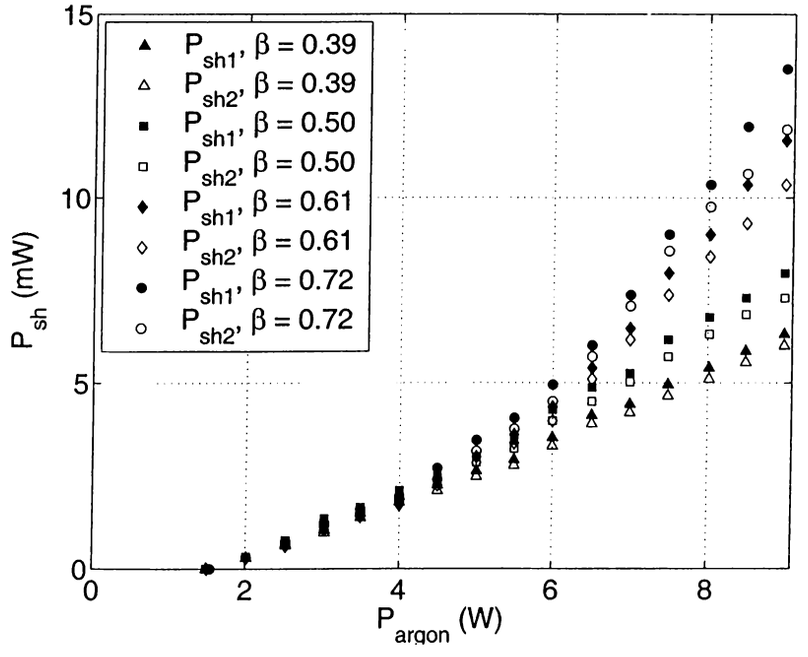

Figure 6.9: The second-harmonic output powers P_{sh1} and P_{sh2} for $\beta = 0.39$, 0.50, 0.61 and 0.72.

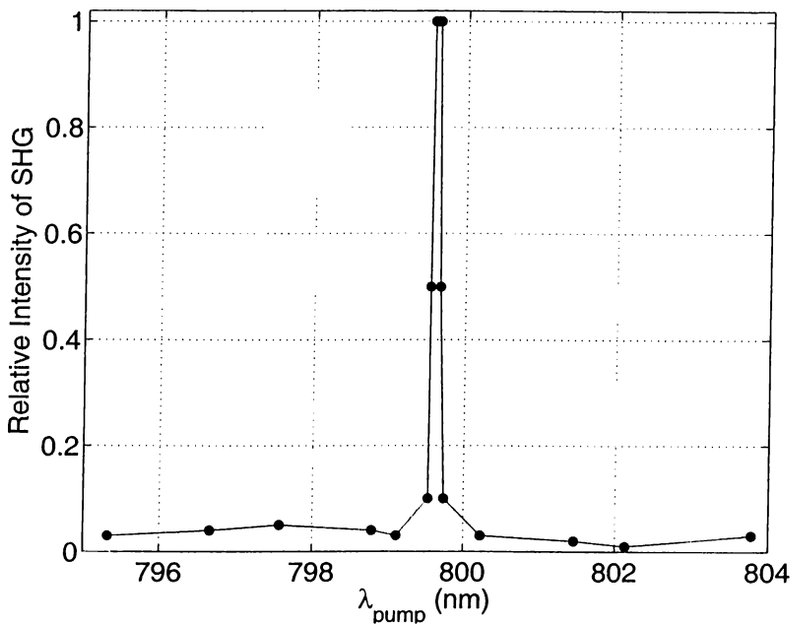

Figure 6.10: Pump wavelength tuning.

for β = 0.39, 0.50, 0.61 and 0.72. Table 6.1 is also shows the OPO threshold P_{TH}, P_1 and P_2 at an argon pump power of 9.0 W. Figure 6.8 shows the intracavity signal power P_s for β = 0.39, 0.50, 0.61 and 0.72. There is a slight difference in the signal power; the signal power decreases with increasing in β. Figure 6.9 shows the second-harmonic output power for β =0.39, 0.50, 0.61 and 0.72. For all β values, powers are increasing

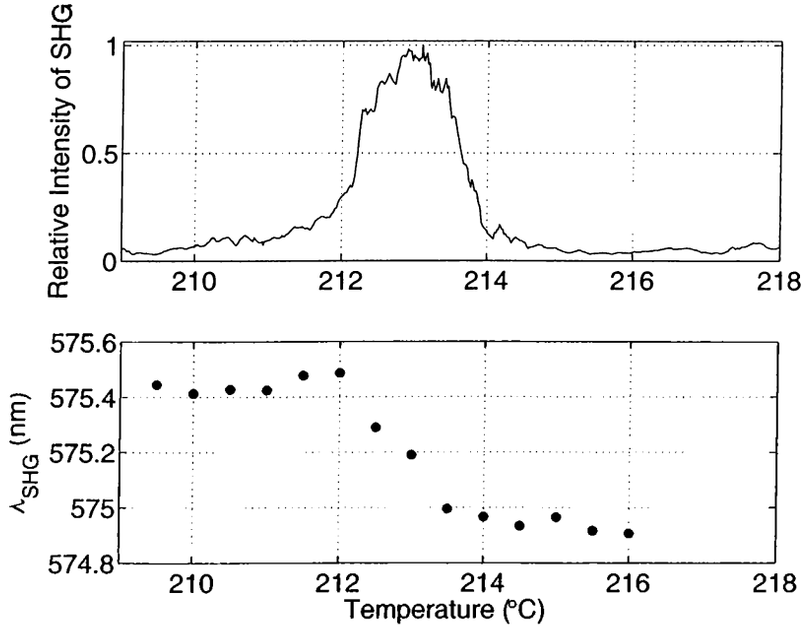

Figure 6.11: Temperature tuning.

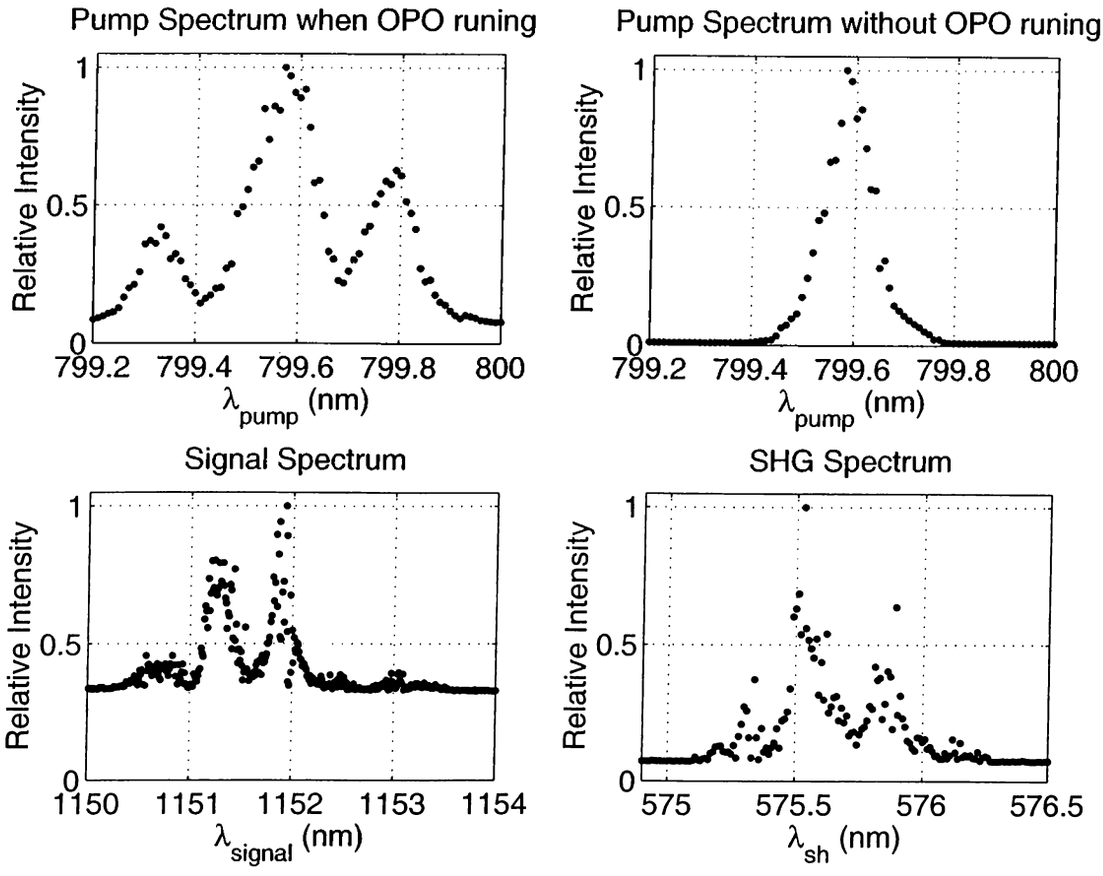

Figure 6.12: Spectrum of the pump, depleted pump, signal, and second harmonic.

with increase in an argon power but data for $\beta = 0.72$ has a greater increase. The total maximum second harmonic power for $\beta = 0.72$ is 25.5 mW.

Figures 6.10 and 6.11 show the change in the second-harmonic output power as a change in the pump wavelength and the crystal temperature. These data are taken to show that the SHG interaction is phase-matched. The sharp drop of the relative intensity in Figure 6.10 is an indication of a phase-matched interaction.

Figure 6.12 shows the spectrum of the pump, the signal and the second-harmonic beams. When OPO is not running, the pump spectrum has a single peak at 799.6 nm but when OPO is running, the pump spectrum has three peaks in addition to the peak at 799.6 nm. This is due to bandwidth-limited high nonlinear loss introduced by the OPO. This loss affects the loss profile of BRF which is used for wavelength selection of the Ti:sapphire laser. The signal and the second-harmonic spectrum are also effected by this operation.

In the cw experiments, although we could not get good efficiencies, we demonstrated cw systems in which three different system co-exist. The second-harmonic output of the cw OPO based on the KTA crystal is low because the OPO cavity losses are high and draw most of the power converted from the Ti:sapphire pump beam resulting very little room for SHG by rotating the intracavity quarter-wave plate. The second-harmonic output of the cw OPO based on the APLN crystal is also low but in this case the reason is the low β values in addition to the OPO cavity losses.

Chapter 7

Conclusion

In this thesis, we presented our work on upconverting OPO experiments. Simultaneous phase matching of optical parametric oscillation and SHG or SFG is employed in these OPOs except for one experiment. We achieved good results in all our experiments. In addition to the experiments, we developed a design method for QPM that is used for simultaneous phase matching of any two arbitrary interaction. We also demonstrated the effectiveness of this method with two experiments.

In Chapter 5, we presented experiments on femtosecond SD-OPOs and a femtosecond SF-OPO. To our knowledge, the femtosecond SD-OPO based on a KTP crystal is the first demonstration of an OPO employing simultaneous phase matching. In this experiment, in addition to very efficient two step conversion from the pump wavelength to the second-harmonic of the signal wavelength (reaching 34% in the KTP crystal), we demonstrated tuning by rotating the crystal in conjunction with changing the pump laser wavelength. The second experiment of SD-OPO is based on a KTA crystal. We also demonstrated very efficient two step conversion reaching 39% in the KTA crystal. To the best of our knowledge, this is the highest efficiency for an intracavity-doubled OPO. In this experiment, we also employed a delay between the two orthogonally polarized signal components to partially overcome GVM effects in the KTA crystal. We could not demonstrate the tuning of this SD-OPO because the KTA crystal that we used is relatively long. In addition, we set up an external pulse compressor and reduced the second-harmonic pulse width by 40%.

Other than the SD-OPOs based on the KTP and KTA crystals, we also demonstrated a femtosecond SF-OPO based on another KTP crystal in which both parametric oscillation and SFG between the pump and the signal waves are phase-matched simultaneously. We achieved 43% power conversion efficiency. To the best of our knowledge, this is the highest value reported for an upconversion OPO. To overcome GVM effects in the simultaneous interactions, we applied a delay between the two orthogonally polarized pump components and achieved more that three times increase in efficiency. In addition, we demonstrated limited tuning of this device.

In Chapter 5, we also presented experiments on femtosecond OPOs that employ QPM. One of these is an intracavity-doubled OPO based on a PP-KTP crystal; a BBO crystal provides frequency-doubling of the signal beam. To our knowledge, this experiment is the first demonstration of an intracavity-doubled OPO based on PP-KTP. In this device, a cavity-length tuning method which results in a fast change of frequency is employed. We achieved 90 nm wavelength tuning around 630 nm which was limited by the reflectivity of the cavity mirrors. Unfortunately, in this experiment, the direction of the second-harmonic was changing with the change in frequency unless we adjust the angle of the BBO crystal because noncolinear phase matching of SHG occurs in the crystal. We achieved efficient conversion from the pump wavelength to the second-harmonic, reaching 15.9%.

The last femtosecond experiment was performed for a quick verification of our aperiodically-poled crystal design method that we presented in Section 3.5. In this experiment, we employed the APLN crystal designed to convert a pump beam at 790 nm to a second-harmonic beam at 570 nm. The wavelengths used in the design process are well-matched with the measured wavelengths at a temperature of 130 °C and we achieved 17.9% conversion efficiency. However, the second-harmonic pulse width was very long compared to the pump pulse width due to GVM between the second-harmonic and the signal pulses.

In our femtosecond experiments, although we achieved very high efficiencies, our upconverted outputs suffered from pulse width broadening. This is due to two reasons: one of these is the broadening of signal pulse due to intracavity group velocity dispersion.

This effect can be reduced by intracavity pulse compensation schemes but we did not construct such a system because it requires four dispersive prisms to be inserted into the OPO cavities which make cavity alignment very difficult. The other one is due to GVM effect. In the generation process of second harmonic or sum frequency, the output pulse walks away from the pulses that generate it, but the pulses continue to generate second harmonic or sum-frequency output as a result the output pulse is spread over time. We believe the GVM effect is the dominant reason for the output pulse broadening but this point needs detailed theoretical analysis as well.

Our cw experiments in Chapter 6 are based on the same crystals used in the femtosecond SD-OPOs based on the KTA and APLN crystal. In our cw experiments, in addition to OPOs, we designed a cw Ti:sapphire laser. The thermal lensing effect in the Ti:sapphire crystal caused by high intensity of the Argon-ion laser made it difficult to join the OPO and Ti:sapphire laser cavities. In both experiments, the conversion efficiency is low because for the OPO based on the KTA crystal, the OPO cavity losses are high and draw most of the power converted from the Ti:sapphire pump beam. As a result, there is very little room for SHG by rotating the intracavity QWP. The reason for the cw OPO based on the APLN crystal is a little different. In this case, in addition to the OPO cavity losses, the β values are low.

In this thesis, in addition to the experiments, we described a method that facilitates the design of aperiodic grating structures to simultaneously quasi-phase match two arbitrary second-order nonlinear processes within the same crystal. This method is much simpler than previous approaches to the same problem. Since the relative strength of the two processes can be adjusted freely, the conversion efficiency of the overall process can be optimized. The SD-OPO experiments using the APLN crystal provide experimental verification of our method. In our simple design method, we have result in large d_{eff} values for the APLN crystal, but we do not sure whether they are the highest possible values that we can achieve using an aperiodic grating structure.

The simultaneous phase matching of two different second-order nonlinear processes within the same crystal opens up many frequency conversion possibilities. In a future world, QPM techniques will no doubt play a central role in realizing various simultaneous

phase matching condition for two or more interactions. An improvement in our design method to include multiple interaction will be a first step but not the only one. Aperiodic grating design techniques that can employ highest possible Fourier coefficients will be another one. In addition to these improvements in the QPM method, numerical analysis including the various effect that we observed in our experiments will be useful in designing a better OPO system.

Appendix A

Miller's Rule Factor

Dispersion in the second-order nonlinear tensor elements is accounted by Miller's Rule factor

$$M_{ijk} = \frac{[n_i(\omega_3)^2 - 1] \times [n_j(\omega_2)^2 - 1] \times [n_k(\omega_1)^2 - 1]}{[n_i(\Omega_3)^2 - 1] \times [n_j(\Omega_2)^2 - 1] \times [n_k(\Omega_1)^2 - 1]}, \tag{A.1}$$

where Ω_1, Ω_2, and Ω_3 are reference frequencies at which the nonlinear tensor elements are reported [80]. Therefore,

$$\overleftrightarrow{\chi}^{(2)}_{ijk}(\omega_3, \omega_2, \omega_1) = \overleftrightarrow{\chi}^{(2)}_{ijk}(\Omega_3, \Omega_2, \Omega_1) \times M_{ijk}. \tag{A.2}$$

Bibliography

[1] T. H. Maiman, "Stimulated optical radiation in ruby," *Nature*, vol. 187, 1960.

[2] T. Kartaloğlu, "Femtosecond optical parametric oscillators based on potassium titanyl phosphate crystals," M.S. thesis, Bilkent University, 1996.

[3] T. Kartaloğlu, K. G. Köprülü, and O. Aytür, "Phase-matched self-doubling optical parametric oscillator," in *IEEE Lasers and Electro-Optics Society 1996 Annual Meeting Conference Proceedings*. Institute of Electrical and Electronics Engineers, Piscataway, NJ, 1996, pp. 20–21.

[4] T. Kartaloğlu, K. G. Köprülü, and O. Aytür, "Phase-matched self-doubling optical parametric oscillator," *Optics Letters*, vol. 22, pp. 280–282, 1997.

[5] K. G. Köprülü, T. Kartaloğlu, and O. Aytür, "Single-crystal sum-frequency generating optical parametric oscillator,," in *Conference on Lasers and Electro Optics*. Optical Society of America, Washington, DC, 1997, pp. 457–458.

[6] K. G. Köprülü, T. Kartaloğlu, Y. Dikmelik, and O. Aytür, "Advances in femtosecond single-crystal sum-frequency generating optical parametric oscillators," in *IEEE/LEOS Conference on Nonlinear Optics*. Institute of Electrical and Electronics Engineers, Piscataway, NJ, 1998, pp. 215–217.

[7] K. G. Köprülü, T. Kartaloğlu, Y. Dikmelik, and O. Aytür, "Single-crystal sum-frequency-generating optical parametric oscillator," *Journal of the Optical Society of America B - Optical Physics*, vol. 16, pp. 1546–1552, 1999.

[8] T. Kartaloğlu, Z. G. Figen, and O. Aytür, "A self-doubling optical parametric oscillator based on aperiodically-poled lithium niobate," in *2001 IEEE/LEOS*

Annual Meeting Conference Proceedings. Institute of Electrical and Electronics Engineers, Piscataway, NJ, 2001, pp. 243–244.

[9] T. Kartaloğlu, Z. G. Figen, and O. Aytür, "Simultaneous phase matching of optical parametric oscillation and second harmonic generation in aperiodically-poled lithium niobate," Accepted for publication in Journal of the Optical Society of America B - Optical Physics.

[10] T. Kartaloğlu and O. Aytür, "Femtosecond self-doubling optical parametric oscillator based on $KTiOAsO_4$," Submitted to IEEE Journal of Quantum Electronics.

[11] P. A. Franken, A. E. Hill, C. W. Peters, and G. Weinreich, "Generation of optical harmonics," *Physical Review Letters*, vol. 7, pp. 118–119, 1961.

[12] D. A. Kleinman, "Nonlinear dielectric polarization in optical media," *Physical Review*, vol. 126, pp. 1977–1979, 1962.

[13] P. D. Maker, R.W. Terhune, M. Nisenhoff, and C. M. Savage, "Effects of dispersion and focusing on the production of optical harmonics," *Physical Review Letters*, vol. 8, pp. 21–22, 1962.

[14] J. A. Armstrong, N. Bloembergen, J. Ducuing, and P. S. Pershan, "Interactions between light waves in a nonlinear dielectric," *Physical Review*, vol. 127, pp. 1918–1939, 1962.

[15] R. H. Kingston, "Parametric amplification and oscillation of optical frequencies," *Proceedings of the Institute of Radio Engineers*, vol. 50, 1962.

[16] N. M. Kroll, "Parametric amplification in spatially extended media and application to the design of tunable oscillators at optical frequencies," *Physical Review*, vol. 127, 1962.

[17] C. C. Wang and G. W. Racette, "Measurement of parametric gain accompanying optical difference frequency generation," *Applied Physics Letters*, vol. 6, 1965.

[18] J. A. Giordimane and R. C. Miller, "Tunable coherent parametric oscillation in $LiNbO_3$ at optical frequencies," *Physical Review Letters*, vol. 14, pp. 973–976, 1965.

[19] "Optical parametric oscillation and amplification," in *Journal of the Optical Society of America B - Optical Physics*, R. L. Byer and A. Piskarskas, Eds., vol. 10, p. 1655. 1993.

[20] "Optical parametric devices," in *Journal of the Optical Society of America B - Optical Physics*, W. R. Bosenberg and R. C. Eckardt, Eds., vol. 12, p. 2048. 1995.

[21] L. E. Myers, R. C. Eckardt, M. M. Fejer, R. L. Byer, W. R. Bosenberg, and J. W. Pierce, "Quasi-phase-matched optical parametric oscillators in bulk periodically poled $LiNbO_3$," *Journal of the Optical Society of America B - Optical Physics*, vol. 12, pp. 2102–2116, 1995.

[22] I. Camlibel, "Spontaneous polarization measurements in several ferroelectric oxides using a pulsed field method," *Journal of Applied Physics*, vol. 40, pp. 1690–1693, 1969.

[23] D. Feng, N. B. Ming, J. F. Hong, Y. S. Yang, J. S. Zhu, Z. Yang, and Y. N. Wang, "Enhancement of second-harmonic generation in $LiNbO_3$ crystals with periodic laminar ferroelectric domains," *Applied Physics Letters*, vol. 37, pp. 607–609, 1980.

[24] A. Feisst and P. Koidl, "Current induced periodic ferroelectric domain structures in $LiNbO_3$ applied for efficient nonlinear optical frequency mixing," *Applied Physics Letters*, vol. 47, pp. 1125–1127, 1985.

[25] M. Yamada, N. Nada, M. Saitoh, and K. Watanabe, "First-order quasi-phase-matched $LiNbO_3$ waveguide periodically poled by applying an external electric field for efficient blue second-harmonic generation," *Applied Physics Letters*, vol. 62, pp. 435–436, 1993.

[26] W. K. Burns, W. McElhanon, and L. Goldberg, "Second-harmonic generation in field poled quasi-phasematched bulk $LiNbO_3$," *IEEE Photonics Technology Letters*, vol. 6, pp. 252–254, 1994.

[27] J. Webjorn, V.Pruneri, P. S. Russell, J. R. M. Barr, and D. C. Hanna, "Quasi-phasematched blue-light generation in bulk lithium niobate, electrically poled via periodic liquid electrodes," *Electronics Letters*, vol. 30, pp. 894–895, 1994.

[28] D. C. Edelstein, E. S. Wachman, and C. L. Tang, "Broadly tunable high repetition rate femtosecond optical parametric oscillator," *Applied Physics Letters*, vol. 54, pp. 1728–1730, 1989.

[29] H. M. van Driel, "Synchronously pumped optical parametric oscillators," *Appl. Phys. B*, vol. 60, pp. 411–420, 1995.

[30] W. S. Pelouch, P. E. Powers, and C. L.Tang, "Ti:sapphire-pumped, high-repetition-rate femtosecond optical parametric oscillator," *Optics Letters*, vol. 17, pp. 1070–1072, 1992.

[31] Q. Fu, G. Mak, and H. M. van Driel, "High-power, 62-fs infrared optical parametric oscillator synchronously pumped by a 76-MHz Ti:sapphire laser," *Optics Letters*, vol. 17, pp. 1006–1008, 1992.

[32] G. Mak, Q, Fu, and H. M. van Driel, "Externally pumped high repetition rate femtosecond infrared optical parametric oscillator," *Applied Physics Letters*, vol. 60, pp. 542–544, 1992.

[33] P. E. Powers, C. L. Tang, and L. K. Cheng, "High-repetition-rate femtosecond optical parametric oscillator based on $CsTiOAsO_4$," *Optics Letters*, vol. 19, pp. 37–39, 1994.

[34] T. J. Driscoll, G. M. Gale, and F. Hache, "Ti:sapphire 2nd-harmonic-pumped visible range femtosecond optical parametric oscillator," *Optics Communications*, vol. 110, pp. 638–644, 1994.

[35] A. Nebel, H. Frost, R. Beigang, and R. Wallenstein, "Visible femtosecond pulses by second harmonic generation of a cw mode-locked KTP optical parametric oscillator," *Appl. Phys. B*, vol. 60, pp. 453–458, 1995.

[36] R. J. Ellingson and C. L.Tang, "High-power high-repetition-rate femtosecond pulses tunable in the visible," *Optics Letters*, vol. 18, pp. 438–440, 1993.

[37] D. T. Reid, M. Ebrahimzadeh, and W. Sibbett, "Efficient femtosecond pulse generation in the visible in a frequency-doubled optical parametric oscillator based

on $RbTiOAsO_4$," *Journal of the Optical Society of America B - Optical Physics*, vol. 12, pp. 1157–1163, 1995.

[38] A. Shirakawa, H. W. Mao, and T. Kobayashi, "Highly efficient generation of blueorange femtosecond pulses from intracavity-frequency-mixed optical parametric oscillator," *Optics Communications*, vol. 123, pp. 121–128, 1996.

[39] E. C. Cheung, K. Koch, and G. T. Moore, "Frequency upconversion by phase-matched sum-frequency generation in an optical parametric oscillator," *Optics Letters*, vol. 19, pp. 1967–1969, 1994.

[40] R. A. Andrews, H. Rabin, and C. L. Tang, "Coupled parametric downconversion and upconversion with simultaneous phase matching," *Physical Review Letters*, vol. 25, pp. 605–608, 1970.

[41] V. Petrov and F. Noack, "Frequency upconversion of tunable femtosecond pulses by parametric amplification and sum-frequency generation in a single nonlinear crystal," *Optics Letters*, vol. 20, pp. 2171–2173, 1995.

[42] O. Aytür and Y. Dikmelik, "Plane-wave theory of self-doubling optical parametric oscillators," *IEEE Journal of Quantum Electronics*, vol. 34, pp. 447–458, 1998.

[43] Y. Dikmelik, G. Akgün, and O. Aytür, "Plane-wave dynamics of optical parametric oscillation with simultaneous sum-frequency generation," *IEEE Journal of Quantum Electronics*, vol. 35, pp. 897–912, 1999.

[44] M. Vaidyanathan, R. C. Eckardt, V. Dominic, L. E. Myers, and T. P. Grayson, "Cascaded optical parametric oscillations," *Optics Express*, vol. 1, pp. 49–53, 1997.

[45] G. T. Moore, K. Koch, M. E. Dearborn, and M. Vaidyanathan, "A simultaneously phase-matched tandem optical parametric oscillator," *IEEE Journal of Quantum Electronics*, vol. 34, pp. 803–810, 1998.

[46] S. D. Butterworth, P. G. R. Smith, and D. C. Hanna, "Picosecond Ti:sapphire-pumped optical parametric oscillator based on periodically poled $LiNbO_3$," *Optics Letters*, vol. 22, pp. 618–620, 1997.

[47] K. C. Burr, C. L. Tang, M. A. Arbore, and M. M. Fejer, "High-repetition-rate femtosecond optical parametric oscillator based on periodically poled lithium niobate," *Applied Physics Letters*, vol. 70, pp. 3341–3343, 1997.

[48] O. Pfister, J. S. Wells, L. Hollberg, L. Zink, D. A. Van Baak, M. D. Levenson, and W. R. Bosenberg, "Continuous-wave frequency tripling and quadrupling by simultaneous three-wave mixing in periodically poled crystals: application to a two-step 1.19-10.71-μm frequency bridge," *Optics Letters*, vol. 22, pp. 1211–1213, 1997.

[49] C. McGowan, D. T. Reid, Z. E. Penman, M. Ebrahimzadeh, W. Sibbett, and D. H. Jundt, "Femtosecond optical parametric oscillator based on periodically poled lithium niobate," *Journal of the Optical Society of America B - Optical Physics*, vol. 15, pp. 694–701, 1998.

[50] G. L. Luo, S. N. Zhu, J. L. He, Y. Y. Zhu, H. T. Wang, Z. W. Liu, C. Zhang, and N. B. Ming, "Simultaneously efficient blue and red light generations in a periodically poled $LiTaO_3$," *Applied Physics Letters*, vol. 78, pp. 3006–3008, 2001.

[51] X. P. Zhang, J. Hebling, J. Kuhl, W. W. Rühle, and H. Giessen, "Efficient intracavity generation of visible pulses in a femtosecond near-infrared optical parametric oscillator," *Optics Letters*, vol. 26, pp. 2005–2007, 2001.

[52] J. Feng, Y. Y. Zhu, and N. B. Ming, "Harmonic generations in an optical Fibonacci superlattice," *Physical Review B*, vol. 41, pp. 5578–5582, 1990.

[53] S. N. Zhu, Y. Y. Zhu, and N. B. Ming, "Quasi-phase-matched third-harmonic generation in a quasi-periodic optical superlattice," *Science*, vol. 278, pp. 843–846, 1997.

[54] S. N. Zhu, Y. Y. Zhu, Y. Q. Qin, H. F. Wang, C. Z. Ge, and N. B. Ming, "Experimental realization of second harmonic generation in a Fibonacci optical superlattice of $LiTaO_3$," *Physical Review Letters*, vol. 78, pp. 2752–2755, 1997.

[55] Y. Q. Qin, Y. Y. Zhu, S. N. Zhu, , and N. B. Ming, "Quasi-phase-matched harmonic generation through coupled parametric processes in a quasiperiodic optical superlattice," *Journal of Applied Physics*, vol. 84, pp. 6911–6916, 1998.

[56] Y. Y. Zhu, R. F. Xiao, J. S. Fu, G. K. L. Wong, and N. B. Ming, "Third harmonic generation through coupled second-order nonlinear optical parametric processes in quasiperiodically domain-inverted $Sr_{0.6}Ba_{0.4}Nb_2O_6$ optical superlattices," *Applied Physics Letters*, vol. 73, pp. 432–434, 1998.

[57] X. Liu, Z. Wang, J. Wu, and N. B. Ming, "Characterization of third-harmonic generation in Fibonacci optical superlattices," *Physical Review A*, vol. 58, pp. 4956–4960, 1998.

[58] Y. Q. Qin, Y. Y. Zhu, S. N. Zhu, G. P. Luo, J. Ma, and N. B. Ming, "Nonlinear optical characterization of a general Fibonacci optical superlattice," *Applied Physics Letters*, vol. 75, pp. 448–450, 1999.

[59] Y. Y. Zhu and N. B. Ming, "Dielectric superlattices for nonlinear optical effects," *Optical and Quantum Electronics*, vol. 31, pp. 1093–1128, 1999.

[60] Y. B. Chen, Y. Y. Zhu, Y. Q. Qin, C. Zhang, S. N. Zhu, and N. B. Ming, "Second harmonic and third harmonic generation in a three-component Fibonacci optical superlattice," *Journal of Physics-Condensed Matter*, vol. 12, pp. 529–537, 2000.

[61] Y. B. Chen, C. Zhang, Y. Y. Zhu, S. N. Zhu, H. T. Wang, and N. B. Ming, "Optical harmonic generation in a quasi-phase-matched three-component Fibonacci superlattice $LiTaO_3$," *Applied Physics Letters*, vol. 78, pp. 577–579, 2001.

[62] K. F. Kashi and A. Arie, "Multiple-wavelength quasi-phase-matched nonlinear interactions," *IEEE Journal of Quantum Electronics*, vol. 35, pp. 1649–1656, 1999.

[63] K. F. Kashi, A. Arie, P. Urenski, and G. Rosenman, "Multiple nonlinear optical interactions with arbitrary wave vector differences," *Physical Review Letters*, vol. 88, pp. art. no. 023903, 2002.

[64] C. Zhang, H. Wei, Y. Y. Zhu, H. T. Wang, S. N. Zhu, and N. B. Ming, "Third-harmonic generation in a general two-component quasi-periodic optical superlattice," *Optics Letters*, vol. 26, pp. 899–901, 2001.

[65] B. Y. Gu., B. Z. Dong, Y. Zhang, and G. Z. Yang, "Enhanced harmonic generation in aperiodical superlattices," *Applied Physics Letters*, vol. 75, pp. 2175–2177, 1999.

[66] B. Y. Gu., Y. Zhang, and B. Z. Dong, "Investigations of harmonic generations in aperiodic optical superlattices," *Journal of Applied Physics*, vol. 87, pp. 7629–7637, 2000.

[67] Y. Zhang and B. Y. Gu., "Optimal design of aperiodically poled lithium niobate crystals for multiple wavelengths parametric amplification," *Optics Communications*, vol. 192, pp. 417–425, 2001.

[68] H. Liu, Y. Y. Zhu, S. N. Zhu, C. Zhang, and N. B. Ming, "Aperiodical optical superlattices engineered for optical frequency conversion," *Applied Physics Letters*, vol. 79, pp. 728–730, 2001.

[69] T. Kartaloğlu, K. G. Köprülü, O. Aytür, M. Sundheimer, and W. P. Risk, "Femtosecond optical parametric oscillator based on periodically poled $KTiOPO_4$," *Optics Letters*, vol. 23, pp. 61–63, 1998.

[70] F. G, Colville, M. H. Dunn, and M. Ebrahimzadeh, "Continuous-wave, singly resonant, intracavity parametric oscillator," *Optics Letters*, vol. 22, pp. 75–77, 1997.

[71] G. A. Turnbull, T. J. Edwards, M. H. Dunn, and M. Ebrahimzadeh, "Continuous-wave singly-resonant intracavity optical parametric oscillator based on periodically-poled $LiNbO_3$," *Electronics Letters*, vol. 33, pp. 1817–1818, 1997.

[72] T. J. Edwards, G. A. Turnbull, M. H. Dunn, M. Ebrahimzadeh, H. Karlsson, G. Arvidsson, and F. Laurell, "Continuous-wave singly resonant optical parametric oscillator based on periodically-poled $RbTiOAsO_4$," *Optics Letters*, vol. 23, pp. 837–839, 1998.

[73] T. J. Edwards, G. A. Turnbull, M. H. Dunn, M. Ebrahimzadeh, and F. G, Colville, "High-power, continuous-wave, singly resonant, intracavity optical parametric oscillator," *Applied Physics Letters*, vol. 72, pp. 1527–1529, 1998.

[74] R. W. Boyd, *Nonlinear Optics*, Academic Press Inc., 1992.

[75] D. K. Cheng, *Field and Wave Electromagnetics*, Addison-Wesley, 1991.

[76] R. A. Baumgartner and R. L. Byer, "Optical parametric amplification," *IEEE Journal of Quantum Electronics*, vol. QE-15, pp. 432–444, 1979.

[77] M. M. Fejer, G. A. Magel, D. H. Jundt, and R. L. Byer, "Quasi-phase-matched second harmonic generation: tuning and tolerances," *IEEE Journal of Quantum Electronics*, vol. 28, pp. 2631–2654, 1992.

[78] R. L. Byer, "Quasi-phasematched nonlinear interactions and devices," *Journal of Nonlinear Optical Physics & Materials*, vol. 6, pp. 549–592, 1997.

[79] D. F. Lawden, *Elliptic Functions and Applications*, Springer-Verlag, 1989.

[80] D. A. Roberts, "Simplified characterization of uniaxial biaxial nonlinear optical crystals: A plea for standardization of nomenclature and conventions," *IEEE Journal of Quantum Electronics*, vol. 28, pp. 2057–2074, 1992.

[81] T. A. Maldonado and T. K. Gaylord, "Light propagation characteristics for arbitrary wavevector directions in biaxial media by a coordinate-free approach," *Applied Optics*, vol. 30, pp. 2465–2480, 1991.

[82] J. Yao, W. Sheng, and W. Shi, "Accurate calculation of the optimum phase-matching parameters in three-wave interactions with biaxial nonlinear-optical crystals," *Journal of the Optical Society of America B - Optical Physics*, vol. 9, pp. 891–902, 1992.

[83] J. T. Wang and K. Daneshvar, "Numerical Calculation of the Effective Second-Order Nonlinear Coefficient Along Collinear Phase-Matching Directions Inside Nonlinear Crystals in Three-Wave Interaction," *IEEE Journal of Quantum Electronics*, vol. 32, pp. 183–191, 1996.

[84] H. Ito, H. Naito, and H. Inaba, "Generalized study on angular dependence of induced second-order nonlinear optical polarizations and phase matching in biaxial crystals," *Journal of Applied Physics*, vol. 46, pp. 3992–3998, 1975.

[85] K. F. Lee and H. B. Ahmad, "A simple model for the calculation of the walk-off angle in uniaxial crystal," *Optics Communications*, vol. 104, pp. 111–117, 1993.

[86] W. Q. Zhang, "Optical parametric generation for biaxial crystal," *Optics Communications*, vol. 105, pp. 226–232, 1994.

[87] G. J. Zhang, S. Horinounchi, T. Kinoshita, and K. Sasaki, "Theoretical analysis of the spatial phase-matching loci for second-harmonic generation and multiwave-mixing interactions," *Applied Optics*, vol. 34, pp. 5301–5311, 1995.

[88] B. E. A. Saleh and M. C. Teich, *Fundamentals of Photonics*, John Wiley & Sons, Inc., 1991.

[89] V. G. Dmitriev, G. G. Gurzadyan, and D. N. Nikogosyan, *Handbook of Nonlinear Optical Crystals*, Springer, 1997.

[90] K. Kato, "Parametric oscillation at 3.2μm in KTP pumped at 1.064μm," *IEEE Journal of Quantum Electronics*, vol. 27, pp. 1137–1140, 1991.

[91] J.-P. Fève, B. Boulanger, O. Pacaud, I. Rousseau, B. Ménaert, G. Marnier, P. Villeval, C. Bonnin, G. M. Loiacono, and D. N. Loiacono, "Phase-matching measurements and Sellmeier equations over the complete transparency range of $KTiOAsO_4$, $RbTiOAsO_4$, and $CsTiOAsO_4$," *Journal of the Optical Society of America B - Optical Physics*, vol. 17, pp. 775–780, 2000.

[92] Q. Chen and W. P. Risk, "Periodic poling of $KTiOPO_4$ using an applied electric-field," *Electronics Letters*, vol. 30, pp. 1516–1517, 1994.

[93] G. J. Edwards and M. Lawrence, "A temperature-dependent dispersion equation for congruently grown lithium niobate," *Optical and Quantum Electronics*, vol. 16, pp. 373–375, 1984.

[94] D. H. Jundt, "Temperature-dependent Sellmeier equation for the index of refraction, n_e, in congruent lithium niobate," *Optics Letters*, vol. 22, pp. 1553–1553, 1997.

[95] L. E. Myers and R. L. Byer, "93% pump depletion, 3.5-W continuous-wave, singly resonant optical parametric oscillator," *Optics Letters*, vol. 21, pp. 1336–1338, 1996.

[96] M. Taya, M. C. Bashaw, and M. M. Fejer, "Photorefractive effects in periodically poled ferroelectrics," *Optics Letters*, vol. 21, pp. 857–859, 1996.

[97] M. Oron, M. Katz, D. Eger, G. Rosenman, and A. Skliar, "Highly efficient blue light generation in flux grown $KTiOPO_4$ periodically poled by an electric field," *Electronics Letters*, vol. 33, pp. 807–808, 1997.

[98] A. Haché, G. R. Allan, and H. M. van Driel, "Effects of cavity detuning on the pulse characteristics of a femtosecond synchronously pumped optical parametric oscillator," *Journal of the Optical Society of America B - Optical Physics*, vol. 12, pp. 2209–2213, 1995.

[99] J. M. Dudley, D. T. Reid, M. Ebrahimzadeh, and W. Sibbett, "Characteristics of a noncritically phasematched Ti-Sapphire pumped femtosecond optical parametric oscillator," *Optics Communications*, vol. 104, pp. 419–430, 1994.

Vita

Tolga Kartaloğlu was born in Ankara, Turkey, on July 21, 1972. He received his B.Sc. degree from the Department of Electrical and Electronics Engineering at Middle East Technical University, Ankara, Turkey in 1994, and his MSc. degree from the Department of Electrical and Electronics Engineering at Bilkent University, Ankara, Turkey in 1996. He then pursued his Ph.D studies at the Department of Electrical and Electronics Engineering, Bilkent University. His research interests include lasers, nonlinear optics, wavelength conversion, and optical parametric oscillators and amplifiers.